

Development of Biocompatible Aptamer Films as Smart Materials for Novel Fertilizer Systems

by

Amanda Foster
BSc (Hon), Carleton University 2011

A thesis submitted to the Faculty of Graduate and
Postdoctoral Affairs in partial fulfillment of the requirements
for the degree of

Master of Science

in

Chemistry

Carleton University

Ottawa, Ontario

© 2013

Amanda Foster

Abstract

Aptamers are short, single stranded nucleic acids that fold into well-defined 3D structures which bind to a single target molecule with affinities and specificities that can rival or in some cases exceed those of antibodies. Unlike antibodies, aptamers can be chemically synthesized, which eliminates the need for animals, and can be used under non-physiological as well as physiological conditions. Due to their chemical nature, aptamers can be readily modified with reporter molecules and other functional groups making them versatile analytical tools with great promise in biotechnological applications. The compatibility of aptamers with nanostructures such as thin films, in combination with their affinity, selectivity, and conformational changes upon target interaction could set the foundation for the development of smart materials. This research will focus on development of a biocompatible aptamer-polyelectrolyte film system for use in controlled-release applications. We will study the efficacy and feasibility of this system. In doing this, we demonstrated the ability of the sulforhodamine B aptamer to function while sequestered in a chitosan-hyaluronan film matrix (Chapter 2). Our results also suggest that deposition conditions such as rinsing time and volume play a strong role in the internal film interactions and growth mechanism. As a secondary objective, the protective role of the polyelectrolytes against nuclease-mediated aptamer degradation was investigated (Chapter 3). Degradation remains one of the biggest challenges in nucleic acid-based technologies. This research has the potential to revolutionize materials used in

controlled-release platforms with possible application to fertilizer systems which will be discussed.

Acknowledgements

As probably the world's least sentimental person, I seriously considered using Mad Libs for my acknowledgements section but after getting "There once was a lab I'd like to thank for their supportive trip to the moon" as my first sentence I was resigned to take it into my own hands. First of all, a million thank you's go to my supervisor Dr. Maria DeRosa for all her support and un-ending optimism through all the highs and lows of my project. Seriously, if you could find a way to bottle your optimism, not only would you be very rich, but the world would be a better place! To JP for all the love and support, even when you were neglected in the name of science. Thank you especially for your superb cooking; you saved me from a permanent diet of popcorn and Uncle Ben's Instant Rice (if that isn't love, then I don't know what is!). To MM for being a friend and mentor; always answering my millions of e-mails on every subject possible from science to the meaning of life. TF for e-mailing if you hadn't heard from me in too long just to make sure some thesis-crazed tragedy hadn't befallen me. As my career advisor, MB, for long heart-to-heart conversations about life and alternate careers, just in case (garbage man comes to mind). AG, just for being the beautiful person that you are! To YS, for helping me get this project off the ground. To EM, EM, and KH, whom I can always count on for a crazy-fun (and exceptionally glittery) time. And of course, all the other people in and outside of the lab who have helped me over the years. Finally, a special thank you to my cat, Tony, for showing me the best thing to do with a scientific paper is sleep on it, especially if someone is trying to read it (oh how I could have too!).

Table of Contents

| | |
|--|--------------|
| Abstract | ii |
| Acknowledgements | iv |
| List of Tables | vii |
| List of Figures | viii |
| List of Abbreviations | xviii |
| Chapter 1. Introduction | 1 |
| 1.1. Nanomaterials | 1 |
| 1.2. Aptamers..... | 3 |
| 1.3. Smart Fertilizers | 9 |
| 1.3.1. Challenges in Agriculture..... | 9 |
| 1.3.2. An Aptamer-based Approach | 14 |
| 1.4. Polyelectrolyte Multilayers (PEMs) | 17 |
| 1.4.1. Layer-by-layer (LBL) method of film deposition | 18 |
| 1.4.2. Linear versus Exponential Film Growth Mechanisms | 21 |
| 1.5. Thesis Objective..... | 28 |
| Chapter 2. Preparation of aptamer-containing multilayer films | 29 |
| 2.1. Introduction | 29 |
| 2.1.1. Aptamer-functionalized multilayer films | 29 |
| 2.1.2. CHI/HA films..... | 30 |
| 2.1.3. Chapter Objectives..... | 33 |
| 2.2. Experimental | 34 |
| 2.2.1. Materials | 34 |
| 2.2.2. Preparation of the aptamer and random DNA sequences..... | 35 |
| 2.2.3. Film deposition | 37 |
| 2.2.4. Time of Flight Secondary Ion Mass Spectroscopy | 39 |
| 2.2.5. Microscopy | 40 |
| 2.3. Results and Discussion | 42 |
| 2.3.1. Optimization of CHI/HA films and assessment of film morphology..... | 42 |
| 2.3.2. ToF-SIMS analysis of target binding..... | 52 |
| 2.3.3. Fluorescent microscope analysis of target binding | 58 |
| 2.3.4. Investigation of film growth by UV-vis spectrophotometry..... | 70 |

| | |
|---|------------|
| 2.4. Conclusions..... | 95 |
| 2.5. Acknowledgements | 96 |
| Chapter 3. Development of an assay assessing film protective properties against nuclease-mediated degradation..... | 97 |
| 3.1. Introduction | 97 |
| 3.1.1. Limitations of <i>in vivo</i> aptamer nanotechnology | 97 |
| 3.1.2. Chapter Objectives..... | 103 |
| 3.2. Experimental | 103 |
| 3.2.1. Materials | 103 |
| 3.2.2. Optimization of ssDNA degradation by Nuclease S ₁ | 104 |
| 3.2.3. PAGE gel analysis of nuclease assay | 106 |
| 3.2.4. Fluorescence-based analysis of nuclease assay..... | 107 |
| 3.3. Results and Discussion | 109 |
| 3.3.1. Optimized protocol for digestion of ssDNA by Nuclease S ₁ | 109 |
| 3.3.2. Analysis of film nuclease assay by PAGE | 115 |
| 3.3.3. Analysis of film nuclease assay using fluorescence..... | 117 |
| 3.4. Conclusions..... | 124 |
| Chapter 4. Contributions to knowledge and future studies..... | 125 |
| Appendices..... | 127 |
| References... .. | 136 |

List of Tables

Table 2-1: Film morphology and roughness parameters determined for two 60x60 μm^2 AFM images of films containing the SA aptamer or RO control, with or without exposure to SB dye. Two trials (A and B) were taken from different areas on the same film. All values were calculated with NOVA software. AFM images were taken in tapping mode..... 49

Table 2-2: Review of deposition conditions from literature comparing key parameters of CHI/HA film experiments^[70,79,101,108,120]. Asterisks show conditions with confirmed exponential growth. 66

List of Figures

Figure 1-1: Schematic of the general stages in SELEX. An initial library of oligonucleotides consisting of a random region of N nucleotides flanked by two primer regions is incubated with a target of interest. Sequences with affinity for the target will bind. Unbound sequences are partitioned from the target-sequence complexes and discarded. Bound sequences are eluted from the target and amplified to generate the pool for the next cycle. This process is repeated to continually enrich for high affinity sequences. 7

Figure 1-2: Breakdown of the forecasted fertilizer demand for 2016 by nutrient type. Of the 194,132 thousand tonness of fertilizer (N+P+K) expected to be required by 2016, 115,956 thousand tonness (60%) of the demand is for nitrogen. Of potassium and phosphate, 33,163 thousand tonnes (17%) and 45,013 thousand tonnes (23%) are expected respectively (Adapted from [44]). 11

Figure 1-3: Schematic of aptamer-functionalized microcapsules. An encapsulated nitrogen source within a polyelectrolyte multilayer-aptamer microcapsule could be released upon plant demand. Plant starvation signals perceived by the embedded aptamer would trigger a binding event. This binding event, and the corresponding conformational change, would cause a deformation of the polyelectrolyte multilayers and a subsequent change in permeability. This would allow the release of the nitrogen to the plant. 17

Figure 1-4: Schematic of the layer-by-layer assembly method for polyelectrolyte multilayers. A charged substrate (i.e. quartz) is dipped in a polyelectrolyte of opposite charge (purple) where it adheres through electrostatic attraction, effectively reversing the surface charge. The film is rinsed with an appropriate solution to remove excess polyelectrolyte before dipping in the negatively charged polyelectrolyte (green). The negative polyelectrolyte adheres and the surface charge is again reversed. This process is repeated until a film of the desired number of multilayers is achieved. 20

Figure 1-5: Schematic showing charge compensation within a polyelectrolyte bilayer (black). Charges can be paired intrinsically between charged groups on the polyelectrolytes (red). Charged groups unable to participate in intrinsic pairing can be neutralized extrinsically by ions from the surrounding solution—in this case Na^+ and Cl^- (blue). Both are important for the stability of PEMs. 21

Figure 1-6: Schematic comparing the growth mechanisms of films displaying linear and exponential growth. Linear growth (top) follows the classic model of film development where dipping in each PE results in monolayer formation, creating a bilayer at the end of each cycle. In this growth mechanism the thickness of the film increases by the same amount with each deposition step. Exponential growth (bottom) does not grow proportionally. One or more of the PE (red) is able to diffuse into the pre-existing film base during its incubation step. In the subsequent rinse step, some of the PE that had diffused into the film is lost to the rinse solution. Incubation in the PE of opposite charge (blue) results in typical bilayer formation (a), however once the surface charge is reversed, the PE within the film can diffuse back through the film to the surface (b) where it forms additional complexes (c). Hence more than one bilayer is formed per deposition step. The amount of PE that can diffuse into the film is proportional to the pre-existing film thickness and therefore the film grows exponentially thicker with each deposition step. 23

Figure 2-1: Overview of multilayer film composition. A) Schematic of optimized CHI/HA/DNA film. Ten bilayers of CHI (red) and HA (blue) compose the base of the film. Five bilayers composed of CHI and DNA (pink) compose the DNA layers of the film. DNA can represent the incorporation of the SA aptamer or the 29-nt RO. The film then topped with a single bilayer of CHI and HA (capping layer). B) Monomer structures of the PEs used in the film and structure of the target dye SB. C) Sequences of RO (left) and SA (right). Sequences are shown in their predicted secondary structures: a hairpin-loop (RO)(computed by Mfold) and a g-quadruplex (SA) (Adapted from [15]). 32

Figure 2-2: Representative ToF-SIMS sputter profile from a sample set of multilayer films with the general composition of 5 CHI/HA – 5 CHI/DNA – 1 CHI/HA. The depth profile shows the characteristic secondary ions with the greatest signal intensities of a film containing SA DNA after exposure to 2mM SB dye. Ion masses (in g/mol) are shown in brackets. 43

Figure 2-3: Optical image of a multilayer film composed of 5 CHI/HA – 5 CHI/SA – 1 CHI/HA showing the presence of pores within the film (left). The films were subjected to ToF-SIMS surface imaging (156.2 x 156.3 μm^2 area outlined by green box) to determine compositional variations (selected images shown on right). Several characteristic ions were monitored (rounded masses in g/mol given in brackets). Polyelectrolyte specific ions include CHO_2^- (45), CNO^- (42), and C_2HO^- (41). DNA specific ions include PO_2^{3-} (63), and PO_3^{3-} (79). Salt

specific ions include Na^+ (23), and Cl^- (35.5), and substrate specific ions include SiO_2^{2-} (60)..... 45

Figure 2-4: Representative SEM image from a sample set of multilayer films with the general composition of 10 CHI/HA – 5 CHI/DNA – 1 CHI/HA. The image shows a continuous film with no pores for a multilayer film made with SA DNA. 46

Figure 2-5: Analysis of CHI/HA/DNA films after a 5 bilayer increase to the base CHI/HA layers. Top: Optical images of a multilayer films with the general composition of 10 CHI/HA – 5 CHI/DNA – 1 CHI/HA where A) contains SA DNA, B) contains RO DNA, C) contains SA DNA and was exposed to 2mM SB dye, and D) contains RO DNA and was exposed to 2mM SB dye. In all cases, no pores were seen. Bottom: Representative ToF-SIMS sputter profile from the same sample set of multilayer films. The depth profile shows the characteristic secondary ions with the greatest signal intensities of the film containing SA DNA that had no exposure to the target dye. Ion masses (in g/mol) are shown in brackets..... 47

Figure 2-6: Representative AFM image showing surface topography of a $60 \times 60 \mu\text{m}^2$ square from a dry CHI/HA/SA film. A) Height profile of selected area (white line) on a 2D image. Area highlighted in red represents the average peak height value showing the large variation in peak height. B) 3D representation showing overall film morphology..... 48

Figure 2-7: ToF-SIMS sputter profiles of CHI/HA/RO (top) and CHI/HA/SA (bottom) films exposed to 2mM SB dye. The depth profiles shows the characteristic secondary ions generated from each species of interest: CHO_2^- from the CHI/HA matrix, PO_3^{3-} from DNA, and SO_3^{2-} from the SB dye. Ion masses (in g/mol) and shown in brackets..... 53

Figure 2-8: ToF-SIMS sputter profile from the proof of concept work using PSS/PDDA/SA DNA films. These studies aimed to demonstrate the continuing function of the SB aptamer (SA) in binding the target dye (SB) while in a film matrix. The SO_3^{2-} ion was used to track both PSS and the SB dye and the PO_3^{3-} ion was tracked for SA DNA. (A) Films before dye binding showing distinct stratification of PSS/DNA layers within the film. (B) Films after incubation in SB dye. DNA and dye ions show similar temporal trends suggesting co-localization of the dye and DNA within the films. (Reproduced with permission)^[164]..... 54

Figure 2-9: Comparison of the ratio of SO_3^{2-} to PO_3^{3-} intensity counts between CHI/HA/SA and CHI/HA/RO films as an indication of binding. Films were exposed to 2mM SB dye. 55

Figure 2-10: Comparison of the ratio of SO_3^{2-} to PO_3^{3-} intensity counts between CHI/HA/SA and CHI/HA/RO films as an indication of binding. Exposed films were incubated in 200 μM SB dye. Annealed films were heated at 70°C for 10 minutes in 0.15M NaCl. At least two spectra were taken per sample. 56

Figure 2-11: Representative FM images ($\lambda_{\text{em}}=594\text{nm}$) tracking the fluorescence of SB dye in CHI/HA/DNA films made with either SA (right) or RO (left) DNA. Films were prepared by the original method of deposition and were imaged dry. Images represent an area of 602 x 452 μm^2 58

Figure 2-12: Comparison of SB dye binding in CHI/HA/DNA films with either RO (top) or SA (bottom) after exposure to 200 μM SB dye. Images were taken by FM ($\lambda_{\text{em}}=594\text{nm}$) tracking the fluorescence of SB dye. Films were prepared by the original method (left) and modified method (right) of deposition and were imaged dry. Films were not annealed..... 59

Figure 2-13: Comparison of SB dye binding in CHI/HA/DNA films made with either RO (left) or SA (right) that have (bottom) or have not (top) been subjected to heat annealing. Images were taken by FM ($\lambda_{\text{em}}=594\text{nm}$) tracking the fluorescence of SB dye. Films were prepared by the original method of deposition and were imaged dry after exposure to 200 μM SB dye. Images represent an area of 602 x 452 μm^2 61

Figure 2-14: Representative FM images of CHI/HA/6-FAM DNA multilayer films exposed to 200 μM SB dye showing co-localization (Fluorescein-SB overlay; orange) of DNA (Fluorescein; green) and SB dye (SB dye; red) fluorescence as an indication of binding. Films contain either RO DNA (left) or SA DNA (right). Films were prepared using the original method of deposition. Images represent an area of 1048 x 789 μm^2 64

Figure 2-15: Comparison of the average RFP:GFP mean fluorescence ratio between CHI/HA/6-FAM DNA films containing either SA or RO DNA (N=11) as an indication of binding. Films were prepared by the original method of deposition and exposed to 200 μM SB dye. Error bars represent standard deviation. Difference between the ratios is statistically significant ($p<0.05$)..... 65

Figure 2-16: Representative FM images of CHI/HA/6-FAM DNA multilayer films exposed to 200 μ M SB dye showing co-localization (Fluorescein-SB overlay; orange) of DNA (Fluorescein; green) and SB dye (SB dye; red) fluorescence as an indication of binding. Films contain either RO DNA (left) or SA DNA (right). Films were prepared using the modified method of deposition. Images represent an area of 1048 x 789 μ m². 68

Figure 2-17: Comparison of the average RFP:GFP mean fluorescence ratio between CHI/HA/6-FAM DNA films containing SA or RO DNA (N=8) as an indication of binding. Films were prepared by the modified method of deposition and exposed to 200 μ M SB dye. Error bars represent standard deviation. 69

Figure 2-18: UV-Vis spectrophotometry analysis monitoring the growth of CHI/HA bilayers deposited by the original protocol. Growth was measured by tracking the absorbance of CHI and HA between 190-220nm. Three trials were done for each bilayer to account for minor compositional variances. All data is normalized to 300nm. Water rinse was for 5s. Inset: Plot of the average absorbance (N=3) between 190-220nm depicting the growth trend of the CHI/HA film. Error bars represent standard deviation..... 71

Figure 2-19: Plot of the average absorbance between 190-220nm monitoring the growth of CHI/HA bilayers deposited by the modified protocol with increased rinse times, volume, and frequency of solution changes. Three trials were done for each bilayer to account for minor compositional variances. Water rinse was for 1 minute. Error bars represent standard deviation. Inset: Exponential region of the growth curve over bilayers 1 to 6..... 73

Figure 2-20: Plot of the average absorbance between 190-220nm monitoring the growth of CHI/HA bilayers deposited by an adaptation of the modified protocol where the rinses were changed with every use (FS protocol). Three trials were done for each bilayer to account for minor compositional variances. Water rinse was for 10s. Error bars represent standard deviation. Inset: Exponential region of the growth curve over bilayers 1 to 8..... 74

Figure 2-21: Plot of the average absorbance between 190-220nm monitoring the growth of CHI/HA bilayers deposited by an adaptation on the modified protocol with increased rinse volumes (Mulligan protocol). Three trials were done for each bilayer to account for minor compositional variances. Water rinse was for 1 minute. Error bars represent standard deviation..... 76

Figure 2-22: Plot of the average absorbance between 190-220nm monitoring the growth of CHI/HA bilayers deposited by an adaptation of the modified protocol with increased rinse volumes, times, and number (Richert protocol). Three trials were done for each bilayer to account for minor compositional variances. Water rinse was for 10 seconds. Error bars represent standard deviation..... 76

Figure 2-23: Schematic of a two bilayer film system on a substrate (deposited by dipping method) showing potential pathways for light to travel through a film (red). Refractive indices (n) are assumed to be different..... 79

Figure 2-24: Schematic of linear growth mechanism for CHI/HA films; (a) Film is thin enough to allow diffusion of CHI in and out of the film (zone I) (b) Film grows according to the exponential mechanism where CHI diffuses out of the film to double its size (c) Film becomes thick enough and cannot dispense the entire over-saturated CHI reservoir in the allotted time and CHI becomes trapped within the matrix (zone II emerges) (d) Diffusion zone (zone I) will always become saturated with CHI. CHI down to a certain depth from the solution interface will escape to complex with HA to become new bilayer(s) and expand zone I. The part of zone I that is deeper in the film matrix will retain its free CHI and become part of zone II. Therefore, the thickness of zone I will remain constant while zone II grows..... 82

Figure 2-25: UV-Vis spectrophotometry analysis monitoring the growth of CHI/RO bilayers on a base of 5 CHI/HA bilayers by measuring the absorbance of RO DNA at 260nm. Concentration of all PEs used was 2mg/mL. All data is normalized to 300nm. Films were rinsed briefly with dH₂O before each analysis.. 85

Figure 2-26: UV-Vis spectrophotometry analysis monitoring the growth of CHI/SA bilayers on a base of 5 CHI/HA bilayers by measuring the absorbance of SA DNA at 253nm. Films were grown according to the original method using PE concentrations of 1mg/mL. Three trials were done for each bilayer to account for minor compositional differences. All data is normalized to 350nm. Water rinse was for 5s. Inset: Plot of average absorbance (N=3) at 253nm depicting the growth of the CHI/SA bilayers. Error bars represent standard deviation. 87

Figure 2-27: UV-Vis spectrophotometry analysis monitoring the growth of CHI/SA bilayers on a quartz substrate by measuring the absorbance of SA DNA at 253nm. Films were grown according to the original method using PE concentrations of 1mg/mL. Three trials were done for each bilayer to account for

minor compositional differences. All data is normalized to 350nm. Water rinse was for 5s. Inset: Plot of average absorbance (N=3) at 253nm depicting the growth of the CHI/SA bilayers. Error bars represent standard deviation. 87

Figure 2-28: UV-Vis spectrophotometry analysis monitoring the growth of CHI/SA bilayers on a base of 5 CHI/HA bilayers by measuring the absorbance of SA DNA at 253nm. Films were grown according to the original method using PE concentrations of 2mg/mL. Three trials were done for each bilayer to account for minor compositional differences. All data is normalized to 350nm. Water rinse was for 5s. Inset: Plot of average absorbance (N=3) at 253nm depicting the growth of the CHI/SA bilayers. Error bars represent standard deviation. 88

Figure 2-29: UV-Vis spectrophotometry analysis monitoring the growth of CHI/SA bilayers on a quartz substrate by measuring the absorbance of SA DNA at 253nm. Films were grown according to the original method using PE concentrations of 2mg/mL. Three trials were done for each bilayer to account for minor compositional differences. Water rinse was for 5s. Inset: Plot of average absorbance (N=3) at 253nm depicting the growth of the CHI/SA bilayers. Error bars represent standard deviation. 88

Figure 2-30: UV-Vis spectrophotometry analysis monitoring the growth of CHI/RO bilayers on a base of 5 CHI/HA bilayers by measuring the absorbance of RO DNA at 260nm. Films were grown according to the original method using PE concentrations of 1mg/mL. Three trials were done for each bilayer to account for minor compositional differences. All data is normalized to 350nm. Water rinse was for 5s. Inset: Plot of average absorbance (N=3) at 260nm depicting the growth of the CHI/RO bilayers. Error bars represent standard deviation. 90

Figure 2-31: UV-Vis spectrophotometry analysis monitoring the growth of CHI/RO bilayers on a quartz substrate by measuring the absorbance of RO DNA at 260nm. Films were grown according to the original method using PE concentrations of 1mg/mL. Three trials were done for each bilayer to account for minor compositional differences. All data is normalized to 350nm. Water rinse was for 5s. Inset: Plot of average absorbance (N=3) at 260nm depicting the growth of the CHI/RO bilayers. Error bars represent standard deviation. 90

Figure 2-32: UV-Vis spectrophotometry analysis monitoring the growth of CHI/RO bilayers on a base of 5 CHI/HA bilayers by measuring the absorbance of RO DNA at 260nm. Films were grown according to the original method using PE concentrations of 2mg/mL. Three trials were done for each bilayer to account for

minor compositional differences. All data is normalized to 350nm. Water rinse was for 5s. Inset: Plot of average absorbance (N=3) at 260nm depicting the growth of the CHI/RO bilayers. Error bars represent standard deviation. 91

Figure 2-33: UV-Vis spectrophotometry analysis monitoring the growth of CHI/RO bilayers on a quartz substrate by measuring the absorbance of RO DNA at 260nm. Films were grown according to the original method using PE concentrations of 2mg/mL. Three trials were done for each bilayer to account for minor compositional differences. All data is normalized to 350nm. Water rinse was for 5s. Inset: Plot of average absorbance (N=3) at 260nm depicting the growth of the CHI/RO bilayers. Error bars represent standard deviation. 91

Figure 3-1: Common aptamer modifications to improve lifetime and resistance against nuclease-mediated degradation. (A) Native RNA structure (note: modifications can also be applied to DNA). (B) Modification to 5'-end of sequence with molecules like polyethylene glycol (PEG) and cholesterol prevent premature clearance from biological systems. (C) Modification of the 2'-(O)H with groups such as fluorine (F), amino (NH₂) or O-methyl (OCH₃) aids against nuclease degradation (blue). Phosphorothioate linkages (where a non-bridging O is replaced by an S dramatically increases nuclease resistance (red). Capping of the 3'-end by inversion of the 3'-nucleoside to create 5'—5' oligonucleotides is highly effective at preventing degradation due to 3'-exonucleases (pink). (Adapted from [141])..... 98

Figure 3-2: Comparison of 6-FAM SA digestion by Nuclease S₁ over varying times (0 to 10 minutes) at 37°C (top) and at RT (bottom) and then analyzed on a 12% PAGE gel. Reactions were stopped with the addition of 70°C EDTA and a 10 minutes incubation at 70°C. Size controls consisted of undigested 6-FAM SA DNA (29nt) and an 18nt fluorescently labeled DNA sequence. Gels were imaged at 302nm by monitoring the fluorescence of fluorescein..... 110

Figure 3-3: Comparison of 6-FAM SA digestion by Nuclease S₁ over varying times (0 to 5 minutes) using 10U (left) or 1U (right) of nuclease at RT. Samples were analyzed on a 12% PAGE gel using the fluorescence of fluorescein. Reactions were stopped with the addition of 70°C EDTA and a 10 minutes incubation at 70°C. Size controls consisted of undigested 6-FAM SA DNA (29nt) and an 18nt fluorescently labeled DNA sequence. 111

Figure 3-4: Comparison of 6-FAM SA digestion by Nuclease S₁ over varying times (0 to 5 minutes) using 10U (left) or 1U (right) of nuclease at RT. Samples were analyzed on a 19% PAGE gel using the fluorescence of fluorescein.

Reactions were stopped with the addition of 90°C EDTA and a 10 minutes incubation at 90°C. Size controls consisted of undigested 6-FAM SA DNA (29nt) and an 18nt fluorescently labeled DNA sequence. 111

Figure 3-5: Digestion of 6-FAM SA DNA by Nuclease S₁ over varying times (0 to 30 minutes) using 0.1U of nuclease at RT. Samples were analyzed on a 19% PAGE gel using the fluorescence of fluorescein. Reactions were stopped with the addition of 90°C EDTA and a 10 minutes incubation at 90°C. Size controls consisted of undigested 6-FAM SA DNA (29nt) and an 18nt fluorescently labeled DNA sequence. 112

Figure 3-6: Comparison of 6-FAM SA digestion by Nuclease S₁ over varying times (0 to 30 minutes) using 1U (left) or 0.5U (right) of nuclease at RT. Samples were analyzed on a 19% PAGE gel using the fluorescence of fluorescein. Reactions were stopped with the addition of 90°C EDTA and a 10 minutes incubation at 90°C. Size control consisted of undigested 6-FAM SA DNA (29nt). 113

Figure 3-7: Comparison of 6-FAM SA digestion by Nuclease S₁ after 60 minutes using 1U or 0.5U of nuclease at RT. Samples were analyzed on a 19% PAGE gel using the fluorescence of fluorescein. Reactions were stopped with the addition of 90°C EDTA and a 10 minutes incubation at 90°C. Size controls consisted of undigested 6-FAM SA DNA (29nt) and an 18nt fluorescently labeled DNA sequence. 113

Figure 3-8: Schematic of PAGE-based nuclease assay. (A) A CHI/HA/6-FAM SA film is prepared. (B) Film is exposed to Nuclease S₁ (orange circles). Nuclease either permeates the film to digest the DNA (right) or does not leaving the DNA intact (left). (C) Film matrix is degraded by chitosanase (green) and hyaluronidase (pink), releasing the DNA into solution. (D) DNA integrity is analyzed by PAGE gel for restriction fragments using the fluorescence of fluorescein. 114

Figure 3-9: Comparison of 6-FAM SA digestion by Nuclease S₁ between films with different compositions after 60 minutes using 0.5U of nuclease at RT. Washes from the nuclease assay for each film type were analyzed on a 12% PAGE gel using the fluorescence of fluorescein. Size control consisted of undigested 6-FAM SA DNA (29nt)..... 116

Figure 3-10: Gel formed in nuclease assay rinses upon drying down by SpeedVac before PAGE gel analysis. 117

Figure 3-11: Preliminary study of the change in the average mean fluorescent intensity of CHI/HA/6-FAM SA films (N=9) with and without a capping layer after each hour-long exposure to Nuclease S₁. All films were made using the original method. Fluorescence retained was calculated as the percentage of the average mean fluorescent intensity (as calculated by ImageJ) retained from the baseline fluorescence (before nuclease exposure)..... 118

Figure 3-12: Change in the average mean fluorescent intensity of CHI/HA/6-FAM SA films (N=16) with and without a capping layer after each hour-long exposure to Nuclease S₁. Control film was uncapped and exposed to the assay process without addition of nuclease (N=8). All films were made using the original method. Fluorescence retained was calculated as the percentage of the average mean fluorescent intensity (as calculated by ImageJ) retained from the baseline fluorescence (before nuclease exposure). 119

Figure 3-13: Fluorescence measurements of film washes after each nuclease digestion of CHI/HA/6-FAM SA films with and without a capping layer analyzing for DNA loss from the films. Control film was uncapped and exposed to the assay process without addition of nuclease. All films were made using the original method. The presence of DNA was monitored by the fluorescence of fluorescein (Ex=490nm)..... 120

Figure 3-14: Change in the average mean fluorescent intensity of CHI/HA/6-FAM SA films (N=8) with and without a capping layer after each hour-long exposure to Nuclease S₁. Control film was uncapped and exposed to the assay process without addition of nuclease (N=8). All films were made using the modified method. Fluorescence retained was calculated as the percentage of the average mean fluorescent intensity (as calculated by ImageJ) retained from the baseline fluorescence (before nuclease exposure). 121

Figure 3-15: Fluorescence measurements of film washes after each nuclease digestion of CHI/HA/6-FAM SA films with and without a capping layer analyzing for DNA loss from the films. Control film was uncapped and exposed to the assay process without addition of nuclease. All films were made using the modified method. The presence of DNA was monitored by the fluorescence of fluorescein (Ex=490nm)..... 122

List of Abbreviations

| | |
|-------|--|
| 6-FAM | 6-carboxyfluorescein phosphoramidate |
| AFM | atomic force microscopy |
| BSA | bovine serum albumin |
| CHI | chitosan |
| DA | degree of acetylation |
| DNA | deoxyribonucleic acid |
| dsDNA | double stranded deoxyribonucleic acid |
| EDTA | ethylenediaminetetraacetic acid |
| EtBr | ethidium bromide |
| FM | fluorescent microscope |
| FS | fresh-solution |
| HA | hyaluronan |
| K_d | dissociation constant |
| LB | Langmuir-Blodgett |
| LBL | layer-by-layer |
| PAGE | polyacrylamide gel electrophoresis |
| PAH | poly(allyamine hydrochloride) |
| PDDA | poly(diallyldimethylammonium chloride) |
| PE | polyelectrolyte |
| PEM | polyelectrolyte multilayer |

| | |
|--------|---------------------------------------|
| pKa | acid dissociation constant |
| PGA | poly(L-glutamic acid) |
| PLL | poly(L-lysine) |
| PSS | poly(sodium styrene sulfonate) |
| RMS | root-mean-square |
| RO | random oligomer |
| RT | room temperature |
| rxn | reaction |
| SA | sulforhodamine B aptamer |
| SB | sulforhodamine B dye |
| SEM | scanning electron microscopy |
| ssDNA | single stranded deoxyribonucleic acid |
| TEMED | N,N,N',N'-tetramethylethylenediamine |
| TLC | thin layer chromatography |
| UV-Vis | ultraviolet-visible spectrophotometry |

Chapter 1. Introduction

1.1. Nanomaterials

Research and development in nanotechnology (including nanomaterials, nanotools, and nanodevices) has become increasingly popular in the past decade receiving upwards of \$1.8 billion in funding as of 2010 in the US alone^[1,2]. Between 1996 and 2008, an estimated 399, 831 articles have been published involving nano-research^[3]. Publication in this field has increased dramatically, with four-times more articles produced between 2008 and 2009 than published in 1998^[2]. While still dominated by the field of surface chemistry, nanotechnology has become quite interdisciplinary and now represents an amalgamation of many fields including physics, chemistry, biotechnology, materials science, and engineering^[1,2].

There is no formal definition summing up the overwhelming number of properties and functionalities possessed by nanomaterials into one cohesive idea. Instead, they are generally described as materials of one or more components with at least one dimension between 1 and 100nm^[1]. As a result of their size, nanoparticles exhibit some very unique properties. As a nanoparticle gets smaller, the atoms at the surface of the nanoparticle become a major proportion of the atoms that make up the nanoparticle as a whole^[4]. These surface atoms behave differently than those that make up the core, and because they compose a high percentage of the nanoparticle they can dramatically influence the physical and chemical behavior of the nanoparticle to reflect their

own^[4]. As a result, the nanoparticle (which is a collection of atoms) behaves more like a particle than bulk matter^[5]. On top of this, shape (i.e. rod, spherical), aggregation behavior, surface composition (i.e. charge, functionalization), concentration, bulk composition (i.e. Au, C, silica), and active properties (i.e. ability to change behavior in response to environmental cues such as pH) all influence the characteristics of a given nanomaterial^[4]. These unique properties include altered color, magnetism, and optical properties; increased strength, flexibility, and reactivity; and improved electrical conductivity and absorption^[6]. A good example of this phenomenon (as laid out by Roduner) is gold^[5]. In bulk, gold is a yellow, non-reactive, non-magnetic metal with a melting temperature of 1336K. However, on the nanoscale these properties quickly change. Gold particles 10nm in size appear red as they are able to absorb green light. As they get smaller (2-3nm), they become reactive and magnetic. Smaller than this, and they develop properties characteristic of insulators. As gold particles decrease in size, the temperature at which they melt also decreases. Gold particles 2.5nm in size have a reported melting temperature of 930K.

Aside from nanoparticles, nanomaterials also include nanotubes, films, hydrogels, nanofibres, liposomes, quantum dots, as well as countless others^[7,8]. Certain nanomaterials have been produced in large-scale quantities for use in industry for years^[1]. Carbon blacks used for rubber and pigment production fall within the nano-range as do fumed silica, and oxides of titanium, alumina, and zirconia which are used in pigment, cosmetic, and microelectronic industries. Newer applications include plastic fillers, sunscreen agents countering UV rays,

antibacterial coatings and textiles, marine anti-fouling agents, electronics, and catalytic roles in mechanical parts such as catalytic converters^[9]. The majority of nanomaterials used currently in industry are synthetic in nature, however the use of biomaterials (i.e. enzymes, oligonucleotides, natural polymers) is becoming more commonplace in research and demonstrates great potential for fields such as therapeutics, controlled delivery, diagnostics, agriculture, and tissue engineering^[10,11,12, 13]. With novel and innovative applications in nanotechnology research advancing rapidly with each additional year, the future prospects of these materials are promising.

1.2. Aptamers

Aptamers, from the Latin word *aptus* meaning “to fit”, are single-stranded oligonucleotides (RNA or DNA) that fold into 3D nanoscale structures which enable them to bind a specific molecule with high affinity and selectivity^[14]. Aptamers have been selected for a wide range of targets including dyes^[15], small molecules^[16], mycotoxins^[17], enzymes^[18], antibiotics^[19], and viruses^[20]. Interactions between aptamers and their targets are extremely specific and the change of a single chemical group can cause a decrease in affinity as was seen in the classical example of theophylline aptamer^[21]. Theophylline and caffeine differ by a single methyl group however the difference in affinity of the theophylline aptamer for each is 10000-fold^[21]. Aptamers are often referred to as “chemical antibodies” due to their molecular recognition capabilities and *in vitro*

selection^[14]. The affinity of an aptamer for its target is comparable to that seen in antibodies, with dissociation constants (K_d) ranging from micromolar to picomolar^[22]. However, aptamers also have several more advantages over protein-based macromolecules possessing target-specific binding properties such as antibodies and enzymes. Selection does not rely on generating an immune response in animals (as for antibody production) and therefore aptamers can be generated for species that cause difficulties in animal systems such as toxins and molecules that do not easily elicit immune responses^[14]. Therefore, aptamers can theoretically be generated for any target. In addition to this, aptamers themselves do not generally elicit immune responses at therapeutic concentrations, making them promising candidates for new clinical therapies^[23]. Because of the manner in which they are selected, protein-based receptor molecules are limited to a very narrow set of conditions (physiological) in which they can remain functional^[24]. Outside of these conditions they are irreversibly denatured. Oligonucleotides are fairly resilient to harsh conditions and therefore aptamers can be used in a wide range of environments without losing their binding abilities including non-physiological conditions^[24]. As a result, they also tend to have long shelf- lives^[14]. Once the sequence of an aptamer is known they can be synthesized with high purity and reproducibility^[14].

Aptamers are selected by an *in vitro* process called Systematic Evolution of Ligands by Exponential Enrichment (SELEX). The first accounts of *in vitro* selection of oligonucleotides with the ability to bind a specific target were published in 1990 by three different groups. Authors Robertson and Joyce

introduced mutations in the Tetrahymena ribozyme and selected a novel sequence which could cleave ssDNA^[25]. Tuerk and Gold randomized 8-nt of an RNA sequence known to bind T4 DNA polymerase^[26]. The selection they formed with this RNA library yielded a sequence with affinity for T4 DNA polymerase superior to the original. Through this study the term SELEX was coined which now describes the process by which most aptamers are generated. Finally, Ellington and Szostak performed an *in vitro* selection against organic dyes using a randomized library of RNA sequences yielding novel sequences with affinity for those targets^[27]. This method (and variations on it) has evolved to be the modern method of SELEX^[26].

There are typically two stages in aptamer development: (1) selection of a sequence from an oligonucleotide library using SELEX and (2) reduction of the sequence to its minimal structure (called “minimer”)^[24]. The second stage can be optional. SELEX begins with a random library of 10^{14} to 10^{15} oligonucleotide sequences which are designed as a set number of random nucleotides (typically 20-80nt) flanked by two primer binding regions (See Figure 1-1)^[14,28]. The library is incubated with the target of interest where sequences with some level of affinity for the target will bind. The unbound sequences will be partitioned away from the target-sequence complexes and discarded. Some common methods of partitioning include nitrocellulose filtration, affinity chromatography, and gel-mobility shift assays^[29]. Target-bound sequences will be eluted from the target molecules usually by methods involving affinity (higher concentrations of the target), heat, or denaturants^[29]. The eluted sequences are amplified using

techniques like polymerase chain reaction (PCR) to generate the library pool for the next cycle. SELEX is an iterative process, usually consisting of 8-12 cycles, which continually works to enrich the library with sequences of highest affinity for the target. At the end, the remaining sequences (aptamers) are cloned and sequenced for further characterization (i.e. K_d , minimizer determination). Different types of SELEX will perform each step slightly differently in a manner appropriate for the type of selection and target of interest. Selections can also include additional steps such as negative selection, usually in the cases where a solid support matrix is involved in the method. This eliminates sequences in the library pool that have affinity for any other material other than the target. Counter selections may also be performed to eliminate library sequences that have affinity for molecules that are structurally similar to the target (ensure high selectivity).

After selection, some additional characterizations can be performed. Generally, the K_d , which quantifies the affinity of the aptamer for the target, will be determined^[29]. The method by which this is calculated depends on the nature of the target of interest (i.e. size, natural fluorescence) but common techniques include fluorescence polarization and filtration. Additionally, the minimal structure can be found. An aptamer can be 80 to 100 nucleotides or longer, however usually only 10 to 15 nucleotides are in direct contact with the target (binding regions)^[24]. Other nucleotides may not be involved in binding but play a supportive role in maintaining the conformation of the binding region(s)

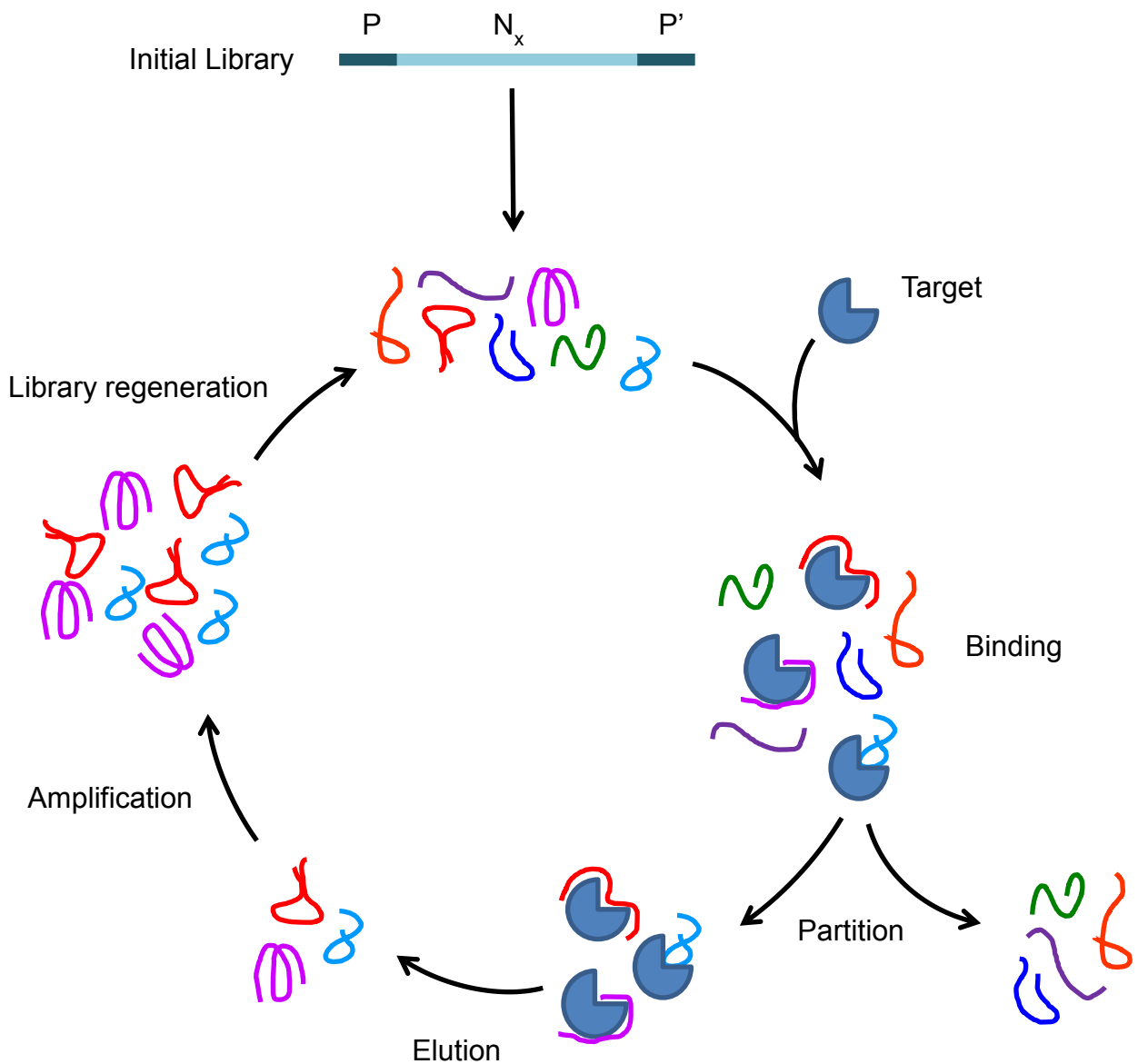


Figure 1-1: Schematic of the general stages in SELEX. An initial library of oligonucleotides consisting of a random region of N nucleotides flanked by two primer regions is incubated with a target of interest. Sequences with affinity for the target will bind. Unbound sequences are partitioned from the target-sequence complexes and discarded. Bound sequences are eluted from the target and amplified to generate the pool for the next cycle. This process is repeated to continually enrich for high affinity sequences.

(facilitating regions). These two regions typically compose 25 to 40 nucleotides of the originally sequence. The remaining nucleotides do not fit into either of the regions discussed above (non-essential regions) and their removal will have no

effect on target binding. Minimer characterization can be done through computational studies, methods analyzing for binding loss (i.e. mutational studies, hybridization with complementary oligonucleotides), or fingerprinting methods (enzymatic or chemical)^[24]. Nonessential regions may not exist within the aptamer and their removal is not required for adequate binding, but determining the minimal structure can have positive effects. Removing nonessential regions can help improve the affinity of the aptamer by reducing steric hindrance^[24,30]. Smaller aptamers may be more ideal for downstream applications (i.e. small-dimension nanostructures)^[24]. Finally, smaller sequences are cheaper to synthesize with better yields than longer products, which tend to become more difficult after 60 nucleotides^[24].

As virtually any molecule can serve as a target, aptamers have received considerable attention in many fields and continues to gain popularity. The therapeutic and diagnostic market for aptamer technology alone is estimated to be worth ~1.8 billion by 2014^[26]. Naturally, the molecular recognition properties of aptamers have generated many applications in therapeutic and clinical applications. Although the age-related macular degeneration therapeutic Pegaptanib (also known as Macugen), has been the only FDA approved aptamer for clinical treatment, other aptamer-based therapeutics are in various stages of pre-clinical and clinical trials^[26]. For example, the REG1 system consists of an RNA aptamer, pegnivacogin, which binds factor IXa (key player in coagulation onset) as well as a complementary component, anivamersen, which counteracts pegnivacogin activity^[31]. The interplay between the aptamer and its target

combined with the interaction of the inhibitor and the aptamer, allows for a balance to be achieved between complete coagulation and inhibition of coagulation (bleeding events). The efficiency of inhibition also ensures that rapid reversal of the anticoagulation effects is achievable if required. This system is currently in Phase II of clinical trials and shows great promise in controlling anticoagulation in acute coronary syndromes. Aside from therapeutics, aptamers have also been used as biosensors on various detection platforms including electrodes^[32], gold nanoparticles^[33], quartz-crystal microbalance^[34], and microfluidic devices^[35]. More recently, aptamers have been integrated into nanomaterials to generate novel “smart” composites that combine the functionality of the nanomaterial with the binding properties of the aptamer^[36,37]. The versatility of aptamer technology will continue to generate novel applications in a wide variety of fields.

1.3. Smart Fertilizers

1.3.1. Challenges in Agriculture

The advent of chemical fertilizers revolutionized agricultural practices and is essential to the crop yields achieved today. Application of these chemicals regenerates nutrient-poor soils and permits large-scale crop growth to be achieved annually^[38]. Nitrogen is an essential nutrient for plant growth as a central element in nucleic acids and proteins, making up 1.5 to 5% of the dry weight in plants^[39]. Despite the abundance of atmospheric nitrogen (in the form of N₂), soils are generally deficient of the nitrogen species usable by plants (NO₃⁻,

NH_4^+). In agriculture, these species are generally produced by specific soil bacteria in a process called nitrogen fixation, where elemental nitrogen is converted to ammonia^[40]. The ammonia can then be oxidized to nitrate by soil bacteria in a process called nitrification^[41]. However, these natural processes cannot keep up with human crop demands. In 1909, Fritz Haber discovered a method to fix atmospheric nitrogen into ammonia with hydrogen in the presence of iron under high pressures and temperatures^[38,42]. Later, Carl Bosch determined how to perform this reaction on an industrial scale^[42]. As a result, large-scale production of nitrogen commenced and the chemical fertilizer market boomed. The increased crop yields as a result of this technology allowed the global population to grow from 1.6 billion to 6 billion in the 20th century^[38]. However, what could not be accounted for were the economic and environmental impacts of increased fertilizer use.

Presently, the agricultural sector is struggling with the consequences of fertilizer overuse. Lack of new arable soils and reduction of fertile farmland due to encroaching urbanization adds continuing pressure for increased produce yields and efficiency from existing agricultural operations^[43]. As a result, more chemical fertilizers are used to meet food demands required to sustain the growing population which is estimated to be 9 billion by 2050. The world fertilizer (N+P+K) demand is expected to increase by 1.9% by 2016 equaling a global requirement of 194.1 million tonnes of fertilizer^[44]. Of this, 60% of the demand is for nitrogen (See Figure 1-2). With dwindling petroleum resources, the cost of fertilizer production, transportation of fertilizer and produce, and food

are rising, impacting farmer and consumer alike^[43,44]. In addition to this, the global market is now turning to agriculture to produce biofuels creating a negative impact cycle on agriculture and fuel markets. Fertilizers are still required to achieve yields necessary for sufficient biofuel production. Corn and sugarcane continue to be the leading crops for biofuel production, producing the most biofuel per acre; however they consumes high amounts of nitrogen^[45].

The overuse of chemical fertilizers has health and environmental consequences as well. Of the nitrogen applied, 50 to 70% is lost to the surrounding environment^[46]. The majority of this nitrogen is leached into water systems causing severe environmental and human health effects. Nitrogen pollution into coastal waters has increased 6 to 8-fold in the USA, 4 to 5-fold in the Gulf of Mexico, and 6 to 20-fold in the North Sea region between 1966 and 2006, and is likely much higher as of today^[47]. Nitrate is the most common

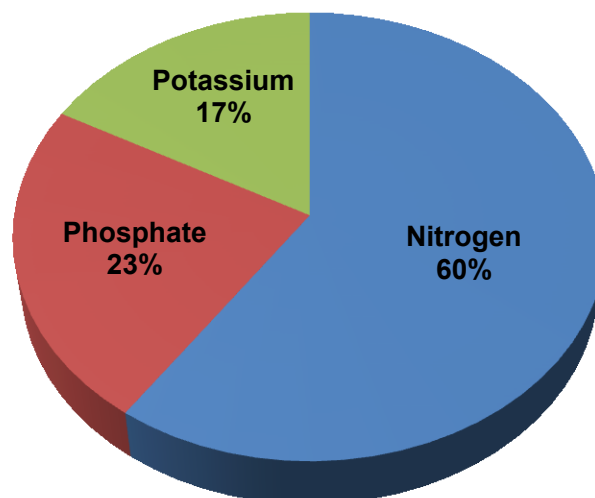


Figure 1-2: Breakdown of the forecasted fertilizer demand for 2016 by nutrient type. Of the 194,132 thousand tonnes of fertilizer (N+P+K) expected to be required by 2016, 115,956 thousand tonnes (60%) of the demand is for nitrogen. Of potassium and phosphate, 33,163 thousand tonnes (17%) and 45,013 thousand tonnes (23%) are expected respectively (Adapted from [44]).

chemical pollutant of global groundwater reserves commonly from fertilizer runoff in rural communities and human waste in urban settings^[48]. Ingestion of nitrate-contaminated water has been shown to contribute to cases of methemoglobinemia—conversion of hemoglobin to methemoglobin as a result of binding nitrite (oxidized nitrate)—which interferes with the oxygen-carrying capacity of the blood. Many adult cases have been reported however, this condition is especially dangerous to infants^[47,48]. Human consumption of nitrate has also been implicated in many cancers (esophagus, colon, bladder, lymphatic, and stem cell), thyroid disease, increased blood pressure, and increased risk for abortion, acute respiratory tract infection, and Alzheimer's disease^[38,47,48]. It has also been suggested that elevated levels promote the growth of allergen-causing plants and promote the spread of infectious diseases such as malaria, cholera, schistosomiasis, and West Nile virus by increasing the growth of food plants of carrier species or by recruiting hosts to the area^[38]. Nitrogen can also feed toxic bacterial species causing dangerous contamination of drinking and recreational waters^[47]. Environmentally, increased levels of reactive nitrogen species (NH_4^+ , NO_2^- , NO_3^-) allow for rapid growth of primary producers including phytoplankton, benthic algae, and macrophytes resulting in altered organism balances such as algal-blooms^[38,47]. Algal-blooms increase cloudiness and shading in water systems which blocks sunlight from reaching aquatic plant life causing eventual death and loss of habitat for food, growth, and reproduction^[49]. Rapidly growing bloom-species, some of which are capable of producing toxic metabolites, consume extremely large amounts of dissolved oxygen to feed their growth.

Affected water systems become increasingly anaerobic, often causing mass mortality events in fish and invertebrates.

In addition to this, reactive nitrogen has effects on biodiversity loss, climate change, and acidification of ecosystems. Nitrogen pollution has been ranked as one of the top three threats to biodiversity worldwide^[38]. Excess nitrogen allows nitrogen-sink plant species to outcompete slow-harvesting plant species whose biological mechanisms cannot take advantage of the excess nitrogen and rapidly increase growth. By-products of fertilizer nitrogen, such as nitrogen monoxide (NO) and nitrogen dioxide (NO₂) are contributors of ground level ozone and nitrous oxide (N₂O) is becoming a prevalent greenhouse gas contributing to climate change and poor air quality^[38]. In the past, acidification of water ecosystems has largely been attributed to sulfur dioxide emissions which get converted to sulfuric acid in the atmosphere^[47]. However, it is becoming recognized that nitrogen species (NO₂, NO) also play a part and undergo a similar conversion to nitric acid. While there has been a global effort to reduce SO₂ emissions, no such regulations have been implemented for these nitrogen species^[47]. As a result, acidification effects from nitric acid continue to damage aquatic ecosystems and effects will only get worse with increased application of nitrogen-containing fertilizers. Acidification changes the delicate balance of water ecosystems and has a large impact on the lifecycles and activity of microorganisms, plants, invertebrates (crustaceans, gastropods, leeches) and fish^[47].

Simply increasing nitrogen production to continue meeting demands is not an option anymore and the need for more efficient methods is clear.

Development of new technologies that increase productivity by conserving land and water resources and increase yields with equal or less input than current methods are required to address the current economic and environmental issues^[43].

1.3.2. An Aptamer-based Approach

Novel fertilizers have been developed to increase the efficiency of chemical fertilizers. A plethora of slow-release approaches have been developed to provide sustained release of nutrients to crops over a period of time. Coated fertilizers release water-soluble fertilizer based on a diffusion gradient or through the developments of defects (i.e. cracks)^[50]. Certain sulfur-coated fertilizers only release their contents after the coating is degraded by microbes. Polymers of urea-aldehydes (formaldehyde, isobutylidenediurea, crotonylidenediurea) use microbial activity to release urea with tunable degradation rates based on degree of polymerization, pH, temperature and granule size^[50]. While these approaches have improved upon current fertilizer application, the efficiency of fertilizers can be improved even further. Synchronization of nutrient release with plant uptake could reduce applied nitrogen and prevent loss of nitrogen to the environment without impacting crop yields providing long lasting economic and environmental benefits. Nanotechnology may be able to provide the next step in fertilizer

technology. Already, new approaches for fertilizers using nanomaterials such as hydrogels^[51], clay nanoparticles^[52], and chitosan nanoparticles^[53] are being developed. However, these approaches still focus on slow release rather than “smart” release.

Aptamers are very promising in the field of molecular recognition and compatibility with nanomaterials. Together, their combined properties may provide the technological advance to enable dynamic responses to environmental cues—hence “smart” nanomaterials. In this case, aptamer-functionalized fertilizer vessels would respond to plant exudates signaling nitrogen deficiency to deliver the needed nutrient. Crop plants have been demonstrated to release starvation signals into the surrounding soils when in need of specific nutrients^[54]. These signals are generally low molecular weight compounds including amino acids, organic acids, sugars, and phenolics^[55]. The type and amount of exudate released depends on the age and species of plant, and the environmental stresses (biotic and abiotic). Release of 5-deoxystrigol (member of the strigolactone family) by sorghum roots was demonstrated to increase 30-fold and 20-fold for plants grown under low-phosphorous and low-nitrogen conditions, respectively^[56]. Phosphorous deficient sugar beet plants released 5-times more exudates to the surrounding soils compared to plants grown under high phosphorous conditions^[57]. The major species released were organic acids—salicylic and citramalic acid—which were theorized to enable the mobilization of phosphorous in soils by chelating iron that was associated with phosphorous. The role, regulation, and mechanisms behind the release of

exudates are not fully understood and investigations are just beginning to emerge^[55]. In addition to increased nutrient mobilization, other studies have suggested that the release of certain exudates can help maintain a beneficial soil pH or change the pH to help solubilize forms of the required nutrient with limited solubility^[58]. Others hypothesize that they can foster positive or negative interactions with surrounding organisms such as aiding microbial growth or inhibiting the growth of competing plant species^[59]. Taking advantage of these signals could help create a fertilizer system capable of responding to the nutritional needs of crop plants. Aptamers embedded in polyelectrolyte multilayers (PEMs) could enable a microcapsule system to perceive plant starvation signals for nitrogen and release the nutrient to the plant when it is required (See Figure 1-3). Small molecules, such as root exudates, could diffuse through PEMs to reach embedded aptamers and trigger a binding event. The resulting deformation of the PEMs layers from the aptamer-target interaction will in turn induce a change in permeability, allowing the encapsulated nitrogen source to be released to the plant. Aptamers have already been shown to retain their binding properties and alter permeability in polyelectrolyte multilayer films and microcapsules using synthetic polymers and the sulforhodamine B aptamer^[36,37]. In addition to this, embedding the aptamer within PEMs could serve as a protective coating against nuclease-mediated degradation. This approach could also be applied for the controlled release of herbicides, pesticides, as well as other agriculturally significant chemicals used for crop enhancement. New systems using biodegradable and biocompatible PEMs,

such as chitosan (CHI) and hyaluronan (HA) could offer environment friendly fertilizers systems able to reduce nitrogen application and increase the efficiency of chemical fertilizers using smart and responsive mechanisms.

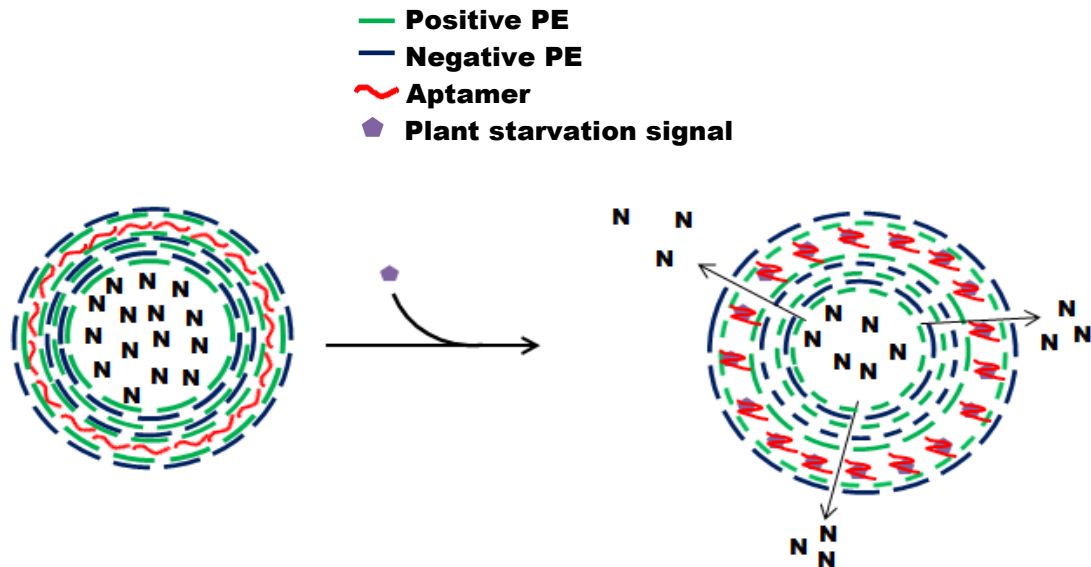


Figure 1-3: Schematic of aptamer-functionalized microcapsules. An encapsulated nitrogen source within a polyelectrolyte multilayer-aptamer microcapsule could be released upon plant demand. Plant starvation signals perceived by the embedded aptamer would trigger a binding event. This binding event, and the corresponding conformational change, would cause a deformation of the polyelectrolyte multilayers and a subsequent change in permeability. This would allow the release of the nitrogen to the plant.

1.4. Polyelectrolyte Multilayers (PEMs)

Multilayer films are fabricated by sequential absorption of polymers in an alternating pattern onto a given substrate to form a stratified film. These films can be constructed using Langmuir-Blodgett (LB) or layer-by-layer (LBL) assembly methods^[60]. LB assembly was developed by Katherine Blodgett in 1934 who described the transfer of Langmuir monolayers to a glass plate^[61]. Langmuir monolayers consist of amphiphilic molecules (polar head, nonpolar tail)

which arrange themselves at a water-air interface with their nonpolar regions sticking into the air. When a substrate is dipped, a monolayer of molecules is transferred to the surface^[62]. With subsequent repeat of this dipping process, multilayers are built with alternating head-to-head/tail-to-tail arrangement. LB has several disadvantages despite being able to produce multilayer films. The technique itself is time consuming and requires expensive equipment to perform^[60]. It also requires amphiphilic molecules thereby limiting the materials that can be used^[60]. Therefore, the LBL method of assembly was used to make films. This method is much simpler and faster, requiring only a beaker to perform, and does not have the same material limitations.

1.4.1. Layer-by-layer (LBL) method of film deposition

LBL assembly was first described by Decher in the 1990s as an alternative method to LB assembly for the fabrication of thin films^[63]. By this method, PEMs are fabricated by sequential absorption of negatively and positively charged polymers (polyelectrolytes, PE) in an alternating pattern onto a charged substrate. Each monomer unit of a PE possesses a charge, creating a multiply-charged molecule in which electrostatic interactions are possible^[64]. From this, PEs can be sorted into two groups: those with permanent charges in solutions (strong PE) and those whose charge depends strongly on pH (weak PE)^[64]. The charge density—based on the number of groups composing the repeating monomer unit—will also influence the interactions possible between

PEs^[65]. The nature of the PEs (i.e. charge density, molecular weight, weak versus strong) will strongly influence the characteristics and behavior of the resulting film. Without the restrictions imposed by LB assembly, LBL films have been composed to an incredible variety of materials including synthetic polymers^[66,67], nanoparticles^[68], carbon nanotubes^[69], sugars^[70], nucleic acids^[71], proteins^[72], and virus particles^[73]. The LBL method is very simple (Figure 1-4). A charged substrate is exposed to a PE solution where it will deposit on the substrate surface until saturated, reversing the surface charge. The film is then rinsed in an appropriate solution (i.e. water or salt solution) to prevent contamination of other solutions by excess and weakly held PE chains. The second PE (oppositely charged) is then deposited on the film surface to complete the bilayer. This cycle can be repeated until the desired number of bilayers is achieved. While solution-dipping (as shown in Figure 1-4) is the most common method of substrate coating, spray and spin-coating are employed for LBL assembly as well^[64].

LBL films are mainly held together by electrostatic interactions. Charges within the film are neutralized intrinsically or extrinsically (Figure 1-5)^[64]. Intrinsic charge compensation refers to the pairing of charges between the PEs, while charges neutralized by extrinsic compensation are paired with a counter-ion from the surrounding solution. Fixed charges are charges within the film that cannot be paired with a charge from another PE due to imposed constraints from the film structure (i.e. sterics)—these rely on neutralization through extrinsic compensation^[74]. Other interactions (although less common) can also drive PEM

formation including hydrogen bonding^[75], coordination chemistry^[76], and hydrophobic interactions^[77].

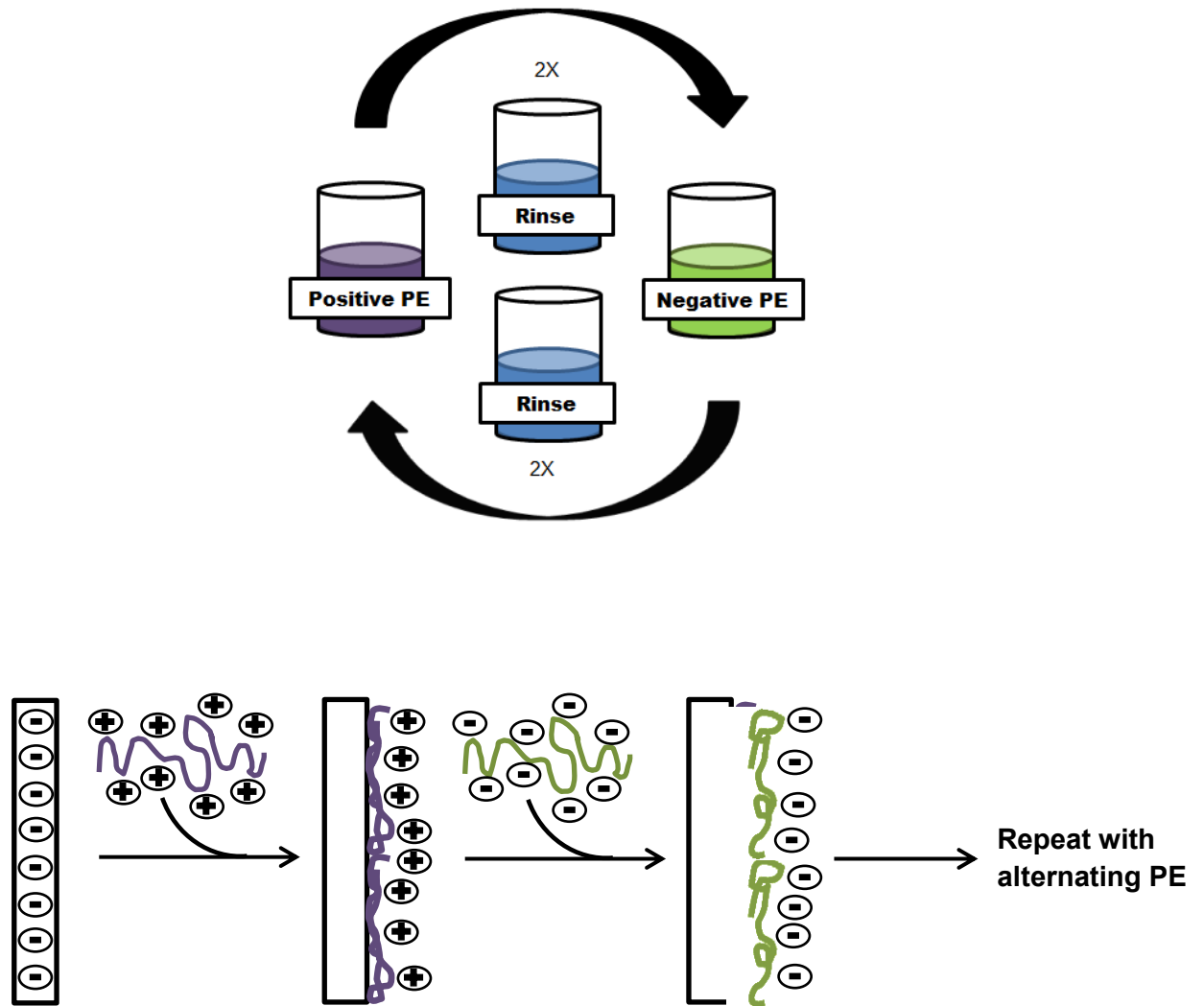


Figure 1-4: Schematic of the layer-by-layer assembly method for polyelectrolyte multilayers. A charged substrate (i.e. quartz) is dipped in a polyelectrolyte of opposite charge (purple) where it adheres through electrostatic attraction, effectively reversing the surface charge. The film is rinsed with an appropriate solution to remove excess polyelectrolyte before dipping in the negatively charged polyelectrolyte (green). The negative polyelectrolyte adheres and the surface charge is again reversed. This process is repeated until a film of the desired number of multilayers is achieved.

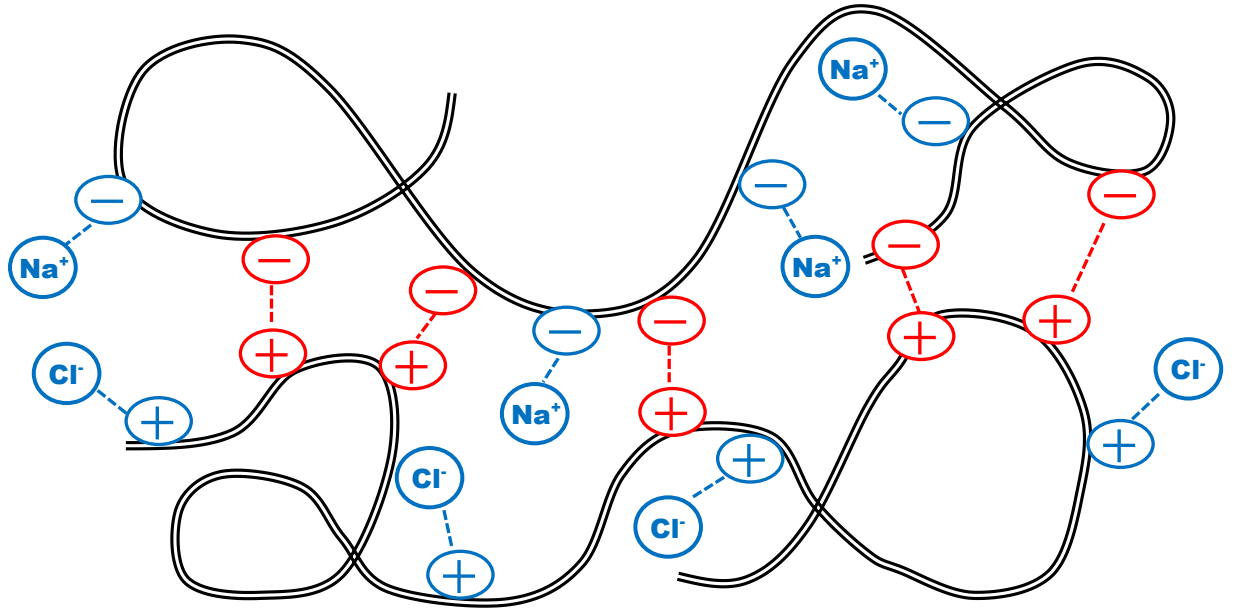


Figure 1-5: Schematic showing charge compensation within a polyelectrolyte bilayer (black). Charges can be paired intrinsically between charged groups on the polyelectrolytes (red). Charged groups unable to participate in intrinsic pairing can be neutralized extrinsically by ions from the surrounding solution—in this case Na^+ and Cl^- (blue). Both are important for the stability of PEMs.

1.4.2. Linear versus Exponential Film Growth Mechanisms

The earliest models of PEM growth show linearly growing systems where the increase in mass and film thickness is proportional to the number of deposited bilayers (deposition steps). Indeed, there are many examples of linearly growing films involving synthetic and natural PE including poly(sodium styrene sulfonate) (PSS)/ poly(allyamine hydrochloride) (PAH)^[66] and CHI/cellulose nanowhiskers^[78] films. In these films, each bilayer interacts only with bilayers that directly neighbor it (above or below) with very little interpenetration and as a result, a distinct layered morphology is seen within the film^[79,74]. However, more recent studies—such as those done by Picart *et al*

using poly(L-lysine) and HA, and Elbert *et al* using poly(L-lysine) and polyethylimine—demonstrated film systems that did not adhere to this growth mechanism^[80,81]. Rather, these systems showed exponential increases in film thickness with each deposition cycle. After the deposition of 20 bilayers, exponential film thickness measured 10 μ m or more as compared to linearly growing films whose typical thickness is approximately 100nm with the same number of bilayers^[79]. This type of growth was attributed to a diffusion model where at least one PE is able to move in and out of the film during buildup (Figure 1-6). Take CHI/HA films for example. When a film is brought into contact with a diffusible PE (CHI), the next bilayer in the film forms on the surface as seen in linearly growing systems but in addition to this, extra CHI (referred to as free CHI) also diffuses into the existing film. The extent of diffusion—number of molecules, penetration depth, and equilibrium behavior— in exponentially growing film systems not yet understood and likely varies depending on the film and deposition conditions. Porcel *et al* speculate the depth a diffusible PE can permeate is finite^[82]. After the deposition of many layers, exponentially growing films often revert to a linear growth mechanism. This is speculated to be due to a “restructuring zone” in which diffusion is hindered due to densification of the internal layers. However, this theory only held true for large molecular weight PEs despite the fact that the exponential-to-linear transition occurs at the same film thickness regardless of molecular weight. Lavallo *et al* believe that PE will continue to diffuse into the film (assuming time is not a factor) until the chemical potential of the film is equal to that of the surrounding solution or until the energy

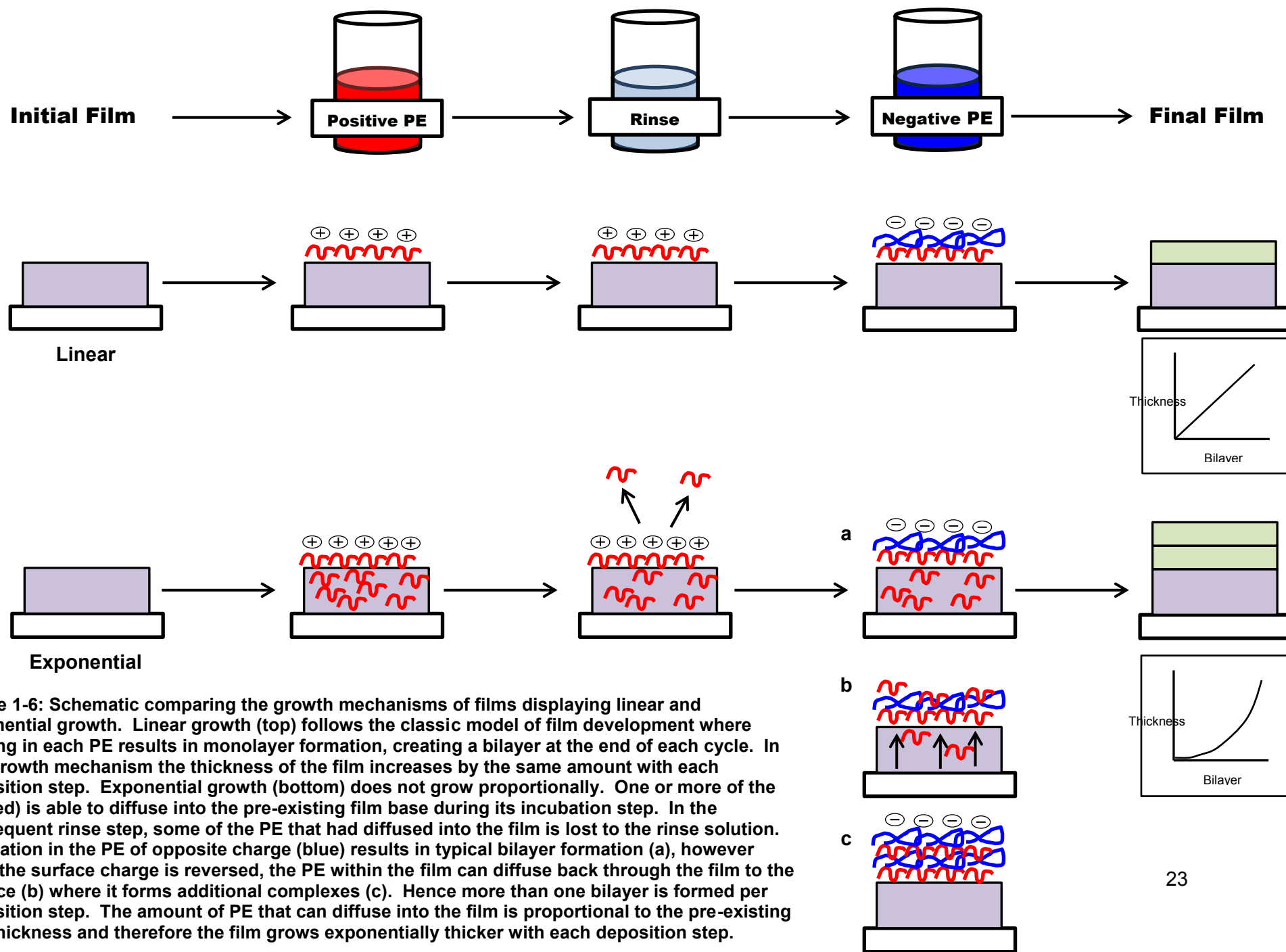


Figure 1-6: Schematic comparing the growth mechanisms of films displaying linear and exponential growth. Linear growth (top) follows the classic model of film development where dipping in each PE results in monolayer formation, creating a bilayer at the end of each cycle. In this growth mechanism the thickness of the film increases by the same amount with each deposition step. Exponential growth (bottom) does not grow proportionally. One or more of the PE (red) is able to diffuse into the pre-existing film base during its incubation step. In the subsequent rinse step, some of the PE that had diffused into the film is lost to the rinse solution. Incubation in the PE of opposite charge (blue) results in typical bilayer formation (a), however once the surface charge is reversed, the PE within the film can diffuse back through the film to the surface (b) where it forms additional complexes (c). Hence more than one bilayer is formed per deposition step. The amount of PE that can diffuse into the film is proportional to the pre-existing film thickness and therefore the film grows exponentially thicker with each deposition step.

barrier required for passage into the film becomes too high^[74]. Until additional studies are able to shed light, the general consensus agrees that some amount will diffuse into the film. As the film is moved into the rinse solution, excess CHI and poorly adhered complexes will be washed from the surface. Some free CHI will be lost from the film as well; however this is limited due to electrostatic barriers^[74]. CHI is positively charged and the surface of the film will also be positively charged. In addition to this, with each CHI lost from the film, the surrounding solution becomes increasingly positive as well creating an increasingly larger energy barrier to overcome in order to leave the film. When the film comes in contact with the negative PE (HA), it complexes to the surface of the film and the electrostatic barriers cease to exist^[74]. The free CHI is able to diffuse out of the film and complex other HA molecules causing the formation of multiple new bilayers. Although intrinsic compensation plays a large role, exponentially growing films rely heavily on extrinsic compensation to allow diffusion through the film^[64].

As a result, exponential films tend to be thicker, with more loosely associated networks of PE^[74]. However, linear and exponentially growing films are quite related to each other. The experimental conditions (i.e. temperature, pH, ionic concentration) in which a film is constructed play a large role in the resulting interaction strength between the PEs involved, and in turn influence the growth mechanism, density, and strength of a given film^[64]. These parameters are just as important as the nature of the PEs themselves (i.e. weak versus strong, molecular mass, 2° interactions) for determining film behavior. Linearly

growing films tend to favor highly charged PE and low ionic strength conditions where intrinsic charge compensation are dominant, forming dense film structures^[64,74]. However, if the ionic strength is increased, the growth mechanism can be changed to exhibit exponential behavior. This was seen in PSS/PAH films when constructed in 1M NaCl compared to 0.15M NaCl which grew linearly^[82,83]. In general, the thickness and roughness of a film increases with higher concentrations of salt as a result of increased charge screening^[64]. The salt ions cause an increase in extrinsic charge compensation; outcompeting PE-PE interactions along the length of the molecules and also screening like-charged groups, decreasing repulsion within the film. This enables structures like coils and loops to form but also increases swelling within the film^[64]. It also allows for diffusion of PE chains within the film and is attributed to the shift from linear to exponential growth. It is true in reverse as well; exponential growth can be reverted to linear growth by decreasing the ionic strength. This was true of CHI/HA films deposited in 10^{-4} M NaCl which grew exponentially at concentrations of 0.15M NaCl^[79]. However, naturally exponential films tend to be unstable at low ionic strengths and there are structural repercussions to deposition under these conditions. For example, CHI/HA films deposited in 10^{-4} M NaCl cannot form continuous films and remain as islets^[79]. CHI and sodium cellulose sulfate films showed reduced growth when the ionic strength was decreased by half from 1M NaCl^[84].

In films composed of one or more weak PEs, pH plays a large role in film formation and morphology. By changing the pH, the charge density of a given

weak PE can be changed depending on the pK_a ^[64]. This in turn affects the thickness of a growing film, the amount of growth per deposition step, and also the thickness and stability of pre-formed films (environmental pH change). The thickness of poly(acrylic acid) (PAA)/poly(allylamine hydrochloride)(PAH) bilayers (both weak PE) changes depending on pH and can range between $>120\text{\AA}$ to $<10\text{\AA}$ depending on the charge density of the PE^[67]. When the pH of the PAA and PAH solutions were 7.5 and 3.5 respectively, the films failed to grow entirely. These experiments were expanded upon by Bieker *et al* who demonstrated that the fluctuations in film thickness also correspond to changes in growth mechanisms^[85]. Intermediate pH (6.5-7.5), where both PE were highly charged, resulted in thin, rigid films growing linearly. As the pH was moved away from this (4.5-6.0 or 8-10) the charge density between the PEs becomes mismatched and the resulting films were soft with an exponential growth mechanism. As this is continued (pH 3-4.5 or 10-12) the charge mismatch becomes extreme resulting in soft films that grow linearly but asymmetrically (increased deposition of a poorly charged PE to neutralize a highly charged PE partner). Morphological changes induced by pH are not always a disadvantage. This property is often exploited in many controlled delivery systems which either exhibit a change in permeability or disassemble to deliver their payload with extreme changes in the pH of the environment^[86].

Increases in temperature can alter the growth mechanisms seen in a given film. Heat provides the energy to overcome electrostatic energy barriers imposed by neighboring PE allowing for internal restructuring and increased

diffusion^[64]. Depending on the amount of heat applied and the film system involved, a change in growth mechanism can be observed. PSS/PDDA films grow linearly at 15 and 25°C and transition to exponential growth as they are heated to 55°C^[87]. This effect is not restricted to large changes in temperature. Increasing the temperature by 1°C from room temperature resulted in a ~5% mass increase for a 30 bilayer PSS/PDDA film^[87].

With the knowledge base of LBL film characteristics expanding, the traditional model of film growth is beginning to evolve. It has been suggested that linear growth is just a special case of exponential growth where diffusion does not happen, or is so slow that PE does not permeate the film^[74,87]. Ghostine *et al* considers the term “exponential” to be incorrect entirely, and rather “linear” and “nonlinear” growth to be more accurate^[88]. They also hypothesize that the bilayer model of growth should be revised as growth during a deposition step occurs as a thickness rather than bilayers. The growth mechanism seen depends on whether the change in thickness is constant in the time given during each deposition step. The concept behind LBL films may grow into something more complex in the coming years. However, until further clarification is present, the studies presented in this work will be discussed in terms of the traditional bilayer model.

1.5. Thesis Objective

This thesis aims to determine whether aptamer technology can be expanded to other film systems. For aptamer-functionalized films to be successful in real-world applications the aptamer must (A) be able to function within the film matrix with high affinity and selectivity and (B) be resistant to environmental challenges (i.e. nucleases). To explore this, the sulforhodamine B aptamer (SA) will be integrated into biocompatible films made of chitosan (CHI) and hyaluronan (HA) polysaccharides. These novel films will be evaluated for continuing high-affinity interactions between the embedded aptamer and its target sulforhodamine B (SB) dye (Chapter 2). It will also be determined whether the chosen film matrix can provide some measure of protection against nuclease-mediated degradation (Chapter 3).

Chapter 2. Preparation of aptamer-containing multilayer films

2.1. Introduction

2.1.1. Aptamer-functionalized multilayer films

Aptamers are very compatible with nanomaterials and have been used to grant the advantages of their binding properties to materials in many applications including hydrogels^[89], nanoparticles^[90], liposomes^[91], micelles^[92], and carbon nanotubes^[93] mainly for the purpose of controlled delivery, sensing, and therapeutics but also to create dynamic materials that are responsive to the surrounding environment. Surprisingly, limited work has been performed using aptamers in films and only two reports exist which are the proof-of-concept for the studies discussed in this work. There are inherent challenges to integrating aptamers into a confined film matrix. The matrix must not interfere with aptamer folding and the final conformation must be correct in order to retain the binding properties of the aptamer. The target must also be able to permeate the matrix to access the aptamer. Both of these challenges were overcome by Sultan *et al* who functionalized PSS/PDDA (PDDA: poly(diallyldimethylammonium chloride)) films and PSS/PAH microcapsules using the sulforhodamine B aptamer (SA)^[36,37]. Sequestering SA within a PSS/PDDA film only had a modest effect on the aptamer K_d (0.7 μ M to 16 μ M) and aptamer films bound the target dye much more effectively than films prepared with other DNAs^[36]. In a slightly different system, the flux of small molecules across PSS/PAH/SA microcapsule walls could

be altered by aptamer-target interaction^[37]. Both studies demonstrate the value of LBL aptamer film systems.

PSS/PDDA and PSS/PAH are excellent model systems for the study of novel nanomaterial applications however they fall short of the biocompatibility standards that are demanded of nanomaterials for practical applications. More recently, focus has shifted away from these synthetic systems and more towards natural polymer films which offer a promising new set of properties including biodegradability, biocompatibility, and lack of toxicity. Materials such as polysaccharides^[79], polynucleotides^[71], enzymes^[94], polypeptides^[82], and proteins^[95] have been used to create novel films with different properties and functionalities. One such film system using CHI and HA was chosen for the present work due to its well-characterized properties and the strong literature base available.

2.1.2. CHI/HA films

CHI is produced by the partial or complete deacetylation of chitin by heat and alkaline treatment^[96]. As the second most abundant polysaccharide (with cellulose being the first), chitin is harvested from the shells of crustaceans with the primary commercial sources coming from crabs and shrimp^[96]. In 2007, several million tonnes of seafood crustaceans were consumed by the global market, 50% of which was discarded as chitin-containing waste^[97]. Aside from this, chitin is also found in the exoskeletons of insects and is produced by some unicellular organisms^[79]. During the deacetylation process, CHI is formed when

50% of the chitin monomer units (N-acetyl- β -D-glucosamine) have been deacetylated^[96]. Therefore, CHI is composed of a random mixture of (1 \rightarrow 4) linked N-acetyl- β -D-glucosamine and β -D-glucosamine monomer units (See Figure 2-1)^[79]. As one of the lower cost choices compared to other biomaterials, it is popular in both research and industrial applications. CHI is used extensively in cosmetics and hair products^[96] but also has applications in agriculture^[98], wastewater treatment^[99], food industry^[100], and biopharmaceuticals^[96].

Hyaluronan (HA) is a stiff, linear polymer composed of N-acetyl- β -glucosamine and β -D-glucuronic acid monomer which are linked together (1 \rightarrow 3) and (1 \rightarrow 4), respectively^[101,102,103]. HA is primarily in vertebrates and is involved in a large number of biological roles including water transport, tissue hydration and joint lubrication, and various mechanical functions in connective tissues^[101,104]. It is also implicated in several co-regulatory functions such as embryonic development, healing, inflammation responses, and tumor development^[104]. Industrially, HA can be isolated from various tissues (e.g. rooster combs) or produced using microorganisms^[103]. There is a large market for HA in cosmetics, however the majority of applications are for clinical work. Clinical applications for HA are extensive and can be classified into five main categories: viscosurgery (to protect delicate tissues and create space during surgeries), viscoaugmentation (aiding to fill and supplement the spaces between tissues), viscoseparation (as a preventative measure against scarring and

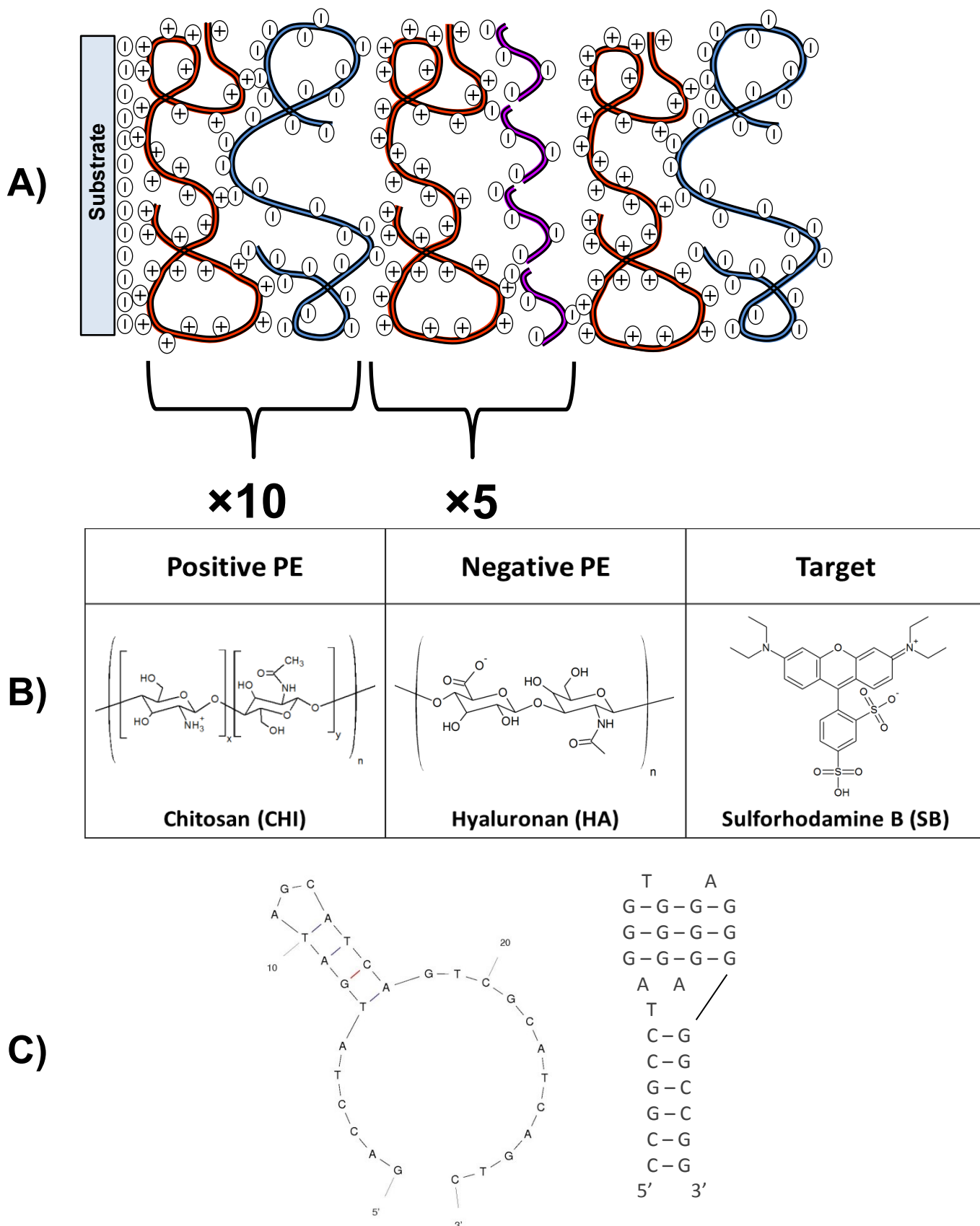


Figure 2-1: Overview of multilayer film composition. A) Schematic of optimized CHI/HA/DNA film. Ten bilayers of CHI (red) and HA (blue) compose the base of the film. Five bilayers composed of CHI and DNA (pink) compose the DNA layers of the film. DNA can represent the incorporation of the SA aptamer or the 29-nt RO. The film then topped with a single bilayer of CHI and HA (capping layer). B) Monomer structures of the PEs used in the film and structure of the target dye SB. C) Sequences of RO (left) and SA (right). Sequences are shown in their predicted secondary structures: a hairpin-loop (RO) (computed by Mfold) and a g-quadruplex (SA) (Adapted from [15]).

adhesion of connective tissues as a result of surgery trauma), viscosupplementation (to relieve pain associated with fluid loss such as with arthritis), and viscoprotection (to promote healing of tissues and protect them from drying and infection)^[103].

Together, CHI/HA nanomaterials have been at the forefront of novel applications due to their advantageous characteristics. Different applications include anti-adhesive and anti-bacterial coatings^[79,105], scaffolds for tissue engineering^[106], and controlled release systems^[107]. The properties of CHI/HA LBL films systems have been characterized extensively in respect to growth mechanism, growth rate, and film behavior^[70,79,101,108]. The unique properties, robust nature, and biocompatibility of CHI/HA films offer a strong platform for a biodegradable aptamer-functionalized film system using LBL chemistry.

2.1.3. Chapter Objectives

The proof of concept work integrating aptamers and LBL films was successful; however a more biocompatible system is required for practical applications in the field. A new film model based on CHI and HA has been chosen to replace PSS and PAH. The behavior of polysaccharide films is quite different than synthetic systems with a new set of challenges and therefore the ability of an aptamer to function within this matrix must be confirmed. This chapter describes the integration of the SB aptamer into CHI/HA films and the effects on its binding abilities as well as optimization of the CHI/HA film system.

The SB aptamer was chosen as it folds into a highly structured G-quadruplex conformation making it a good candidate to study the effects of a film matrix on aptamer function^[15]. In addition to this, the optical characteristics of SB dye are advantageous as this species both fluoresces and absorbs strongly in the visible range.

2.2. Experimental

2.2.1. Materials

Glass (76 x 25mm) and quartz (50 x 25mm) microscope slides were purchased from VWR. Gridded glass slides (75 x 25mm, 1mm thick) were purchased from Lab Scientific. A silicon wafer was donated by Professor Gary Tarr from the Department of Electronics at Carleton University. All slides were cut into smaller slides (~1.5 x 2.5mm) using a hand-held diamond-tipped tool with exception to the grid slides which only had the excess glass surrounding the printed grid removed.

HA (MW 1,580,000 Da) was purchased from Acros Organics as sodium hyaluronate. CHI (MW 135,000 Da) was purchased from Acros Organics. Sulforhodamine B (SB) dye was purchased from Sigma Aldrich. Phosphoramidites, modifiers, acetonitrile, deblock, activator, oxidizer, and capping reagents for DNA synthesis were purchased from Glen Research. Columns (standard, 500Å pore size) were purchased from BioAutomation. All purchased reagents were used as received.

All buffers were made with Milli-Q water and filtered with Corning 0.22 μ m cellulose acetate filter units. Buffer pH adjustments were made with diluted acetic acid. Glassware was rinsed five times with distilled and five times with deionized water prior to use. Deionized water was used for all experiments unless otherwise stated.

2.2.2. Preparation of the aptamer and random DNA sequences

The sulforhodamine B aptamer (SA sequence: 5'–CCG GCC TAG GGT GGG AGG GAG GGG GCC GG–3') and a random oligomer of the same length (RO sequence: 5'–GAC CTA TGA TAG CAT CAG TCG CAT CAG TC–3') were synthesized using standard phosphoramidite chemistry on a BioAutomation Mermade 6 DNA synthesizer as specified by the manufacturer. Modified SA and RO DNA was also prepared by adding fluorescein (as 6-FAM) to the 5' end of the sequence.

Post synthesis, the columns were removed from the synthesizer and the column beads were dried under a stream of argon before transfer to microcentrifuge tubes. The DNA was cleaved from the beads by incubating at 55°C in 1mL of NH₄OH (28%) for 16-24 hours. The supernatant was partitioned away from the beads by concentrating the beads using centrifugation and drawing off the liquid by pipette. The beads were rinsed with several milliliters of water using the same method, and the collected supernatant was dried down overnight using the cryopump setting on a Savant AES2010 SpeedVac.

The synthesized DNA was purified by denaturing polyacrylamide gel electrophoresis (PAGE) using a protocol adapted from the Molecular Cloning Laboratory Manual^[109]. A 12% PAGE gel solution was made using 31.5g of urea, 23.5mL of acrylamide stock (Bioshop; 40% solution (w/v), 19:1 acrylamide/bis-acrylamide), 14mL of water, and 15mL of 5X TBE buffer (45mM Tris-HCl, 45mM boric acid, 1mM ethylenediaminetetraacetic acid (EDTA), pH 8.3). After heating the solution to 37°C to dissolve the urea, it was filtered with filter paper (Whatman No. 1), and allowed to cool to room temperature. The gel was cast between two glass plates after the addition of 450µL of 10% ammonium persulphate and 35µL of N,N,N',N'-tetramethylethylenediamine (TEMED), and allowed to polymerize for 30 minutes. A one well comb was used. The polymerized gel was pre-equilibrated in a SE 600 Chroma Standard Dual cooled gel electrophoresis unit at 300V for 10 minutes. The DNA samples were re-suspended in a minimum volume of a 1:1 mixture of water to formamide, and heated at 55°C for at least 10 minutes before loading in the gel. To track DNA movement through the gel, a fluorescein-labeled ssDNA marker (18 nucleotides, 20µM) was loaded in addition to the sample. The gel was run at 300V until the 18-nt marker had migrated approximately $\frac{3}{4}$ of the way down the gel. The gel was imaged on a 20 X 20 cm TLC plate (F₂₅₄) using an Alpha Imager Multi Image Light Cabinet (Alpha Innotech) on the epi-UV setting ($\lambda_{\text{excitation}} = 254\text{nm}$). The DNA bands of appropriate size were cut from the gel. The gel pieces were crushed in a 50mL falcon tube and eluted with 50mL of water overnight at 37°C with shaking. The gel pieces were separated from the surrounding liquid using a 0.22µm cellulose

acetate syringe filter and dried down using a lyophilizer (Labconco Freezone^{4,5}). The purified DNA was desalted using Amicon-Ultra centrifuge units (3kDa cut off) and quantified by UV-visible (UV-Vis) spectrophotometry using a Varian Cary 300 Bio UV-Vis spectrometer.

2.2.3. Film deposition

Substrates (glass, quartz, or silicon slides) were cleaned by incubating the slides in a 1:1:5 solution of H₂O₂:NH₄OH:H₂O at 70-90°C for ten minutes, followed by copious rinsing with water. Substrates were immediately used for film deposition.

CHI/HA films

Film solutions were prepared at 1mg/mL in 0.15M NaCl pH 4.5 unless otherwise stated. HA was mixed vigorously on a shaker to disperse the polymer in solution. With a pKa of ≈ 2.9 ^[108], HA is negatively charged at acidic pH. CHI has a pKa of ≈ 6 ^[108] and therefore requires an acidic environment to become positively charged and also to dissolve in aqueous solution. Initially, CHI was titrated with concentrated glacial acetic acid to dissolve the polymer, however, accidental over-acidification proved to disrupt CHI/HA film formation (results not shown). Therefore, the pH of CHI solutions were adjusted specifically to 4.5 using diluted glacial acetic acid.

Cleaned slides were dipped successively in the CHI and HA (10mL) solutions for 15 minutes each, with two rinses ($R_1= 10s, 10mL$; $R_2= 5s, 10mL$) in 0.15M NaCl pH 4.5 between solutions. For films containing DNA (6-FAM or unmodified), the anionic PE was switched with $2 \times 10^{-6}M$ solution of SA or RO in water or 0.15M NaCl pH 4.5. DNA solutions were heated for 15 minutes at 80-90°C to denature the DNA, and then cooled immediately on ice for at least 30 minutes before use. This deposition protocol was repeated to create films with the following schematics (where the number specifies the number of bilayers); 10 CHI/HA (CHI/HA films), 10 CHI/HA-5 CHI/SA-1 CHI/HA (CHI/HA/SA films), and 10 CHI/HA-5 CHI/RO-1 CHI/HA (CHI/HA/RO films). Figure 2-1 shows the composition of the multilayer films and gives structural information regarding the components. CHI, HA, and rinse solutions were refreshed every 10 bilayers. Annealed films were heated for 10 minutes at 70°C in 0.15M NaCl pH 4.5 or 0.10M KCl pH 4.5, and allowed to cool to room temperature prior to dye binding experiments. To assess dye binding, films were dipped in 200 μ M SB dye (in 0.10M KCl) for 30 minutes unless otherwise stated. The films were rinsed with water until the washings were no longer pink. Films were allowed to dry overnight before analysis.

Preparation of films and dye binding experiments for UV-Vis analysis was conducted by the above procedure (designated as the “original” protocol) however some alternative conditions were also investigated. In general, PE solutions were prepared at 1mg/mL; however 2mg/mL solutions were also used for some UV-Vis experiments. Growth mechanism and dye binding experiments

were also performed for films prepared by an alternative deposition method (designated as the “modified” protocol) whose rinse procedure varied from the original protocol. Rinses were longer ($R_1 = 1$ min, $R_2 = 5$ min) with varying volumes ($R_1 = 10$ mL, $R_2 = 12$ mL) which were changed every 4 uses. CHI and HA solutions were never changed. All other conditions remained the same. In addition to this, UV-Vis growth experiments were conducted for three other variations on the modified protocol; the Mulligan, the fresh-solution (FS), and the Richert adaptations. The Mulligan adaptation involved increasing the rinse solution volumes where $R_1 = 175$ mL and $R_2 = 75$ mL. The FS adaptation was conducted in the exact manner as the modified protocol as outlined above, however the rinse solutions were changed with every use. The Richert adaptation increased the number of rinses and their time and volume where $R_1 = 350$ mL for 1s, $R_2 = 60$ mL for 6min, and $R_3 = 60$ mL for 6 min. All deposition times, conditions, and frequency of solution changes remained the same. In all UV-Vis experiments an additional rinse in water ($R = 10$ mL, 5s or 1 min) to remove excess salt was added after deposition of the layer to be analyzed. Before each spectrum, the films were dried under a stream of argon.

2.2.4. Time of Flight Secondary Ion Mass Spectroscopy

CHI/HA/DNA films were prepared with unmodified DNA by the original method as described in Section 2.2.3, with the exception of one sample set that was constructed with fewer base bilayers (5 CHI/HA-5 CHI/DNA-1 CHI/HA) and

exposed to 2mM SB dye during dye binding experiments. Thicker film (10 CHI/HA – 5 CHI/DNA – 1 CHI/HA) dye binding experiments were performed with 2mM or 200 μ M SB dye. Depth profiles were collected using a ToF-SIMS IV instrument (IonTOF GmnH) at the University of Alberta using a dual ion-beam system to generate negative secondary ions. Bi⁺ ions (operated at 25kV) were used as an analytical source, and Cs⁺ ions (operated at 250V with ion current at 10nA) were used as a sputtering source. The ion beams were alternated to create 500 x 500 μ m² craters in the samples from which an area of 108 x 108 μ m² in the center of the crater was used for ion acquisition. Peak areas were calculated using Microsoft Excel using the composite trapezoidal integration method for determining the area under a curve. Surface images were taken using the same instrument operated at 25kV in a static mode with Bi⁺ ions as the analytical source. Optical images of the film were taken using a digital camera attachment on the same instrument. All profiles were collected on dry films.

2.2.5. Microscopy

Atomic Force Microscopy (AFM)

CHI/HA/DNA films were prepared with unmodified DNA as described in Section 2.2.3, with the exception that dye binding experiments were performed with a SB dye concentration of 2mM. Topography images were taken with a Ntegra AFM (NTMDT, Russia) in tapping mode equipped with a 100 x 100 μ m² scanner (Ntegra) and rotated monolithic Si cantilever tips (Budget Sensors; 125 μ m long, 40 N/m spring constant Tap 300Al, 315 kHz resonance frequency).

A minimum of two areas were sampled from each film. All AFM images were taken at room temperature on dry films.

Scanning Electron Microscopy (SEM)

CHI/HA/DNA films were prepared with unmodified DNA as described in Section 2.2.3, with the exception that CHI/HA film dye binding experiments were performed with a SB dye concentration of 2mM. Images were taken on a Tescan VegaII XMU SEM. All SEM images were taken at room temperature on dry films that had been sputter-coated in a gold/palladium alloy using an Anatech Hummer VII Sputter-Coater. CHI/HA images were taken from the flat surface of glass substrates.

Fluorescent Microscopy (FM)

Annealed and unannealed CHI/HA/DNA films were prepared with unmodified DNA by the original and modified method and incubated with SB dye as described in Section 2.2.3. Additionally, CHI/HA/6-FAM DNA films were prepared as well by both protocols and incubated with SB dye to analyze for binding and co-localization between the DNA and dye. Throughout sample preparation and storage, samples were shielded from all light using aluminum foil coverings to prevent dye bleaching. All FM images were taken at room temperature on dry films. Images investigating dye-DNA co-localization and quantification of target-dye binding were taken with an EVOS®fl fluorescent microscope using AMG software. Fluorescence of 6-FAM DNA and SB dye was

imaged using the GFP channel ($\lambda_{\text{excitation}} = 470\text{nm}$, $\lambda_{\text{emission}} = 525\text{nm}$) and RFP channel ($\lambda_{\text{excitation}} = 531\text{nm}$, $\lambda_{\text{emission}} = 593\text{nm}$) respectively. Films were rinsed after incubation with the dye in 10mL aliquots of deionized water three (original method) or five (modified method) times for 10s. Images of the effect of annealing on dye binding were taken with an Olympus BX61 Fluorescent microscope ($\lambda_{\text{excitation}} = 531\text{nm}$, $\lambda_{\text{emission}} = 594\text{nm}$) connected to a Q-imaging Retiga 2000R camera. Films were rinsed briefly after dye incubation using deionized water. Mean fluorescent intensities of the images were calculated using ImageJ. Statistical significance was analyzed in Excel using a student t-test (heteroscedastic analysis with unequal variance, 95% confidence interval). Magnification was 10X for all images.

2.3. Results and Discussion

2.3.1. Optimization of CHI/HA films and assessment of film morphology

5 CHI/HA bilayer base films

Initial films were modeled after the PSS/PDDA/DNA film schematic that had proved successful in the proof of concept work^[36], using a five bilayer base to achieve thin, nanoscale films. Their composition and target-binding abilities were then to be assessed using ToF-SIMS, however this analysis was met with difficulties. Figure 2-2 shows a sputter profile of a multilayer film composed of

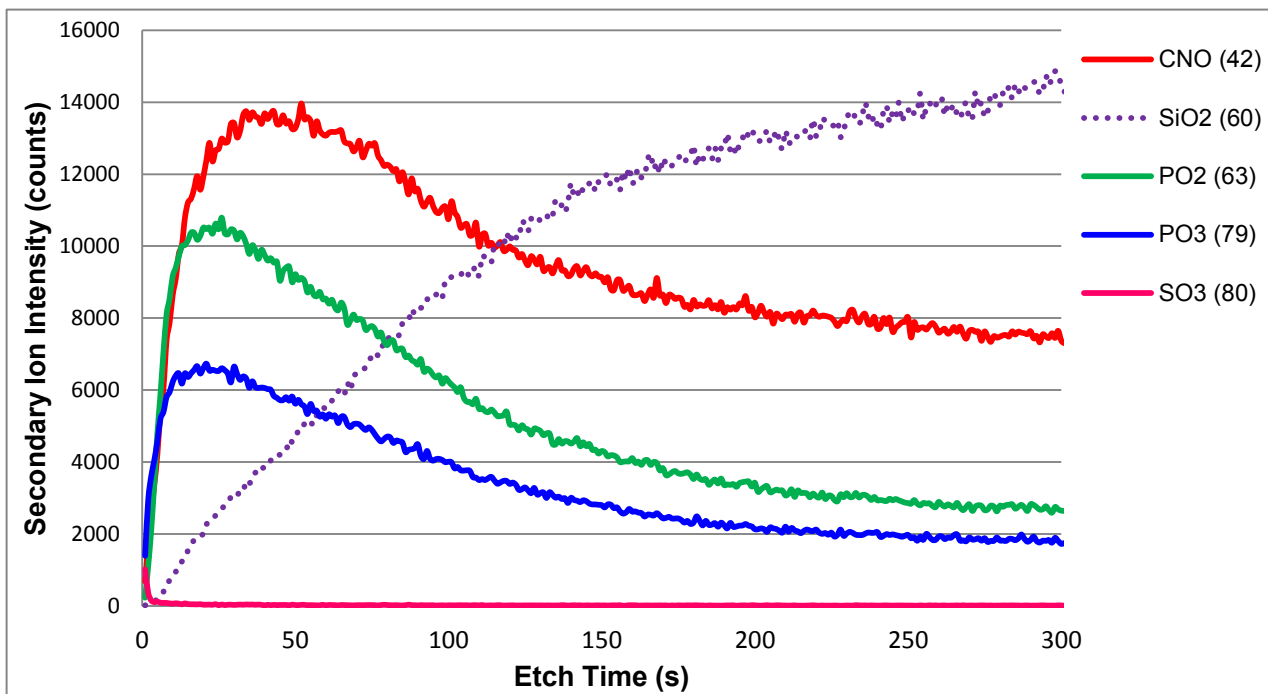


Figure 2-2: Representative ToF-SIMS sputter profile from a sample set of multilayer films with the general composition of 5 CHI/HA – 5 CHI/DNA – 1 CHI/HA. The depth profile shows the characteristic secondary ions with the greatest signal intensities of a film containing SA DNA after exposure to 2mM SB dye. Ion masses (in g/mol) are shown in brackets.

5 CHI/HA – 5 CHI/SA – 1 CHI/HA after exposure to 2mM dye. Clean depth profiles with all species of interest (CNO^- , PO_3^{3-} , and SO_3^{2-}) were difficult to obtain, showed excessive loss of key characteristic secondary ions in favor of smaller species (high intensity PO_2^{3-} peak versus PO_3^{3-}), and was complicated by immediate observation of substrate-specific species (SiO_2^{2-}) with the onset of sputtering. Despite exposure to SB dye, the SO_3^{2-} peak in the sputter profile was virtually non-existent. The same trends were seen with all other films prepared from this sample set including CHI/HA alone, SA and RO films missing the capping layer, and films made with RO DNA with and without SB dye exposure (See Appendix). This was much different than what was seen in the PSS/PAH/DNA proof of concept work where characteristic secondary ions were

present in good yields and the substrate-specific ions were not seen until ~300s into the profile. Figure 2-3 shows an optical image taken of the same multilayer film and corresponding surface images tracking several ion species. From the optical image, it was apparent that films having only five CHI/HA base bilayers were porous. Strong signal intensities for salt ions (Na^+ , Cl^-) and substrate specific species (SiO_2^{2-}) were seen by ToF-SIMS surface imaging adding further evidence towards this theory while film-specific species (PO_2^{3-} , PO_3^{3-} , CHO_2^- , CNO^- , C_2HO^-) were generally seen in lower amounts. The observed pores are most likely a product of the mechanism by which CHI/HA films grow; a process that is well studied in literature. The first bilayers form as small, disconnected islands which continue to grow in diameter and height as more layers are deposited until they converge on one another, forming a continuous film usually after 8-10 bilayers have been deposited^[79,101]. Despite that the film consists of eleven bilayers in total, the addition of CHI/DNA bilayers are not able to transition the film from island to continuous film morphology. Variations in the salt concentration during the deposition of the CHI/DNA layers may have played a role in this morphology as well. While the CHI was always dissolved in 0.15M NaCl, the DNA used to build these films was dissolved in water and water was also used in the subsequent rinsing step. A study of the effects of salt concentration on the growth of CHI/HA films performed by Richert *et al* showed low salt concentrations heavily impede film growth^[79].

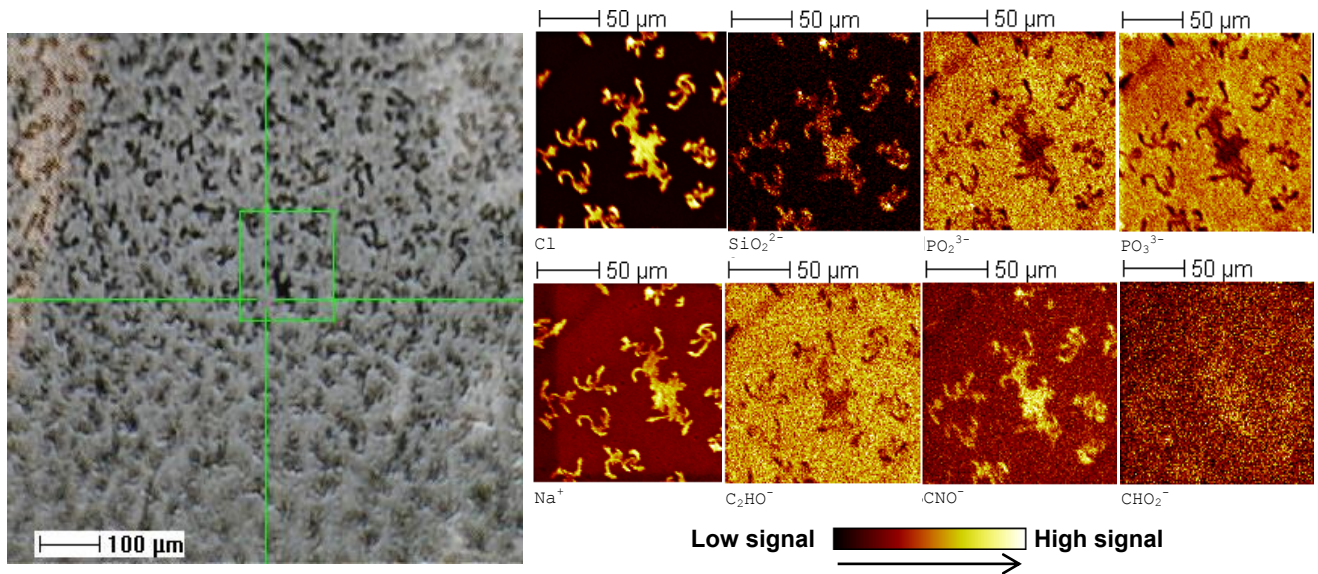


Figure 2-3: Optical image of a multilayer film composed of 5 CHI/HA – 5 CHI/SA – 1 CHI/HA showing the presence of pores within the film (left). The films were subjected to ToF-SIMS surface imaging ($156.2 \times 156.3 \mu\text{m}^2$ area outlined by green box) to determine compositional variations (selected images shown on right). Several characteristic ions were monitored (rounded masses in g/mol given in brackets). Polyelectrolyte specific ions include CHO_2^- (45), CNO^- (42), and C_2HO^- (41). DNA specific ions include PO_2^{3-} (63), and PO_3^{3-} (79). Salt specific ions include Na^+ (23), and Cl^- (35.5), and substrate specific ions include SiO_2^{2-} (60).

When salt (NaCl) concentrations were at 10^{-4}M , polyelectrolyte deposition was severely decreased and film growth ceased to be exponential but instead adopted a linear growth mechanism even if the films were previously built at higher salt concentration with exponential growth. In addition to this, the films were unable to transition to a continuous morphology and remained as islands even after the deposition of fifty bilayers. Using DNA in water may have prevented the film from becoming continuous after the deposition of ten bilayers total by decreasing the population of salt ions within the film during those deposition steps giving it an “intermediate” morphology between islands and continuous film.

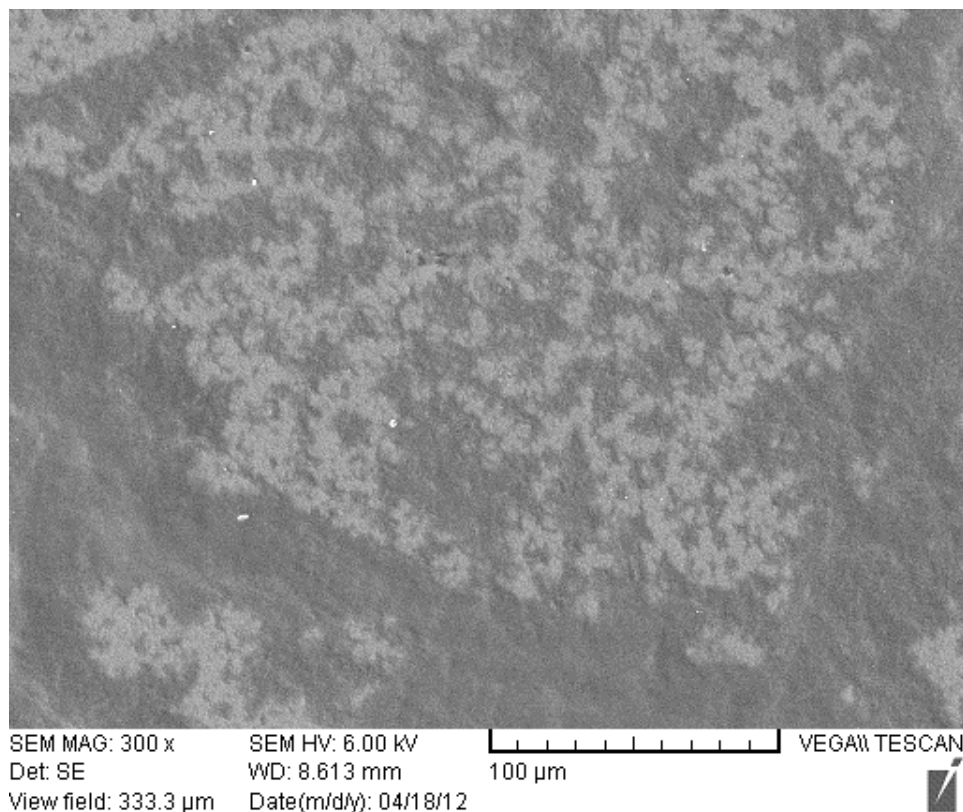


Figure 2-4: Representative SEM image from a sample set of multilayer films with the general composition of 10 CHI/HA – 5 CHI/DNA – 1 CHI/HA. The image shows a continuous film with no pores for a multilayer film made with SA DNA.

10 CHI/HA bilayer base films

To achieve continuous films, five bilayers were added to the CHI/HA base to ensure a complete foundation for the deposition of the CHI/DNA bilayers. Figure 2-4 shows a SEM image confirming the absence of pores due to the addition of five bilayers. Films showed identical morphology and continuity whether using SA or RO DNA, and with or without dye exposure (not shown). This was also consistent with optical microscope images as well as ToF-SIMS analysis of the films (Figure 2-5). Regardless of DNA used or dye exposure, films appeared continuous with the only obvious morphology variations being

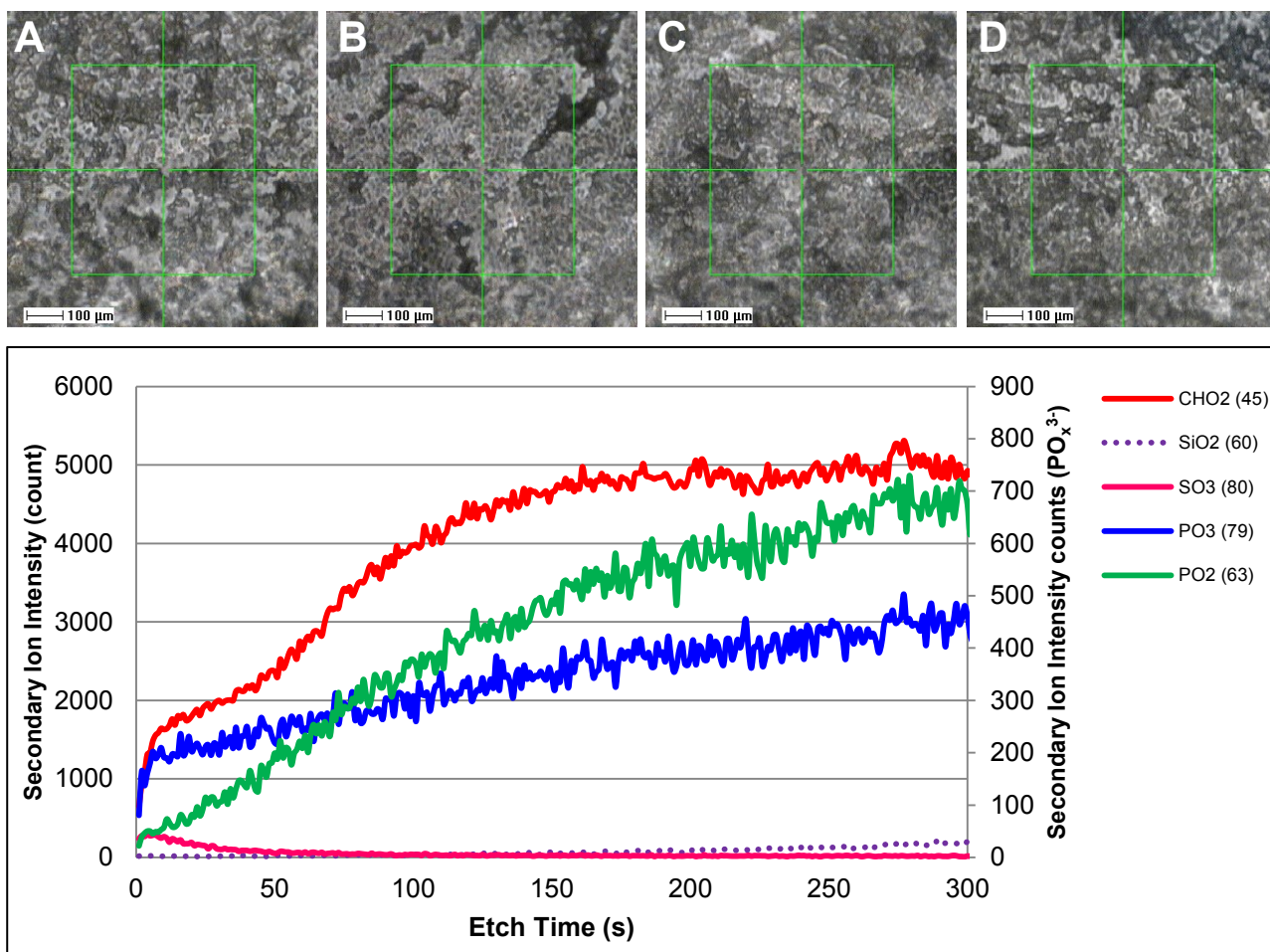


Figure 2-5: Analysis of CHI/HA/DNA films after a 5 bilayer increase to the base CHI/HA layers. Top: Optical images of a multilayer films with the general composition of 10 CHI/HA – 5 CHI/DNA – 1 CHI/HA where A) contains SA DNA, B) contains RO DNA, C) contains SA DNA and was exposed to 2mM SB dye, and D) contains RO DNA and was exposed to 2mM SB dye. In all cases, no pores were seen. Bottom: Representative ToF-SIMS sputter profile from the same sample set of multilayer films. The depth profile shows the characteristic secondary ions with the greatest signal intensities of the film containing SA DNA that had no exposure to the target dye. Ion masses (in g/mol) are shown in brackets. Secondary ion intensity of phosphate species (PO_2^{3-} , PO_3^{3-}) are displayed on the right-hand y-axis. All other species are displayed on the left.

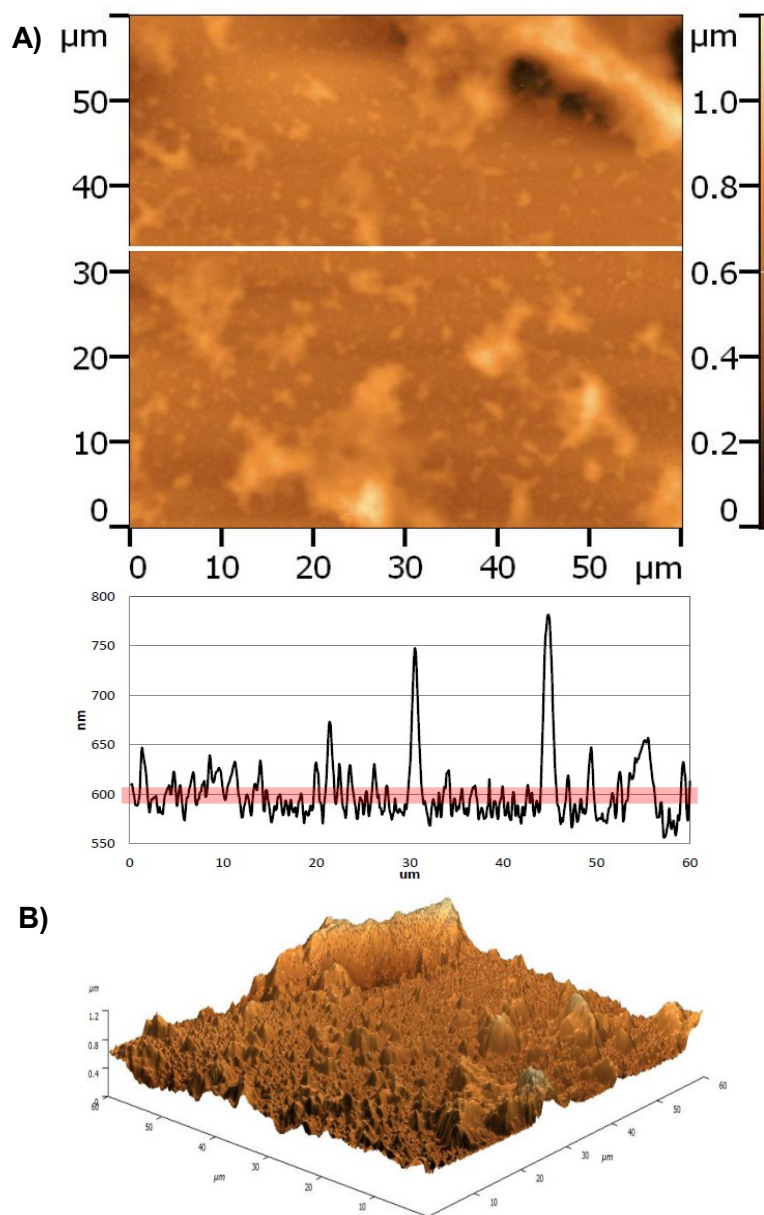


Figure 2-6: Representative AFM image showing surface topography of a 60 x 60 μm² square from a dry CHI/HA/SA film. A) Height profile of selected area (white line) on a 2D image. Area highlighted in red represents the average peak height value showing the large variation in peak height. B) 3D representation showing overall film morphology.

Table 2-1: Film morphology and roughness parameters determined for two 60 x 60 μm^2 AFM images of films containing the SA aptamer or RO control, with or without exposure to SB dye. Two trials (A and B) were taken from different areas on the same film. All values were calculated with NOVA software. AFM images were taken in tapping mode.

| Sample | | Number points sampled | Average height ^a (nm) | Average roughness ^b (nm) | RMS roughness ^c (nm) | Average RMS roughness (nm) |
|---------|---|-----------------------|----------------------------------|-------------------------------------|---------------------------------|----------------------------|
| SA -dye | A | 262144 | 601.9 | 82.3 | 119.4 | 157.1 |
| | B | 262144 | 515.0 | 128.5 | 194.8 | |
| SA +dye | A | 262144 | 640.7 | 157.7 | 193.4 | 198.1 |
| | B | 172032 | 1380.6 | 138.9 | 202.8 | |
| RO -dye | A | 262144 | 460.4 | 113.6 | 143.7 | 185.9 |
| | B | 262144 | 671.7 | 181.0 | 228.1 | |
| RO +dye | A | 262144 | 508.7 | 96.0 | 134.4 | 160.1 |
| | B | 262144 | 679.6 | 134.2 | 185.7 | |

$$^a \bar{z}(N, M) = \frac{1}{N} \sum_{x=1}^N z(x, y)$$

$$^b R_a(N, M) = \frac{1}{N} \sum_{x=1}^N (z(x, y) - \bar{z}(N, M))$$

$$^c R_q(N, M) = \sqrt{\frac{1}{N} \sum_{x=1}^N (z(x, y) - \bar{z}(N, M))^2}$$

trenches whose size and depth are most likely exaggerated due to drying of the films. In addition to this, ToF-SIMS analysis was no longer complicated by early entrance of substrate-specific secondary ions. Therefore, all future films were designed based on this composition (Figure 2-1).

Once continuous films were achieved, AFM was used to investigate the general morphology and roughness. Figure 2-6 shows a surface topography image of a CHI/HA/SA film which is representative of what was seen for all films imaged (not shown), however a summary of morphology properties for all films is shown in Table 2-1. In general, the films appear to be very rough with large microstructures arising from the island-growth mechanism of film growth. These large island peaks vary in width and height. The average height, which describes

the average height of all measurable peaks in a sample^[110], varies considerably not only between films of different composition, but also between trials on the same film. This is also true to a lesser extent for average roughness, which is the average deviation in peak height, and the root-mean-square (RMS) roughness, which is the standard deviation on the surface heights^[110]. The magnitude of these two parameters is indicative of an extremely rough surface, which is in agreement with the 3D image shown in Figure 2-6B. A perfectly smooth surface would, in theory, have a RMS roughness of zero, whereas a smooth film surfaces achieved by LBL assembly such as PSS/PAH and PSS/polyaniline films generally have low RMS roughness values of ~4nm or 25nm respectively^[111,112]. All examples listed were chosen because the RMS roughness was measured for films constructed of ten bilayers. In general, RMS roughness tends to change (increase or decrease) with more bilayers which can cause a smooth film of few bilayers to become rough as it is built thicker or vice versa; therefore this effect must be kept in mind. The value of RMS roughness increases with rougher films as a function of the polyelectrolytes used, and also as a function of deposition conditions (such as temperature, pH, and substrate) and AFM imaging conditions (such as scanning mode and rate)^[113]. Despite this, RMS roughness is still a useful surface parameter and is used quite often in literature to describe CHI/HA films making it an adequate reference point. The average RMS roughness for all films was measured to be between ~150-200nm with very little difference between films of different DNA content and dye exposure (Table 2-1). The rough morphology of the films is consistent with

literature for CHI/HA films. A study by Kujawa *et al* found the RMS roughness to be ~110nm for a hydrated 12 bilayer CHI/HA film made from 360,000Da HA and 160,000Da CHI^[101]. The value measured may have been exaggerated compared to that found by Kujawa *et al* as the films were dried before AFM imaging, making them appear rougher. Hydrated AFM was attempted, however was never successful (Appendix). It is also unclear what affect DNA has on the film roughness. The use of ssDNA in multilayer films is uncommon. Ren *et al* did investigate the morphology of hydrated PLL/dsDNA films and found them to form smooth films with RMS roughness values of 2.70nm at 5 bilayers and 8.21nm at 10 bilayers^[71]. However, even at 10 bilayers the films did not form a continuous morphology but remained as the intermediate vermiculate form. Due to the extreme variations in height and width seen in the peak-like microstructures, the thickness of the films was never measured as it would not truly be accurate. Hydration and swelling also play a large role in the final thickness of a film, with large differences between dry and wet films^[114]. Thickness has been estimated for CHI/HA films by several other groups for hydrated films; 869 ± 202 nm for a 12 bilayer film^[101], and ~300nm for a 10 bilayer film^[79]. These values must not be treated as absolute measurements as PE molecular weight and deposition condition differences affect the resulting film thickness quite considerably.

2.3.2. ToF-SIMS analysis of target binding

Once the base CHI/HA section was increased from five to ten bilayers, PO_3^{3-} became the primary secondary ion monitored for the presence of DNA, however, in some rare cases PO_2^{2-} was still present at high enough levels to be considered. In those cases, the intensities of both phosphate species were added together for a more accurate representation of the overall DNA levels in the film. All samples were prepared by the original method of deposition.

ToF-SIMS depth profiling was used in the proof of concept work with PSS/PDDA/DNA films as a measure of target binding and co-localization of the DNA and dye on a LBL basis^[36]. At first glance, it is apparent that the CHI/HA/DNA films behave quite differently than the proof of concept (See Figure 2-7). The alternation between species as each layer is probed seen in the proof of concept sputter profiles, was not seen in the ToF-SIMS analysis of these films (Figure 2-8). This is most likely due to the gel-like morphology seen in exponentially growing films systems^[115]. Linearly growing systems have highly defined layers that only interact directly with layers above and below it^[116,117]. With the diffusion of one or more of the PE species, exponentially growing films have less structure, higher entanglement and therefore more contact with multiple layers in the film^[115,117,118]. In addition to this, due to the roughness and large microstructures in these films (as discussed in Section 2.3.1), ToF-SIMS may be analyzing different segments of the film make up, depending on the region selected. Despite this, all species relevant to analysis were still detected

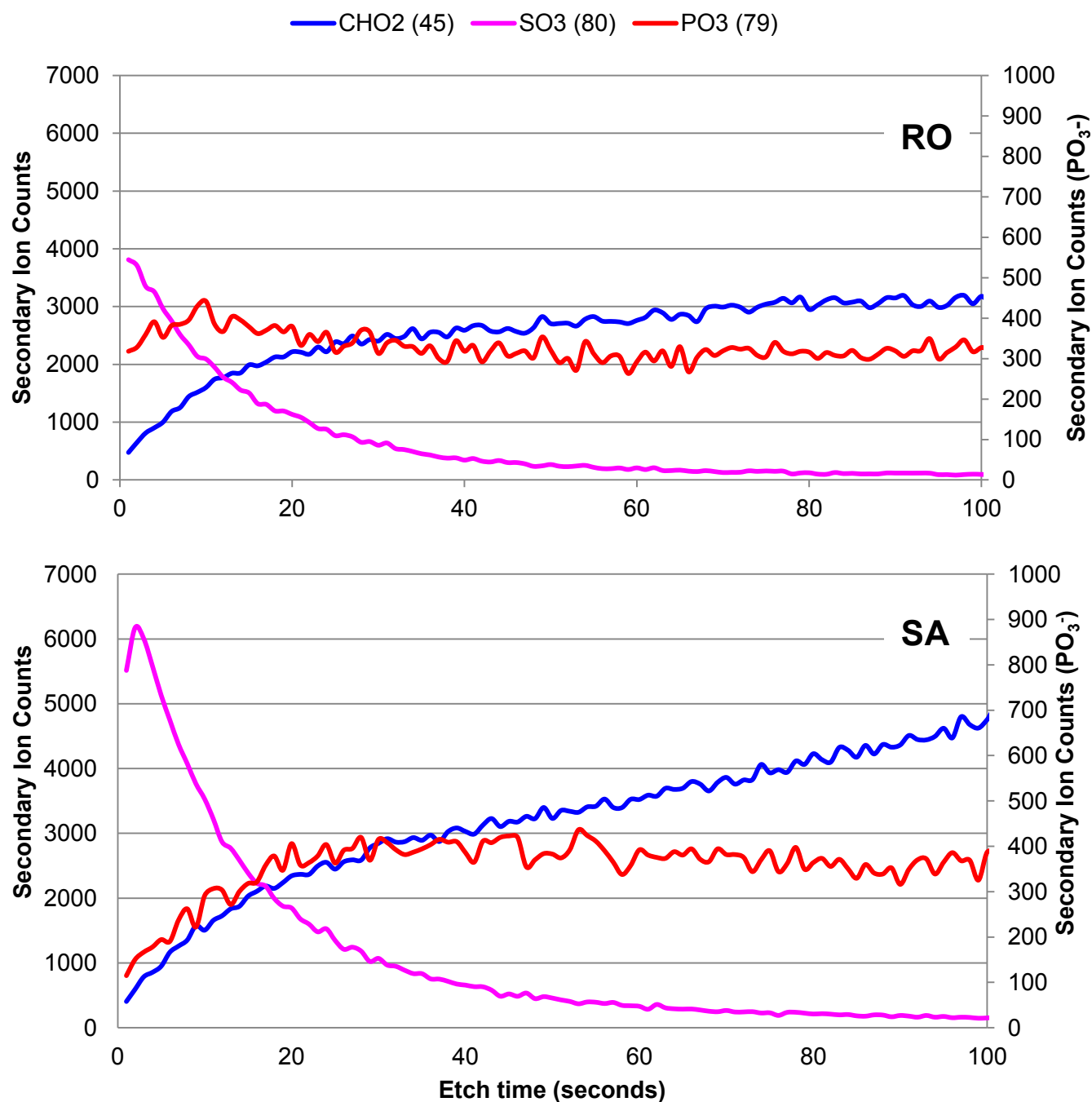


Figure 2-7: ToF-SIMS sputter profiles of CHI/HA/RO (top) and CHI/HA/SA (bottom) films exposed to 2mM SB dye. The depth profiles shows the characteristic secondary ions generated from each species of interest: CHO₂⁻ from the CHI/HA matrix, PO₃³⁻ from DNA, and SO₃²⁻ from the SB dye. Ion masses (in g/mol) and shown in brackets. Secondary ion intensity of phosphate species (PO₃³⁻) are displayed on the right-hand y-axis. All other species are displayed on the left.

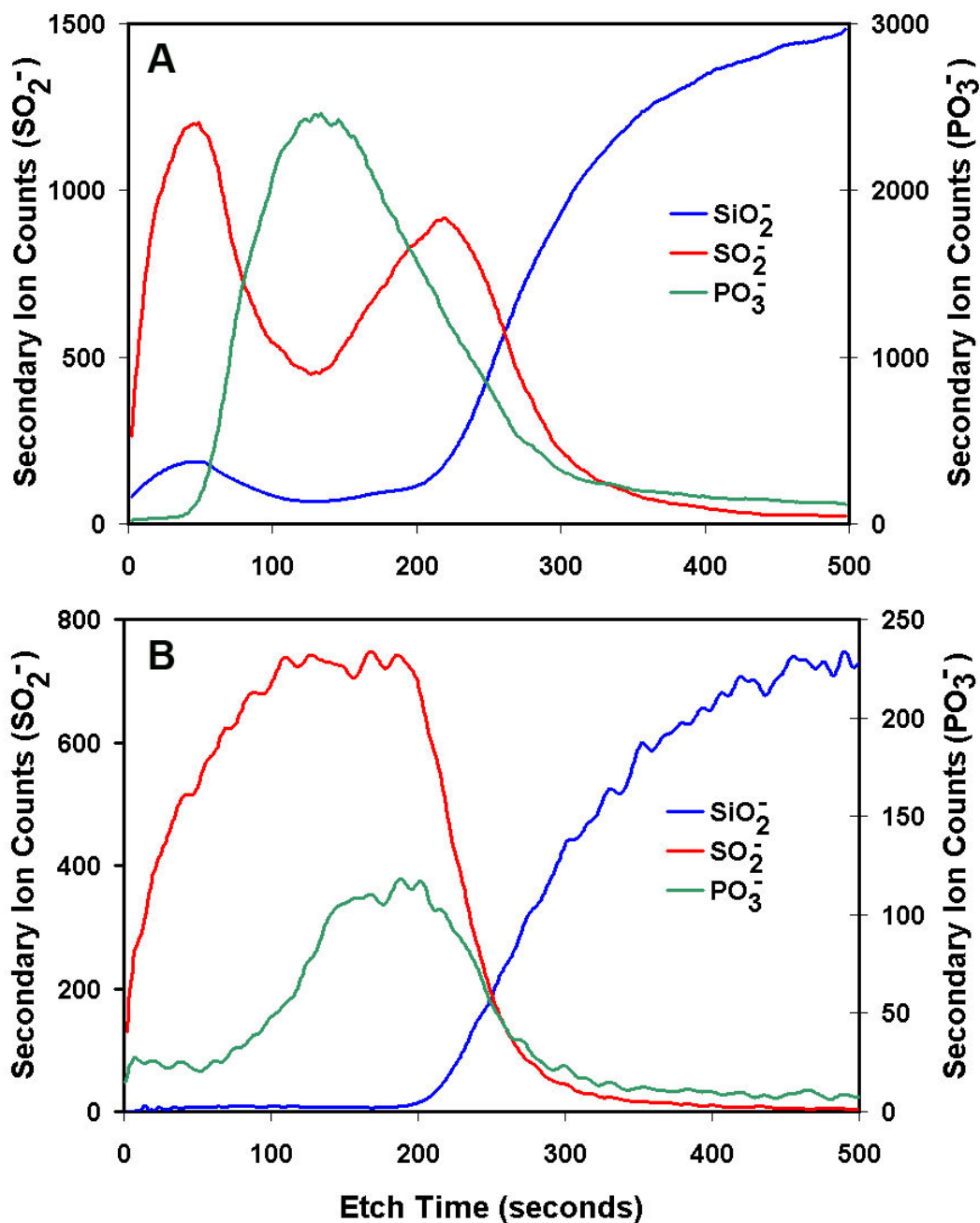


Figure 2-8: ToF-SIMS sputter profile from the proof of concept work using PSS/PDDA/SA DNA films. These studies aimed to demonstrate the continuing function of the SB aptamer (SA) in binding the target dye (SB) while in a film matrix. The SO_3^{2-} ion was used to track both PSS and the SB dye and the PO_3^{3-} ion was tracked for SA DNA. (A) Films before dye binding showing distinct stratification of PSS/DNA layers within the film. (B) Films after incubation in SB dye. DNA and dye ions show similar temporal trends suggesting co-localization of the dye and DNA within the films. (Reproduced with permission)^[164].

indicating their presence in the films. The CHI/HA/SA film retained more SB dye than by the CHI/HA/RO film as indicated by the SO_3^{2-} peak in Figure 2-7. The shape of the CHI/HA/SA dye peak is promising as it appears more shifted than the CHI/HA/RO peak suggesting that the dye may be within the film rather than on the surface. As a more accurate comparison, a ratio of dye (SO_3^{2-}) to DNA (PO_3^{3-}) was calculated for each film which is shown in Figure 2-9. While this confirms that the CHI/HA/SA film has retained more dye compared to the CHI/HA/RO film, both ratios have a value higher than one. As the aptamer has only been confirmed to bind one dye molecule^[15], this is an indication of an overabundance of dye within the films caused by nonspecific binding. This is further confirmed by the large SO_2^{3-} peak that was observed in the CHI/HA/RO film sputter profile (Figure 2-7) which should have no affinity for the dye other

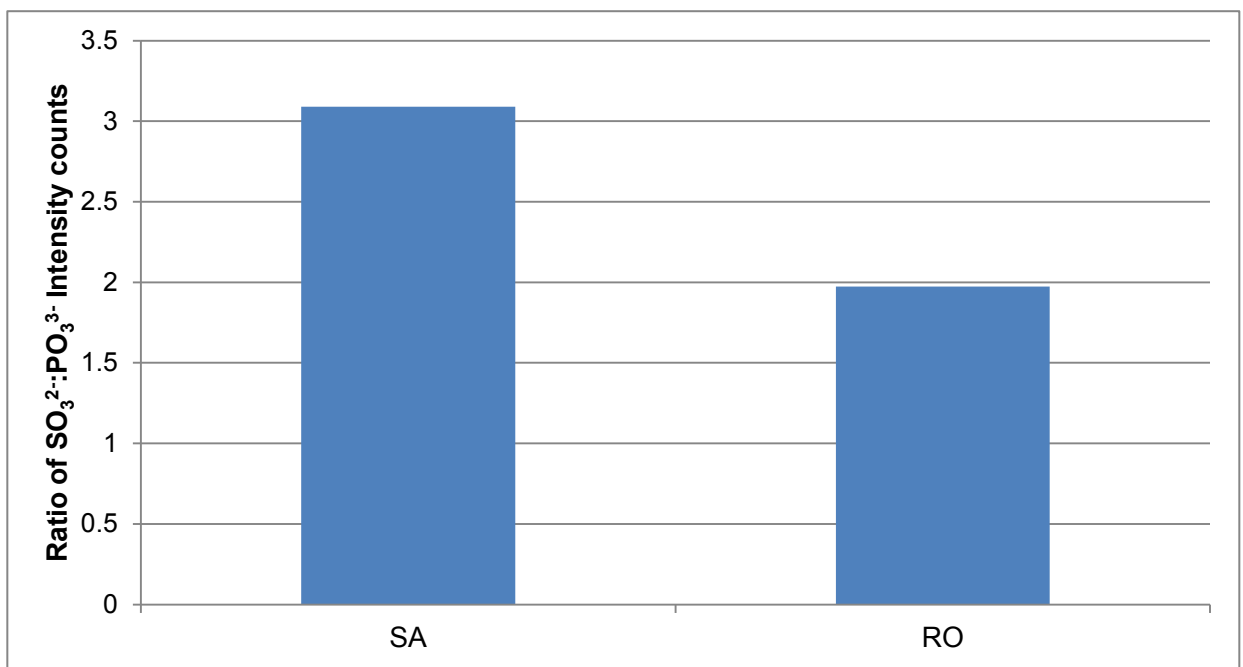


Figure 2-9: Comparison of the ratio of SO_3^{2-} to PO_3^{3-} intensity counts between CHI/HA/SA and CHI/HA/RO films as an indication of binding. Films were exposed to 2mM SB dye.

than inevitable nonspecific interactions. Therefore, a less concentrated dye solution needed to be used.

The proof of concept study also showed that exposing the completed films to elevated temperatures for a finite period of time (annealing) was critical for their ability to bind the target dye^[37]. In addition to reducing the dye concentration, the effect of annealing on target binding was also explored.

Figure 2-10 shows the analysis of the resulting ToF-SIMS profiles.

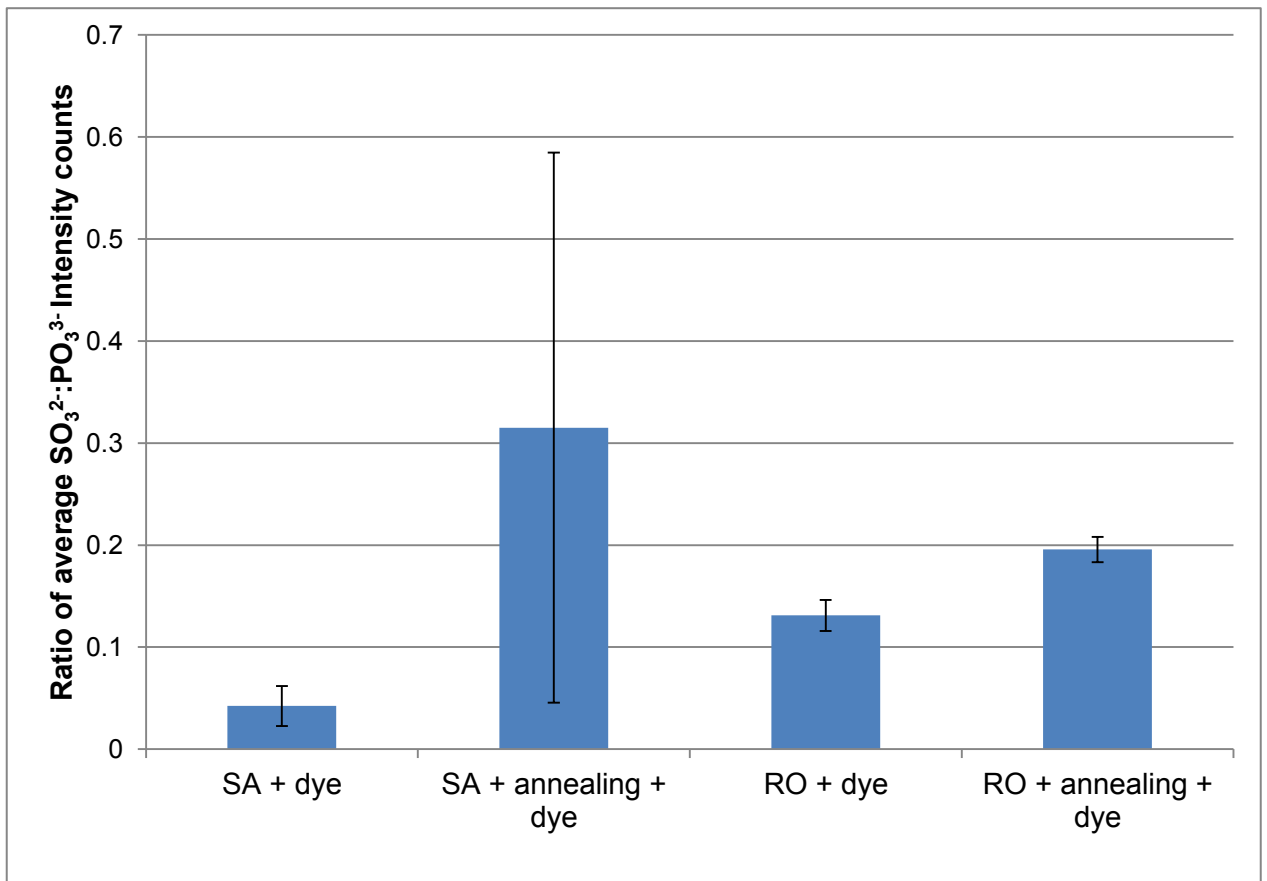


Figure 2-10: Comparison of the ratio of SO_3^{2-} to PO_3^{3-} intensity counts between CHI/HA/SA and CHI/HA/RO films as an indication of binding. Exposed films were incubated in 200 μM SB dye. Annealed films were heated at 70°C for 10 minutes in 0.15M NaCl. At least two spectra were taken per sample.

Annealing appeared to increase the amount of dye bound in both the SA and RO samples compared to their non-annealed equivalents. The error in the annealed SA film was extremely high compared to the other samples. Unexpectedly, of the non-annealed samples, the RO film bound more dye than the SA films which was the complete reverse of the trend seen in the previous ToF-SIMS analysis (Figure 2-9). Attempts to reproduce these results and decrease the error seen were unsuccessful. UV-Vis and FTIR were also attempted to quantify target binding but were unsuccessful due to dye levels being below the limit of detection of both techniques.

Fluorescent microscopy of the CHI/HA/SA and CHI/HA/RO films shed light on the issues seen in ToF-SIMS analysis (Figure 2-11). Using the fluorescence of the SB dye, FM showed that the dye was not uniformly distributed throughout the film, but rather was located in highly concentrated areas of binding. This indicated that point- analysis methods (as by ToF-SIMS) could not yield results that were truly representative of the binding behavior of the film as a whole, and that a method with the ability to perform larger-area analysis was required. Thus, ToF-SIMS was abandoned in favor of FM.

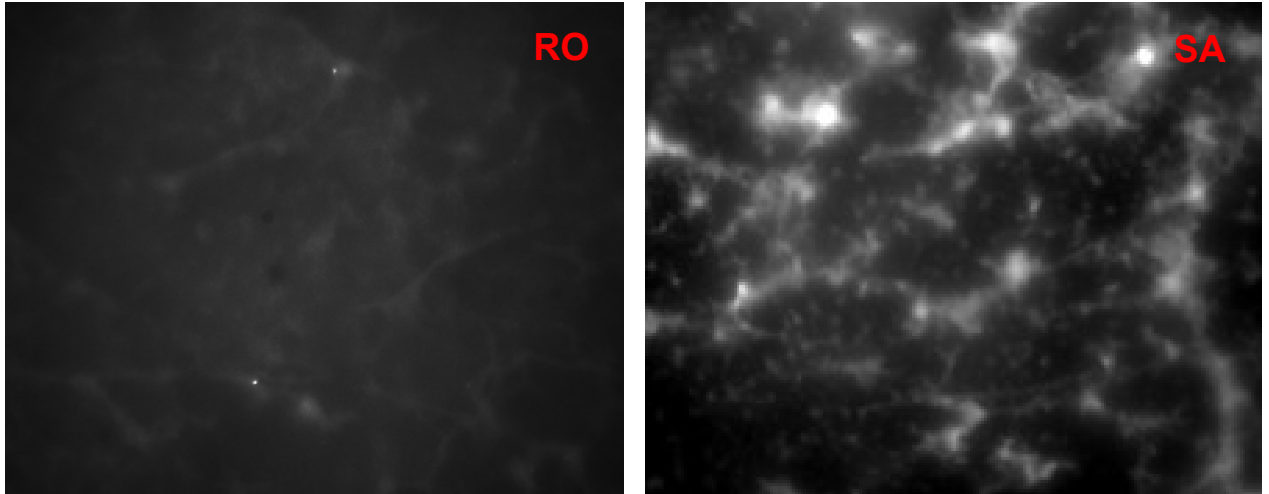


Figure 2-11: Representative FM images ($\lambda_{em}=594nm$) tracking the fluorescence of SB dye in CHI/HA/DNA films made with either SA (right) or RO (left) DNA. Films were prepared by the original method of deposition and were imaged dry. Images represent an area of $602 \times 452\mu m^2$.

2.3.3. Fluorescent microscopy analysis of target binding

As shown in Section 2.3.2, zones of SB dye binding were not uniform throughout the film and rather formed distinct regions indicating the need to analyze larger areas of the film to gain perspective on the film as a whole.

Original Method versus Modified Method: the effects of annealing on dye binding

The effects of changing rinse times and volumes appear to have considerable effects on the interaction of the films with the target dye (Figure 2-12). Films produced by the modified method show an increased level of dye binding. This binding is most likely nonspecific in nature due to the differences seen in dye binding between films containing RO DNA which has been shown to have no affinity for the target dye in the proof of concept work^[36,37]. SB dye is negatively charged and therefore will inevitably have some interaction with the

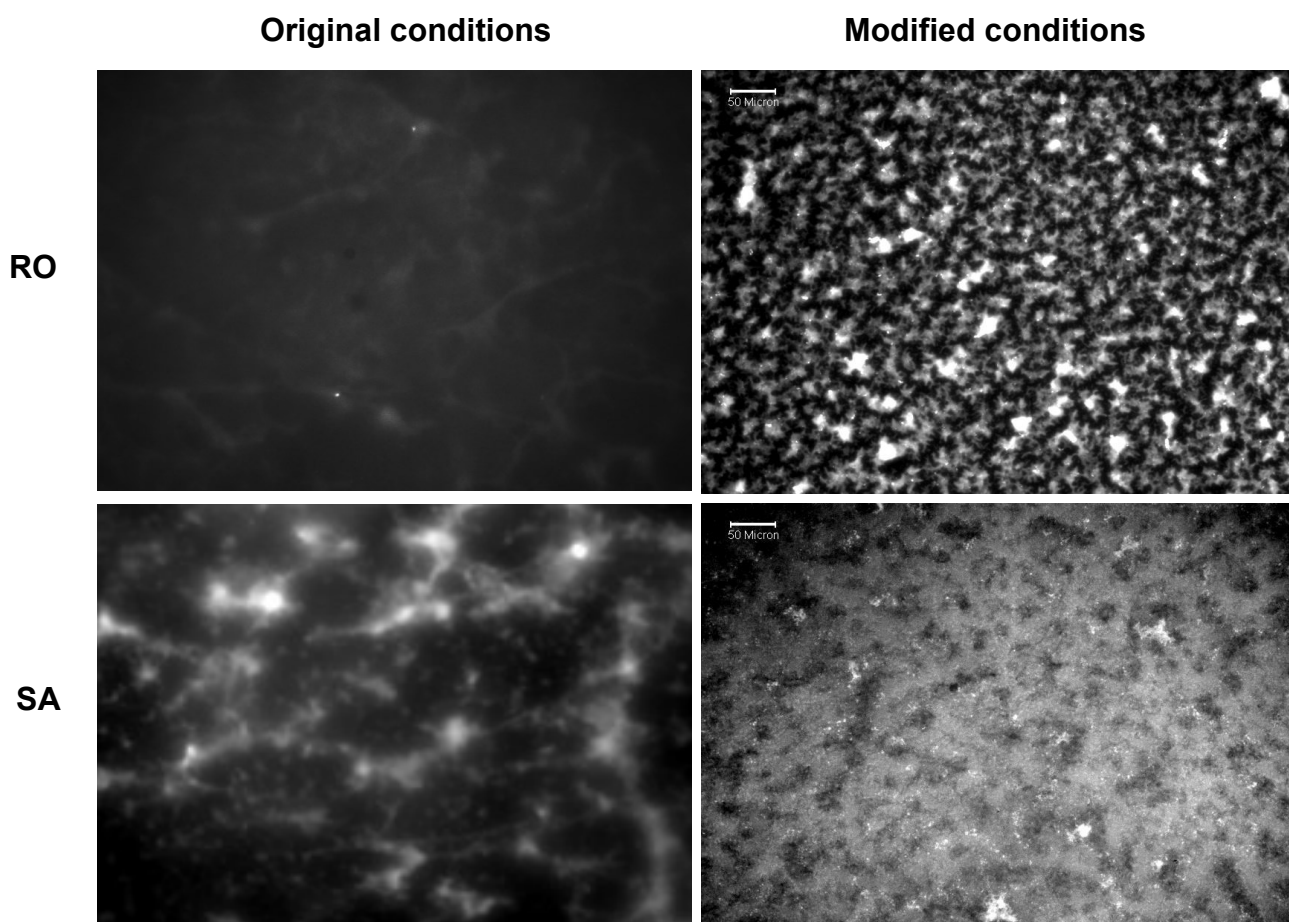


Figure 2-12: Comparison of SB dye binding in CHI/HA/DNA films with either RO (top) or SA (bottom) after exposure to 200 μ M SB dye. Images were taken by FM (λ_{em} =594nm) tracking the fluorescence of SB dye. Films were prepared by the original method (left) and modified method (right) of deposition and were imaged dry. Films were not annealed. Scale applies to both image sets.

films due to the nature of their construction. The increased rinse times employed in the modified deposition method may result in less PE composing the film network forming a film that is less dense and sterically hindered, allowing the dye increased access to the film interior. Within the film, the dye may be able to displace the ions neutralizing fixed positive charges and assume their counter-active role, thus interacting nonspecifically (electrostatically) with the film matrix. This argument is appealing especially since the fluorescent images strongly resemble optical and SEM images taken of the films and show distinct

morphological features (See Figures 2-3 to 2-5). Studies of the diffusion behavior of counter-ions within linear and exponentially growing films are complicated and often contradictory. A more recent study by Ghostine *et al* with PSS/PDDA films addresses a lot of the current issues in this field. Among other things, they found after the deposition of 12-14 bilayers, PSS is no longer able to compensate for all positive charges of PDDA^[88]. As a result, counter-ions from the surrounding solution must permeate the film to neutralize these fixed charges. This transition may occur sooner in CHI/HA films. PSS is likely superior to HA at compensating positive charges as every monomer is charged, whereas the repeated unit of HA consists of one charged and one uncharged group. Despite the increase in nonspecific binding seen in the modified method films, the trends in dye binding seem to be similar with the original method films in that films prepared with SA DNA show more interaction with the target dye than films prepared with RO DNA.

The effect of heat annealing was also explored in films prepared by the original method of deposition. Annealing appeared to have a detrimental effect on the specificity of dye interaction, causing fluorescence levels in CHI/HA/RO films increased dramatically as a result of the process (See Figure 2-13). Thermal annealing provides energy allowing structural rearrangements throughout the film that may not have been possible at room temperature^[87]. As this process is performed in 0.15M NaCl, these rearrangements may not serve to pair more charges between the polyelectrolytes but rather optimize different interactions such as hydrogen bonds or lessen steric repulsion within the film.

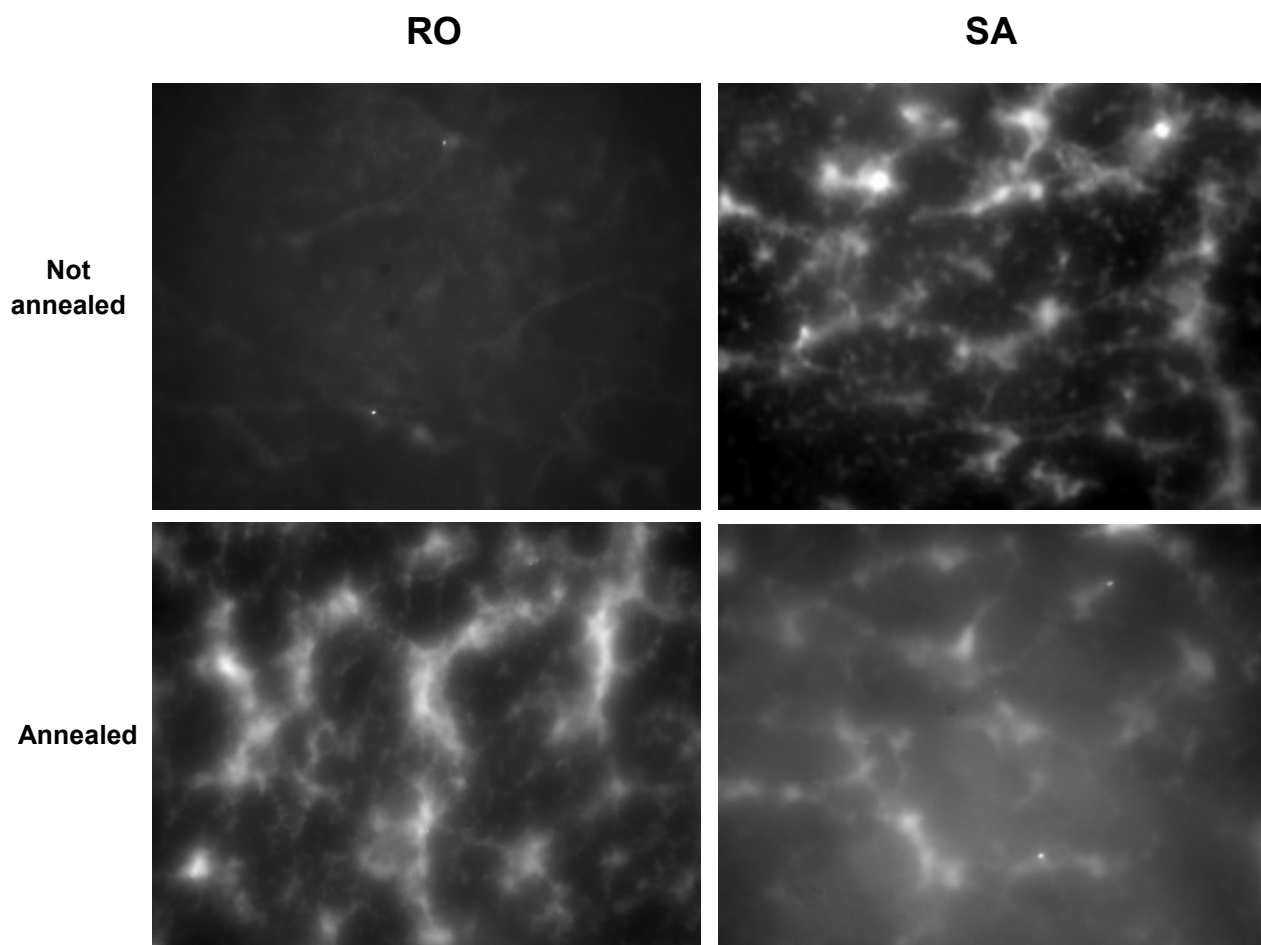


Figure 2-13: Comparison of SB dye binding in CHI/HA/DNA films made with either RO (left) or SA (right) that have (bottom) or have not (top) been subjected to heat annealing. Images were taken by FM ($\lambda_{em}=594nm$) tracking the fluorescence of SB dye. Films were prepared by the original method of deposition and were imaged dry after exposure to 200 μ M SB dye. Images represent an area of 602 x 452 μ m².

This is possible due to the abundance of ions available to shield fixed charges and thus decrease electrostatic repulsion. As a result, there are more fixed charges available for interaction with the charged SB through ion displacement and nonspecific binding of the dye to the film increases. Alternatively, the effects of the heat and structural rearrangements may loosen the film structure, either temporarily or with partial permanence, allowing excess PE that was already loosely associated with the film matrix (due to short rinsing times and small rinse

volumes) to escape. This effect could increase the number of fixed charges needing to be compensated. Material loss has been seen in PSS/PDDA microcapsules upon annealing^[119].

The effect of deposition temperature on film growth was studied by Salomaki *et al* who found that linearly growing PSS/PDDA films would transition to exponential growth by performing the deposition at 55°C^[87]. This change was attributed to increased diffusion of the PE in and out of the film allowing for the increased mass deposition characteristic of exponential growth. Increased temperatures were found to induce reversible swelling of the film matrix and could provide the energy to overcome normal thermodynamic barriers to accommodate the increased flux of PE^[87,119]. Salomaki *et al* did report that changing the deposition temperature after a film had been well established had limited effects on the mass of the new layers deposited^[87]. However, this study was performed on a 60-bilayer film and therefore the effects are expected to be much less dramatic due to the strict diffusion constraints imposed on films of this thickness. The 10-bilayer films used in this study will not be as limited.

Annealing proved to be an essential addition to the proof of concept work performed on PSS/PAH/DNA microcapsules^[37]. Heating the films was hypothesized to allow proper folding of the aptamer sequence into the conformation required for target binding^[37]. PSS and PAH films grow in a linear fashion and therefore have very directed interactions between bilayers leading to a distinct layer structure which could interfere with proper aptamer folding. Exponential growing systems, such as CHI/HA, are much more loosely

associated and may not have as large of an impact. Due to the effects of target binding seen, the annealing process was not continued.

Target dye binding—Original method

FM was also used to determine the ability of SA to bind SB dye while sequestered in a film matrix. While the presence of SB dye in the films was confirmed (as discussed previously), these results did not shed light on the relative location of the DNA or confirm the co-localization of both species within the film. Using fluorescently labeled DNA, SB dye was found in the same regions as the DNA within the CHI/HA/SA films and to a lesser extent in the CHI/HA/RO films indicating that the presence of dye within the films solely due to nonspecific interactions is unlikely (Figure 2-14). The mean fluorescence from each channel was calculated using ImageJ and expressed as a ratio to quantify the dye bound by each film (Figure 2-15). The ratio of dye to DNA was significantly higher for the CHI/HA/SA film ($p=0.0008$, $\alpha=0.05$) confirming the ability of the aptamer to bind its target within a film matrix. Interestingly, all FM images analyzed indicated a higher loading of RO DNA within the films as compared to SA DNA. This may be due to the conformational differences between the two sequences that result in structural consequences within a film. RO is much less structured than SA which folds into a G-quadruplex (See Figure 2-1). This extended conformation may have more charges available for interaction with the PE network in the film compared to the G-quadruplex.

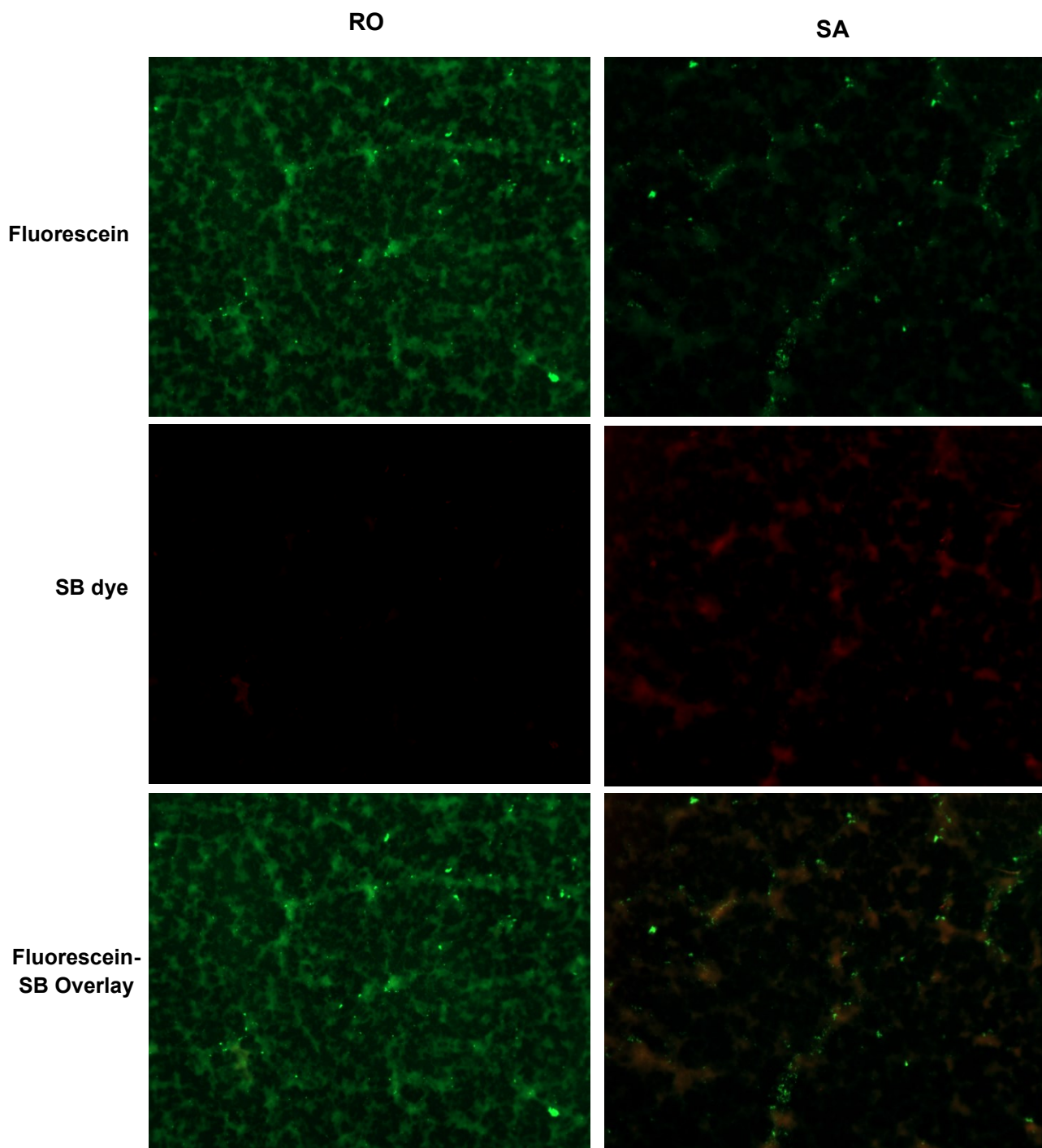


Figure 2-14: Representative FM images of CHI/HA/6-FAM DNA multilayer films exposed to 200 μ M SB dye showing co-localization (Fluorescein-SB overlay; orange) of DNA (Fluorescein; green) and SB dye (SB dye; red) fluorescence as an indication of binding. Films contain either RO DNA (left) or SA DNA (right). Films were prepared using the original method of deposition. Images represent an area of 1048 x 789 μ m².

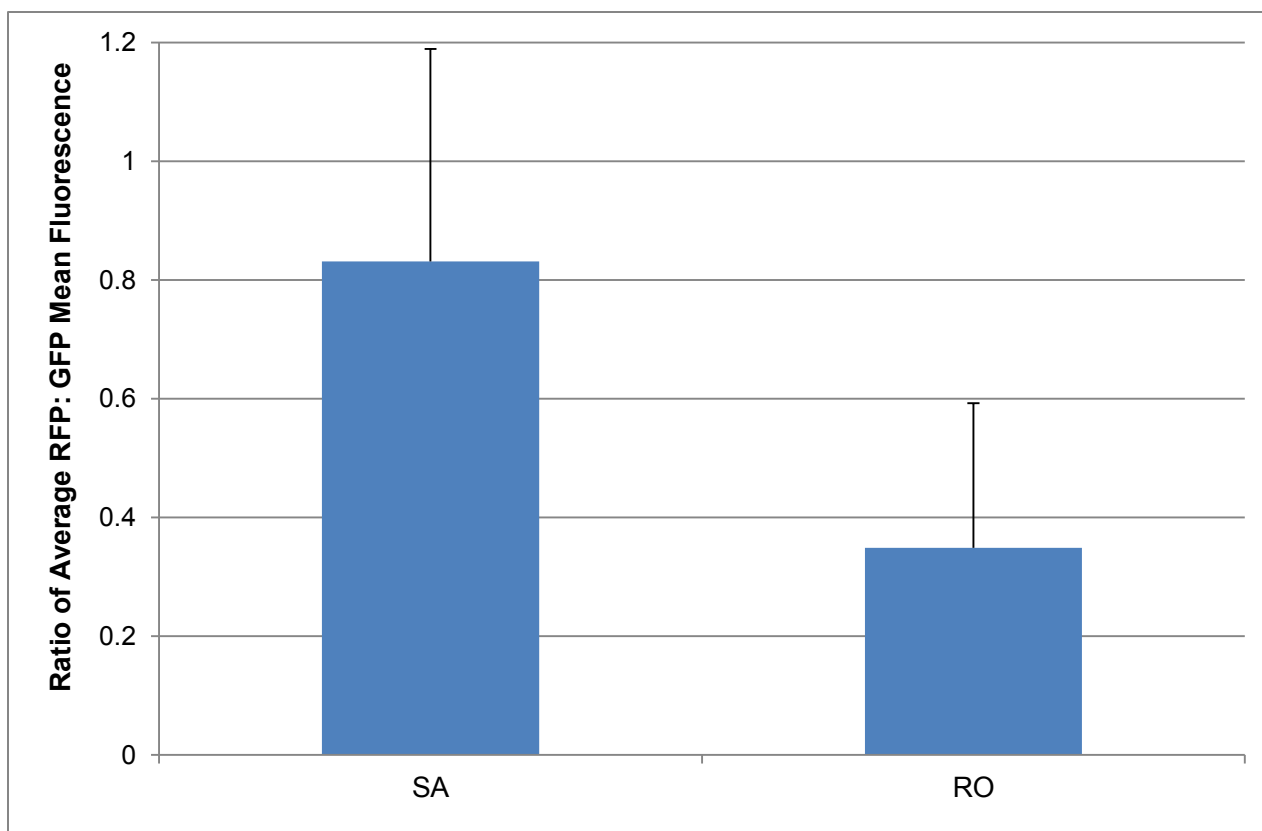


Figure 2-15: Comparison of the average RFP:GFP mean fluorescence ratio between CHI/HA/6-FAM DNA films containing either SA or RO DNA (N=11) as an indication of binding. Films were prepared by the original method of deposition and exposed to 200 μ M SB dye. Error bars represent standard deviation. Difference between the ratios is statistically significant ($p < 0.05$).

The size difference between the DNA and the PEs could also contribute to this effect. Both SA and RO are quite small (9,225Da and 8,940Da for SA and RO respectively) compared to the PEs used in this experiment (See Table 2-2). The G-quadruplex structure transforms this small DNA polymer into an even smaller, more compact entity. This may allow SA DNA to diffuse from the film more readily especially if the structure is already loosely associated with the film matrix due to the limited availability of charges. As it is unclear whether binding induces a conformational change in an aptamer or the sequence is pre-folded^[30], it is

Table 2-2: Review of deposition conditions from literature comparing key parameters of CHI/HA film experiments^[70,79,101,108,120]. Asterisks show conditions with confirmed exponential growth.

| Group | Technique(s) | Deposition Time (min) | PE Volume (mL) | PE Change Frequency | Rinse Times | Rinse volume (mL) | Rinse Change Frequency | PE Molecular weight (g/mol) |
|-----------|--|-----------------------|----------------------|--------------------------------------|---|---|---------------------------------|--|
| Foster | <ul style="list-style-type: none"> UV-Vis Hand-dipped | 15 | 10 | 20 layers | R ₁ = 10s R ₂ = 5s | R ₁ = 10 R ₂ = 10 | 20 layers | HA= 1,580,000 CHI= 135,000 |
| Mulligan | <ul style="list-style-type: none"> AFM Ellipsometry | 15 | Not specified | Not specified | R ₁ = 1 min R ₂ = 5 min | R ₁ = 350 R ₂ = 150 | 3 layers | HA= 163,000 CHI= 50,000 |
| Kujawa* | <ul style="list-style-type: none"> SPR AFM | 20 | 10 (total) | Each use | Not specified | 10 (total) | Each use | HA ₁ = 360,000 HA ₂ = 31,000 CHI ₁ = 160,000 CHI ₂ = 30,000 |
| Picart | <ul style="list-style-type: none"> ATR-FTIR CLSM QCM Auto-dipped | 15 | 12 | Not specified | R ₁ = dip R ₂ = 2.5 min R ₃ = 2.5 min | R ₁ = 350 R ₂ = 40 R ₃ = 40 | 6 layers | HA= 400,000 CHI ₁ = 5,000 CHI ₂ = 100,000 |
| Schneider | <ul style="list-style-type: none"> AFM CLSM Auto-dipped | 15 | 12 | Not specified | R ₁ = dip R ₂ = 2.5 min R ₃ = 2.5 min | R ₁ = 350 R ₂ = 40 R ₃ = 40 | 6 layers | HA= 400,000 CHI= 5,000 |
| Richert* | <ul style="list-style-type: none"> OWLS AFM QCM-D Auto-dipped | 15 | 15 or 0.5 (QCM-D) | Not specified or each use (QCM-D) | R ₁ = dip R ₂ = 6 min R ₃ = 6 min or 10s (QCM-D) | R ₁ = 350 R ₂ = 40 R ₃ = 40 or 0.5 (QCM-D) | 3 layers or each use (QCM-D) | HA= 400,000 CHI ₁ = 110,000 CHI ₂ = 270,000 CHI ₃ = 460,000 |

possible that the conformation change induced in SA upon target binding allows for the escape of DNA-target complexes. This could be through a combination of conformational compactness and competition with the film matrix for interaction with the aptamer sequence. This is further supported by control films prepared with 6-FAM DNA for CHI/HA/RO and CHI/HA/SA films which do not show the same depositional bias (images not shown). This effect was investigated by UV-Vis spectrophotometry and will be discussed later.

Target dye binding— Modified method

The same process was repeated for films prepared by the modified method with much different results. No co-localization could be determined due to the extensive interaction between the SB dye and the film matrix (Figure 2-16). This was further confirmed by calculating the dye to DNA ratio (Figure 2-17) which yielded ratios that had no significant difference ($p=0.3742$, $\alpha=0.05$) between the CHI/HA/SA and CHI/HA/RO films and large standard deviations. Interestingly, clear pockets can be seen in the RFP channel images for both film types which perfectly coincide with the locations of DNA fluorescence (Figure 2-16). Fluorescence of the SB dye could be blocked by the presence of DNA leading to the darker color (reduced fluorescent intensity) of these pockets. The differences seen between the original and modified method films can be attributed to the differences in PE film density as discussed previously. Dye is seen only in the regions inhabited by DNA in the films prepared by the original

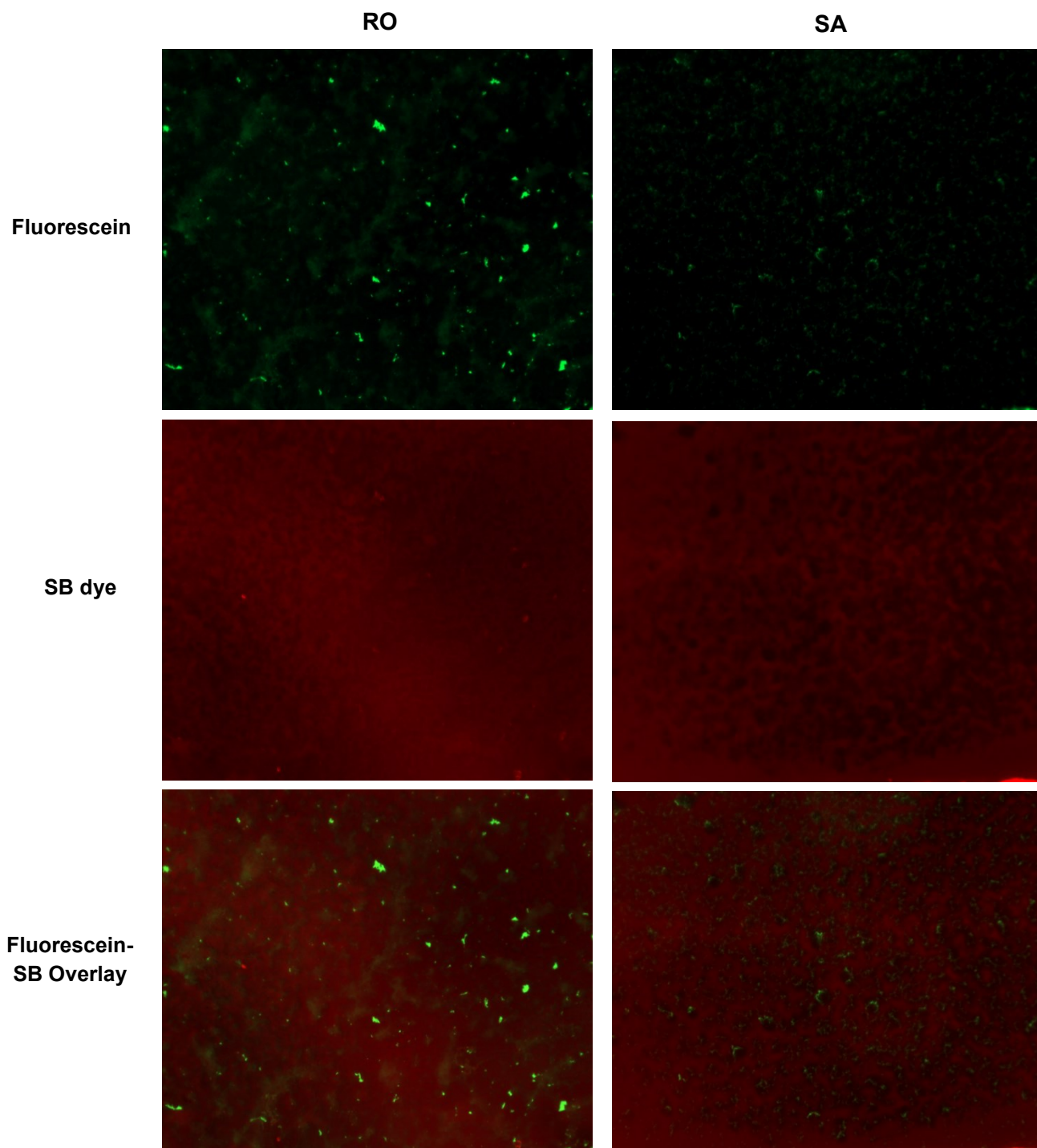


Figure 2-16: Representative FM images of CHI/HA/6-FAM DNA multilayer films exposed to 200 μ M SB dye showing co-localization (Fluorescein-SB overlay; orange) of DNA (Fluorescein; green) and SB dye (SB dye; red) fluorescence as an indication of binding. Films contain either RO DNA (left) or SA DNA (right). Films were prepared using the modified method of deposition. Images represent an area of 1048 x 789 μ m².

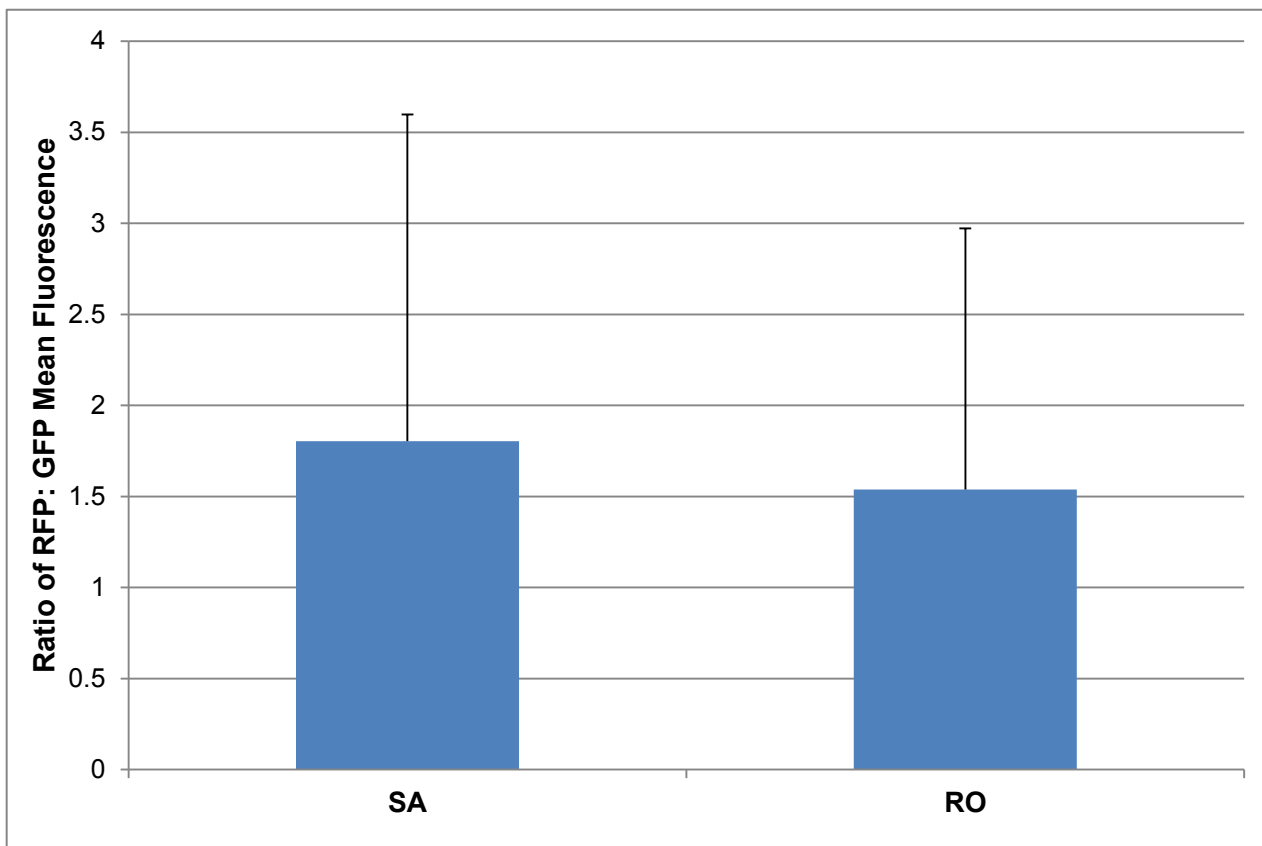


Figure 2-17: Comparison of the average RFP:GFP mean fluorescence ratio between CHI/HA/6-FAM DNA films containing SA or RO DNA (N=8) as an indication of binding. Films were prepared by the modified method of deposition and exposed to 200 μ M SB dye. Error bars represent standard deviation.

method which arise from binding events. In the modified method films, the decreased steric limitations on film permeability allow the dye increased access to the film and the nonspecific interactions that occur prevent or mask any binding events that (could) occur. As in the original method films, the RO sequence was again seen in higher levels than SA in the films.

2.3.4. Investigation of film growth by UV-Vis spectrophotometry

CHI/HA film growth

The initial protocol successfully produced rough, but continuous films after the deposition of sixteen bilayers where the initial ten CHI/HA bilayers serve as a base for further growth (as discussed in Section 2.3.1). However, these were studies on an end product and did not shed light to the manner in which these films were growing with each additional deposition step to yield the resulting film. The growth of the CHI/HA base can be observed by UV-Vis spectrophotometry by monitoring the absorbance of glucosamine and N-acetylglucosamine which absorb between 190-220nm^[78,121,122]. N-acetylglucosamine is the predominant chromophore in this range and is present in HA and to some extent CHI^[78,121,122]. CHI is produced by the deacetylation of chitin using highly concentrated alkali at high temperatures; however this does not always yield the ideal 100% deacetylation. This CHI used in all experiments has a degree of acetylation (DA) of 10% and therefore minimally contributes to the absorbance of this species. The absorbance of glucosamine is solely contributed by CHI.

The condition-set initially explored gave a linear-like growth pattern with each additional CHI/HA bilayer deposited (See Figure 2-18). This was unexpected as previous studies published in literature describe this system as growing exponentially^[74,79,101]. Comparing published deposition conditions reveals that there is considerable variation between methods used to produce CHI/HA films (See Table 2-2). Previous studies have shown that polyelectrolyte molecular weight and deposition conditions play a large role in the manner in

which films grow and their morphology. Richert *et al* studied the effects of salt concentration (0.15 , 10^{-2} , and 10^{-4} M) and the molecular weight (See Table 2-2) of the diffusible PE (CHI) on CHI/HA film formation^[79]. Using QCM-D, the measured PE mass deposited decreased with lower salt concentrations and film growth transitioned from exponential (0.15 M) to linear (10^{-4} M). This remained true for new bilayers deposited, even if the film was previously built at higher ionic strength. Islet size and thickness decreased with lower ionic strength and

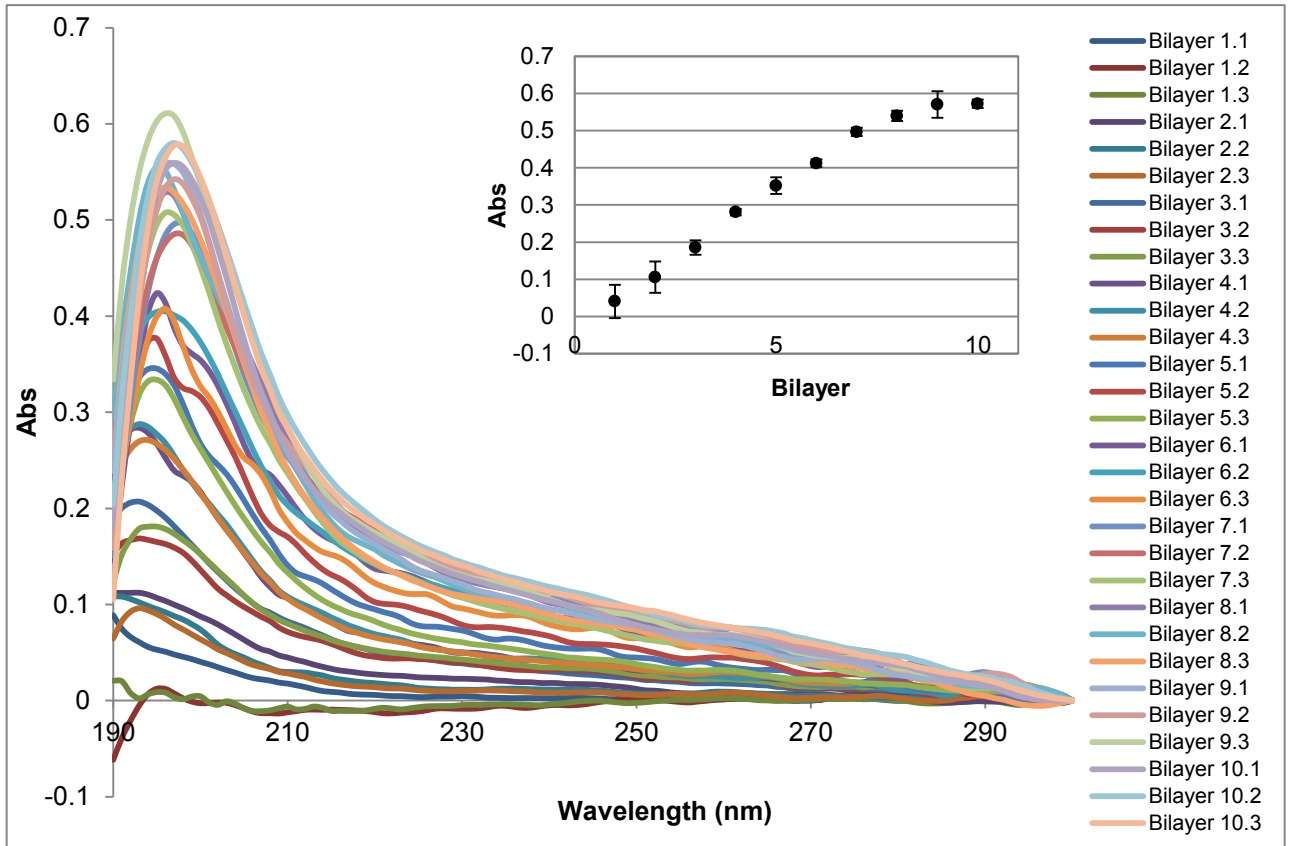


Figure 2-18: UV-Vis spectrophotometry analysis monitoring the growth of CHI/HA bilayers deposited by the original protocol. Growth was measured by tracking the absorbance of CHI and HA between 190-220nm. Three trials were done for each bilayer to account for minor compositional variances. All data was normalized to 300nm. Water rinse was for 5s. Inset: Plot of the average absorbance (N=3) between 190-220nm depicting the growth trend of the CHI/HA film. Error bars represent standard deviation.

the transition from islet to film morphology was delayed in the case of films built at 10^{-2} M NaCl compared to 0.15M. The transition could not be achieved at all in films built at 10^{-4} M. This was attributed to the re-dissolution of unstable CHI/HA complexes due to the ionic strength of the solution. For CHI of different molecular weights, film growth remained exponential showing that the films are permeable to different PE masses. The results found by Richert *et al* suggested the rate of growth is more rapid with smaller molecular weight however; this was complicated by the viscoelastic properties that become dominant with CHIs of larger molecular weight. Kujawa *et al* shed further light on the effects of molecular weight in CHI/HA films finding that the growth rate does not depend on the molecular weight^[101]. Molecular weight influences the transition to the exponential growth phase which in turn results in thicker films rather than a larger deposition of mass per layer formation. The molecular weight of both the diffusing and non-diffusing species affects this phenomenon with larger molecular weights transitioning earlier and thereby producing thicker films after the deposition of a given number of bilayers. This trend also holds true to the transition between island and vermiculate morphology. Despite this, lower molecular weight PE produce rougher films, with larger morphological structures. The independence of the film growth rate from molecular weight has been confirmed in other systems as well^[82].

From a quick overview of the conditions listed in Table 2-2, it becomes clear that there are a wide variety of rinsing methods which differ in many parameters including time, volume, and frequency of solution changes. The

initial method used to produce CHI/HA films involved short rinsing times, in small volumes of rinse solution (0.15M NaCl pH 4.5) that was infrequently changed; a much different protocol than those used in literature. Rinse times were increased ($R_1= 1$ min, $R_2= 5$ min) and volumes changes slightly ($R_1= 10$ mL, $R_2= 12$ mL) in order to better emulate the literature protocols (the modified protocol). Rinse solutions were also changed more frequently. The water rinse (10mL) time was also lengthened (1min). Figure 2-19 shows the resulting growth curve for CHI/HA films produced by this method. The linear-like growth seen before was replaced by a more exponential-type growth however; this only extends to

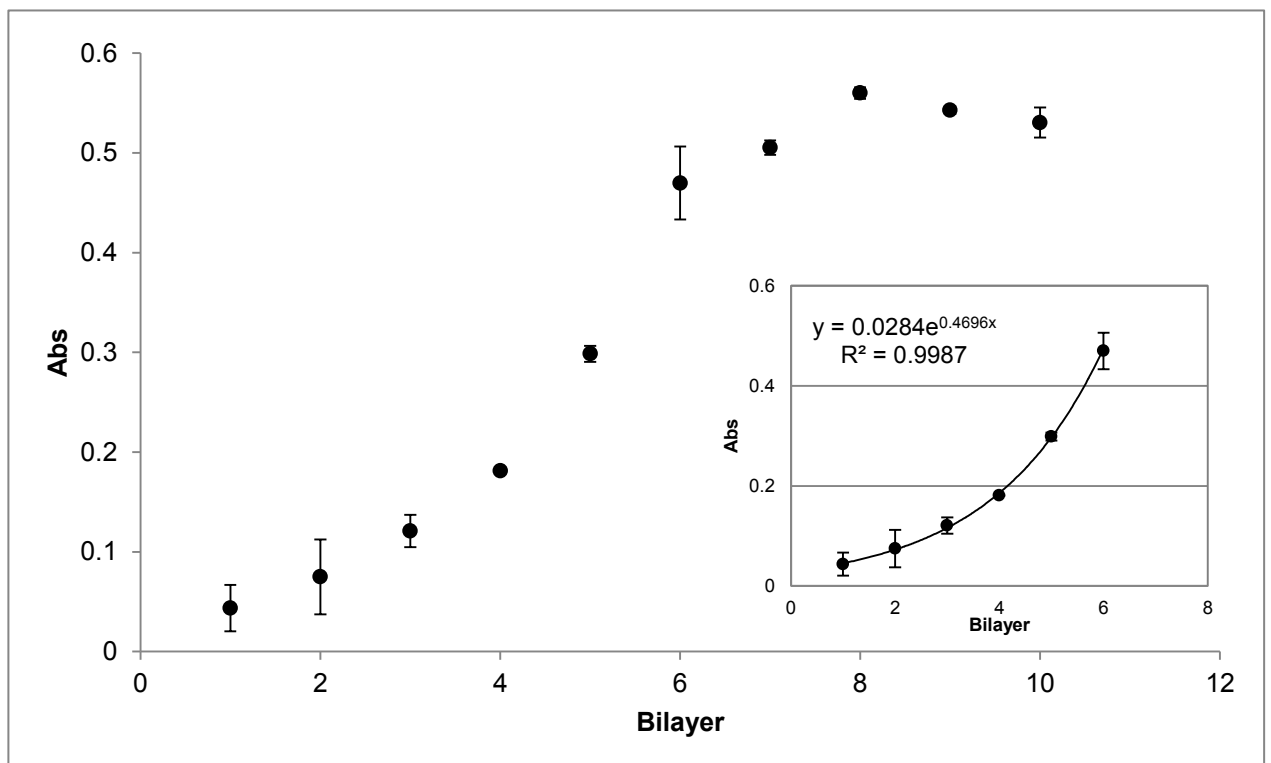


Figure 2-19: Plot of the average absorbance between 190-220nm monitoring the growth of CHI/HA bilayers deposited by the modified protocol with increased rinse times, volume, and frequency of solution changes. Three trials were done for each bilayer to account for minor compositional variances. All data was normalized to 300nm. Water rinse was for 1 minute. Error bars represent standard deviation. Inset: Exponential region of the growth curve over bilayers 1 to 6.

the first 6 bilayers before the growth decreases dramatically. It was a concern that the drying step between each bilayer deposition was impacting film growth. An additional experiment was performed with two films; the first conducted in the exact method as before with scans in between each bilayer up to six bilayers, and the second where a film was built up to ten bilayers (without intermediate drying steps in between) before drying and UV-Vis spectrophotometry analysis.

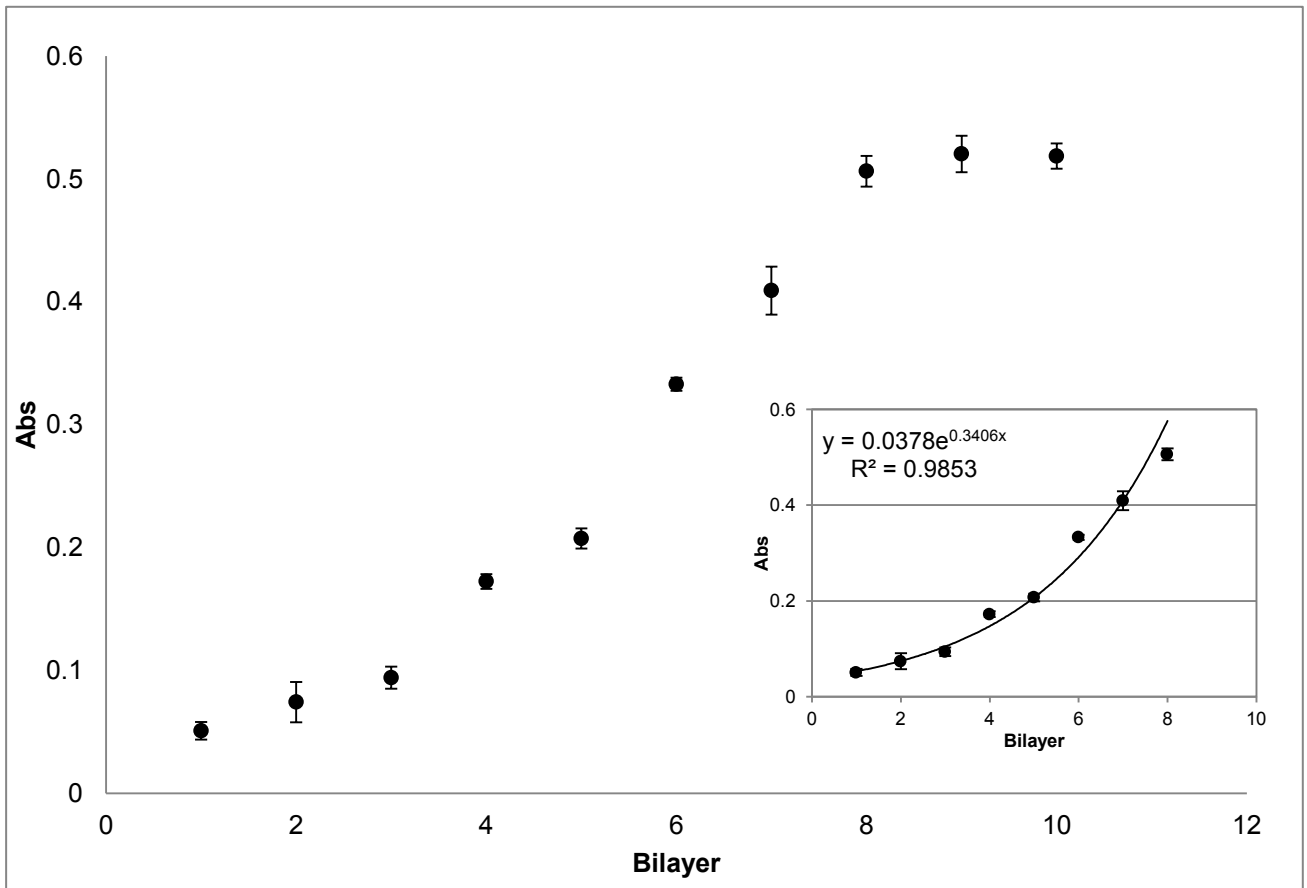


Figure 2-20: Plot of the average absorbance between 190-220nm monitoring the growth of CHI/HA bilayers deposited by an adaptation of the modified protocol where the rinses were changed with every use (FS protocol). Three trials were done for each bilayer to account for minor compositional variances. All data was normalized to 300nm. Water rinse was for 10s. Error bars represent standard deviation. Inset: Exponential region of the growth curve over bilayers 1 to 8.

Through this it could be concluded that the drying process was not affecting film growth and the same decrease was seen even without intermediate drying steps (Appendix).

A variation on the modified protocol where the rinse solutions were changed each use was also studied (FS method). Previous studies showing exponential growth in CHI/HA films employed techniques such as QCM-D and SPR which have alternative protocols from the specified dipping method to suit the apparatus^[79,101]. Because of the nature of these techniques, fresh solutions are often used in each deposition step. A ten second water rinse was performed before each scan. Figure 2-20 shows the resulting growth curve from this method. The growth was very similar to the results obtained from the modified protocol, with the exception that the exponential-like growth was extended two bilayers further. The onset of the exponential growth phase is slightly delayed as a result of the additional washes. The film grows more slowly; requiring 8 bilayers to reach an absorbance of ~ 0.5 compared to the modified method, which required 6 bilayers.

Another variation, modeled after the Mulligan *et al* protocol, involved increasing the rinse volumes used^[120]. The original protocol parameters used by are listed in Table 2-2. Mulligan *et al* used glass coverslip substrates which were 25mm x 25mm (from e-mail communication) which were approximately twice the size of the slides employed in these studies. Therefore, the original rinse volumes used were scaled down by half ($R_1 = 175\text{mL}$ and $R_2 = 75\text{mL}$). A water rinse (1 minute) was performed before each scan. Figure 2-21 shows the

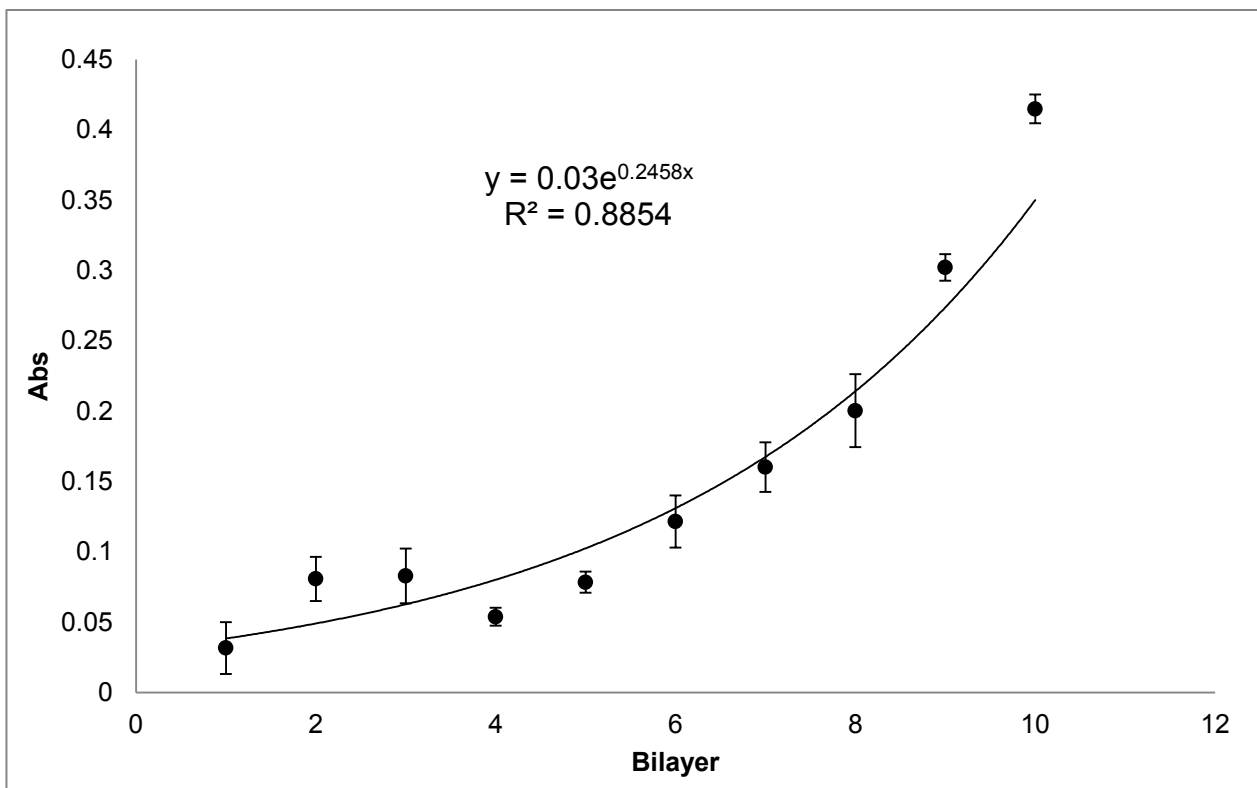


Figure 2-21: Plot of the average absorbance between 190-220nm monitoring the growth of CHI/HA bilayers deposited by an adaptation on the modified protocol with increased rinse volumes (Mulligan protocol). Three trials were done for each bilayer to account for minor compositional variances. All data was normalized to 300nm. Water rinse was for 1 minute. Error bars represent standard deviation.

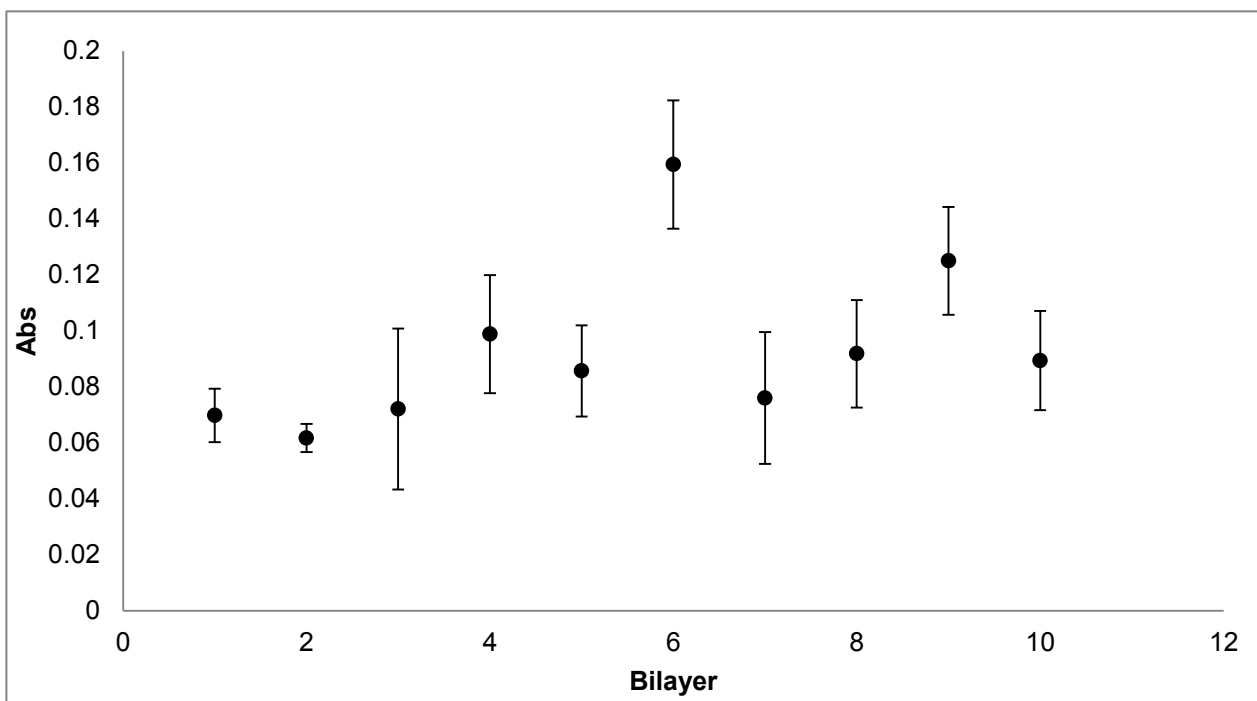


Figure 2-22: Plot of the average absorbance between 190-220nm monitoring the growth of CHI/HA bilayers deposited by an adaptation of the modified protocol with increased rinse volumes, times, and number (Richert protocol). Three trials were done for each bilayer to account for minor compositional variances. All data was normalized to 300nm. Water rinse was for 10 seconds. Error bars represent standard deviation.

resulting growth curve from this protocol. An exponential-like growth trend was seen across all ten bilayers deposited. Compared to the modified method films, the transition into exponential growth is delayed and the growth rate is much slower with the absorbance of all ten bilayers falling under 0.5.

Finally, one last variation on the rinse procedure was explored. This was modeled after the protocol used by Richert *et al* (See Table 2-2). In this method, both rinse volume and the number of rinses increased compared to the modified method. As the substrate size used was unclear, the solution volumes were not changed from the original protocol. A ten second water rinse was performed before each scan. Figure 2-22 shows the resulting growth curve. No visible trends could be discerned. The rinse procedure used by Richert *et al* is much more intense than any protocol used previously and has already proven to successfully yield continuous CHI/HA films after ten bilayers^[79]. Because of this, the amount of PE deposited is reduced below the detection threshold of the UV-Vis spectrophotometer. Richert *et al* was monitoring film growth using AFM which is an extremely sensitive instrument and can detect very small changes. The UV-Vis cannot compete with this level of sensitivity. ATR-FTIR and QCM were attempted to monitor growth, however neither were successful due to technical constraints of the available equipment.

While it is possible to theorize that the films studied (especially those created using the modified and FS method) reach a growth maximum leading to a reduction in deposited material at a higher number of depositions, the trends seen most likely arise from a more technical issue. CHI/HA films of similar

composition have been studied by different methods without consequence^[79,101,108]. In all scenarios (Figures 2-18 to 2-20), absorbance issues (failure to change or gradual decrease in change) consistently arise after an absorbance of 0.5 is reached, suggesting a systematic error. A complete trend is only seen when the growth per step was decreased so that the absorbance of all ten bilayers remained below 0.5 (Figure 2-21). In the first several deposition steps, the CHI/HA films are relatively transparent however they do become increasingly cloudy as deposition continues without becoming truly opaque over the course of ten bilayers. This could contribute to a scattering issue where light is reflected from the sample and fails to reach the detector^[123]. This generally manifests as a higher apparent absorbance value causing a continued increase in measured absorbance independent of the chromophore concentration. However, interactions between the thin film and the light beam may further complicate this phenomenon. Thin films do not interact with light as solutions do; rather they are complicated by inherent morphological planes and differing refractive indices^[124]. Consider the two bilayer system outlined in Figure 2-23. As the incident beam passes through the film, there is a chance that some light may be reflected in another direction^[124]. These reflected beams may still be reflected back to the detector or may be reflected again internally. The incident light is not passing through a homogenous material such as with a solution but rather through a substrate with its own optical properties and refractive index that is flanked by two films (since the dipping procedure exposes each side of the substrate equally) with properties different than its own. While not as distinct, the

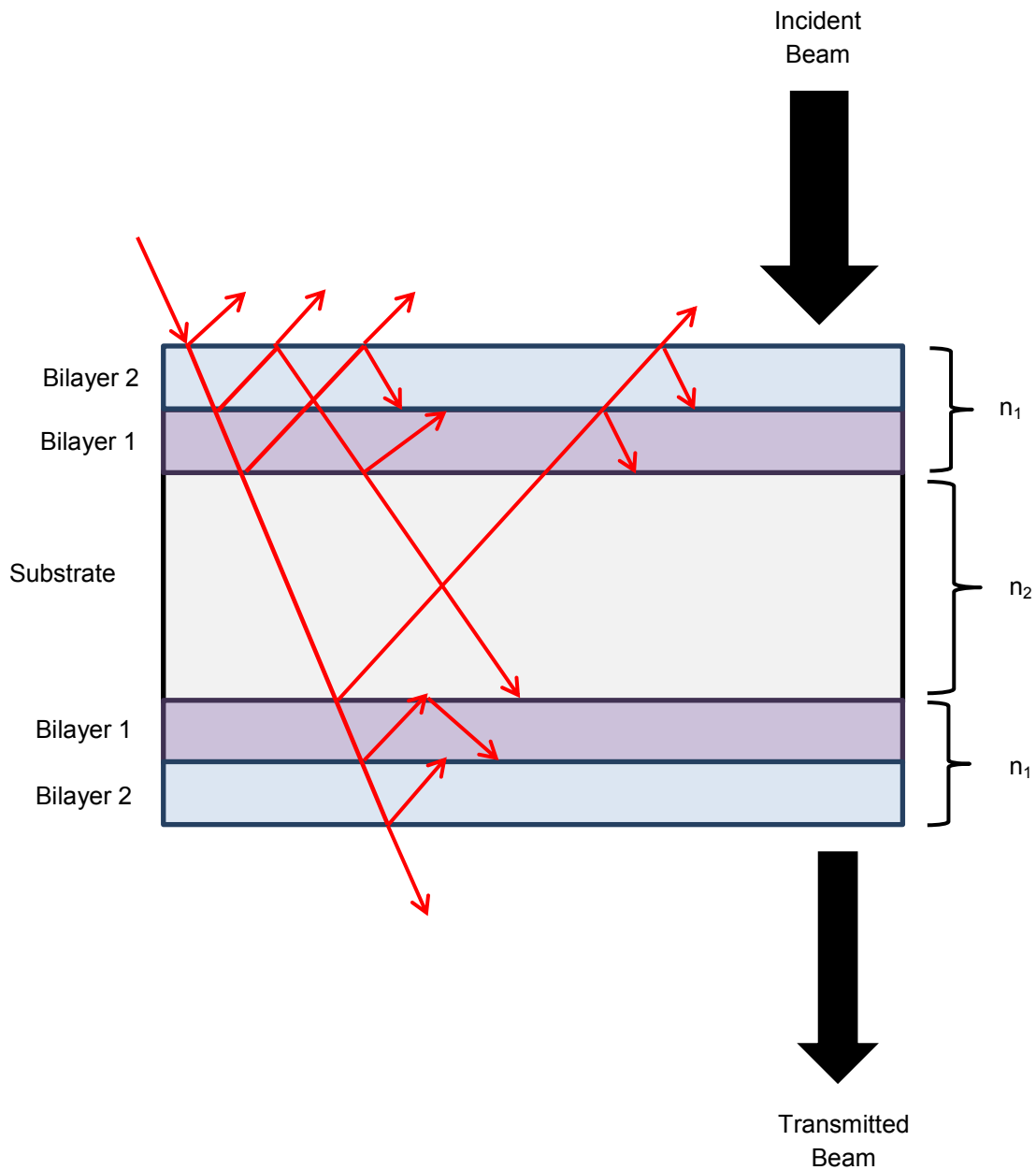


Figure 2-23: Schematic of a two bilayer film system on a substrate (deposited by dipping method) showing potential pathways for light to travel through a film (red). Refractive indices (n) are assumed to be different.

films themselves may have more than one interface within their own morphology as they are deposited as layers. This morphology may be more complicated still due to the mechanism of exponential growth; meaning that some areas may be more homogenous than others. In addition to this, CHI/HA films have rough surfaces with microstructures that become more pronounced as the film grows as discussed in Section 2.3.1 however are not uniform in size across the entire size of the film^[79,101]. The differing refractive indices of the substrate and the film increase the likelihood that some light will be diffracted away from the detector^[124]. With each additional layer, the path of the incident beam becomes increasingly complicated. As the film reaches a certain thickness (when the absorbance is around 0.5-0.6), scattering becomes the predominant contributor to the film absorbance. Very little light remains to be absorbed by the sample (assuming a maximum absorbance of 1.0) and therefore is not reflective of the true amount of chromophore (CHI and HA) in the sample. The effects of scattering were subtracted from the presented graphs by normalizing to 300nm. Beyond the 0.5 mark, the change in absorbance between 190-220nm becomes extremely small suggesting the film stops growing. However when scattering is not subtracted, the growth trend continues and only stops after an absorbance of 1.0 (10% transmittance) is reached (Appendix). Therefore both, wavelength-dependent (absorbance) and wavelength-independent (scattering) components should be considered for an accurate reflection of the growth pattern^[124].

From the experiments performed, it appears that restricting rinse time during all stages of deposition yields a linearly growing film. If the rinse time is

lengthened (constant volume) a more exponential-like growth is seen even with reduced volume. The main outcome of a short rinsing time is an excess of polyelectrolyte; mainly CHI due to its ability to diffuse into the film matrix. After incubation in the CHI solution, the film will be saturated with free or loosely associated CHI. Normally over the course of longer rinse times, some of the CHI would diffuse out of the film until a large enough energy barrier (electrochemical) builds to stop further diffusion^[79]. The amount of CHI that diffuses in and out of a film has not yet been investigated. In shortened rinse times, CHI is not given enough time to diffuse out of the film and thus the film remains saturated into the next deposition cycle. Under the time constraints of the next incubation with HA, the entire reservoir of free CHI will not be complexed with HA and some will remain in the film. This reservoir will persist and grow with subsequent deposition steps forming a “trapped” population of CHI (Figure 2-24). During the next deposition cycle, the film is “topped-up” with CHI and the already sequestered CHI from the previous deposition round remains trapped. Therefore, the same amount of CHI will be deposited in each deposition cycle.

A concept similar to this has already been proposed twice, first by Hubsch *et al* and then by Salomaki *et al* for film systems exhibiting a transition from exponential to linear growth patterns^[87,125]. Several studies have shown that exponentially growing films will exhibit linear growth after the deposition of ten or more bilayers^[82,87,116,125,126]. It was theorized that exponentially growing films become too thick and evolve three distinct domains within their architecture: Domain I which is in contact with the substrate, Domain III which is at the solution

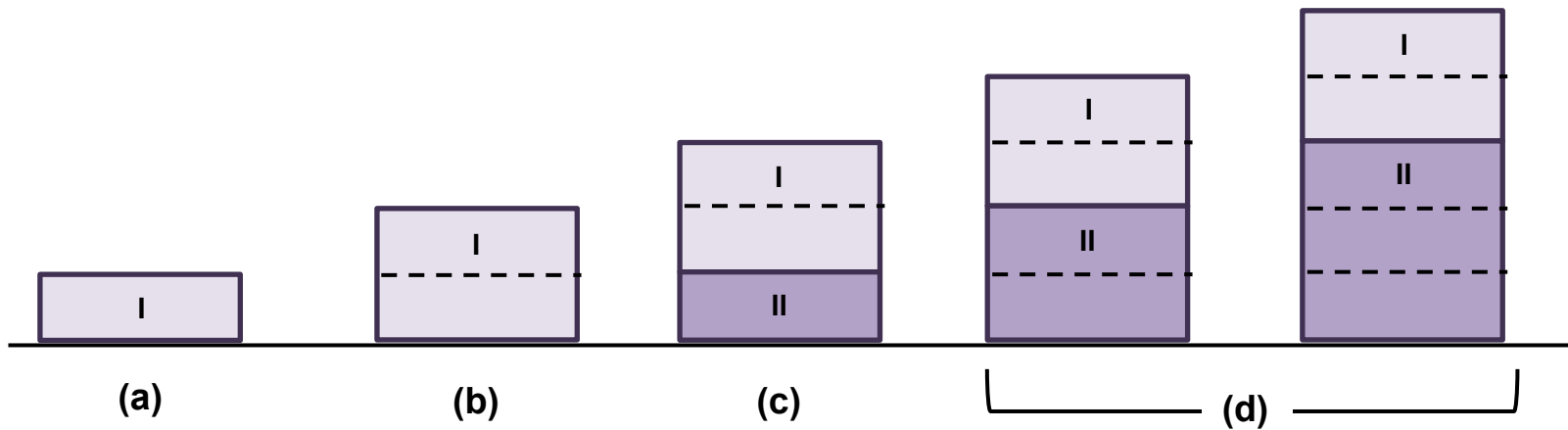


Figure 2-24: Schematic of linear growth mechanism for CHI/HA films; (a) Film is thin enough to allow diffusion of CHI in and out of the film (zone I) (b) Film grows according to the exponential mechanism where CHI diffuses out of the film to double its size (c) Film becomes thick enough and cannot dispense the entire over-saturated CHI reservoir in the allotted time and CHI becomes trapped within the matrix (zone II emerges) (d) Diffusion zone (zone I) will always become saturated with CHI. CHI down to a certain depth from the solution interface will escape to complex with HA to become new bilayer(s) and expand zone I. The part of zone I that is deeper in the film matrix will retain its free CHI and become part of zone II. Therefore, the thickness of zone I will remain constant while zone II grows.

interface and remains permeable to diffusing PE, and eventually Domain II (restructuring zone) which lies between Domains I and III and is constantly in a state of re-organization to a denser film structure making it impermeable to diffusing PE^[82,87,116,125]. As a diffusing PE can only permeate so far in a finite amount of time, the film begins to grow linearly^[116]. The presence and dense structure of Domain II helps to enforce linear growth. Porcel *et al* studied this idea with two other exponentially growing film systems; HA/PLL and PGA/PAH^[82,116]. Low molecular weight PLL (20,000 and 55,000) was able to diffuse through the entire film structure regardless of the PLL molecular weight used to build the film, while high molecular weight PLL(360,000) was restricted to a diffusion zone of approximately 4 μ m in all film types (HA held constant at 400,000)^[82]. While these results complicate the current hypothesized model, the factors influencing the exponential to linear transition are still not fully understood and investigation is on-going. Porcel *et al* hypothesized that diffusion may still be an active process in the linear growth regime however the complexes free PLL forms with HA during the next deposition cycle may be unstable and only a fraction will remain associated with the film at the solution interface^[82].

The molecular weight of CHI used is within the same range as the high molecular weight PLL used in the discussed study and is expected to have more limitations with diffusing into a film matrix. CHI also is a relatively stiff, extended molecule (persistence length of 6-12nm) which also will contribute to its diffusion behavior due to steric constraints^[79]. The diffusion profile seen in the high molecular weight model studied by Porcel *et al* was constant for up to a week

lending support to the hypothesis that a population of PE can remain sequestered within a film^[82]. The effects of drying the film were not investigated in this film system. It is possible that the drying process is aiding the effect of this process by forcing the film to adopt a dense structure. Depending on the speed of restructuring, the film may not have time (in solution) to re-establish the preferred hydrated morphology. This has been a concern of more than one author studying the exponential to linear transition; however it was ruled out by Porcel *et al* who saw no changes in growth rate, mechanism, and film thickness^[116]. The films used were constructed by spray method rather than dipping and could be the result of the deposition procedure. Other procedure-dependent trends have been noted with regard to film growth^[82]. It is also possible that the linearly-built films are only stable as long as conditions permit an abundance of CHI within the film matrix. It is possible that the films will lose mass if left in a buffered solution as a new equilibrium becomes established.

CHI/DNA film growth

The presence of DNA has been confirmed in both SA and RO-containing films by other methods (Sections 2.3.2 and 2.3.3), however the actual mechanism of growth (linear versus exponential) was unknown. A preliminary study of CHI/RO growth on a five CHI/HA bilayer base using the original growth conditions is shown in Figure 2-25. The presence of RO DNA can be confirmed by the clear peak at 260nm; however the mechanism of growth could be linear or exponential. A study of more bilayers was required to determine this. The water

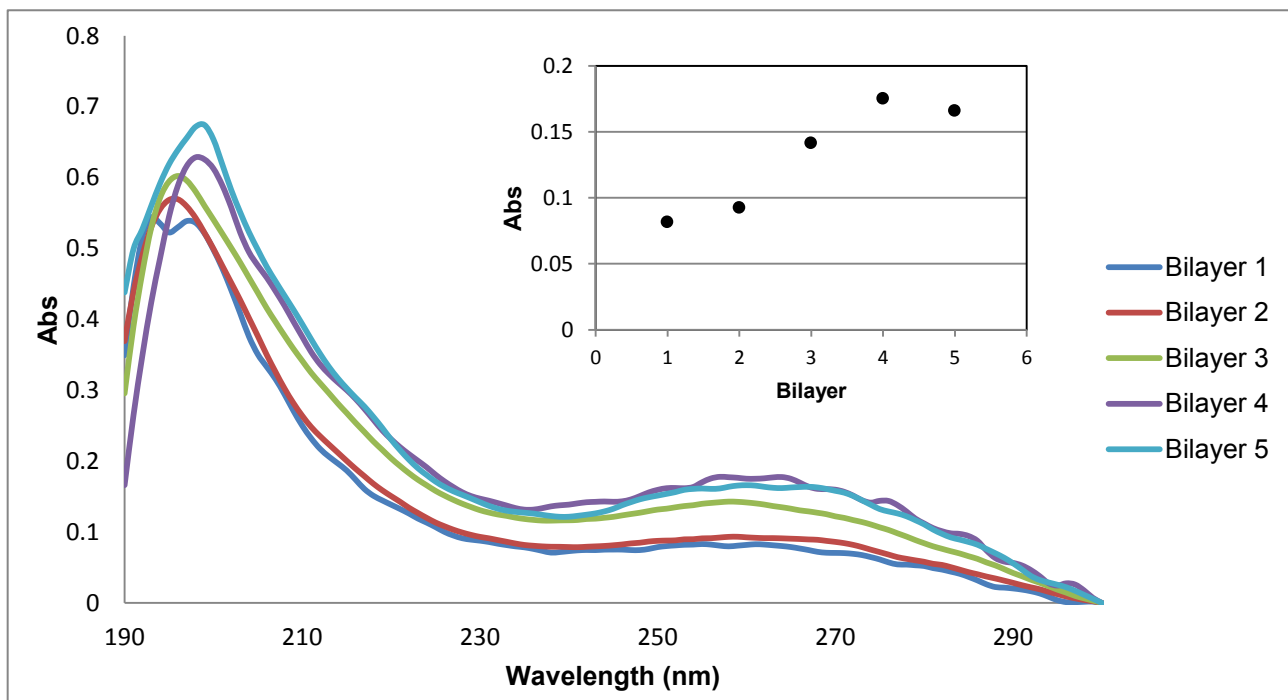


Figure 2-25: UV-Vis spectrophotometry analysis monitoring the growth of CHI/RO bilayers on a base of 5 CHI/HA bilayers by measuring the absorbance of RO DNA at 260nm. Concentration of all PEs used was 2mg/mL. All data is normalized to 300nm. Films were rinsed briefly with dH₂O before each analysis.

rinse for this study was performed using a spray bottle and therefore volume was not controlled. To ensure the trends observed were not due to rinse-volume errors, additional studies were conducted where rinse volume and times were held constant. In addition to this, PE concentrations of 1mg/mL were also investigated as it is the concentration normally used when building films.

The growth of CHI/SA bilayers on a ten CHI/HA bilayer base ([PE]=1mg/mL) was briefly investigated by UV-Vis with the thought that the DNA layers would grow in the exact same environment as when films are constructed for other purposes. These films proved to be too thick for analysis by UV-Vis (See Appendix). While peaks at 253nm can be seen, the scattering effects were

too large to get a true absorbance value. Therefore, this experiment was abandoned after depositing three bilayers.

The deposition of SA in films was explored two ways; the first by depositing CHI/SA bilayers on a five CHI/HA bilayers base (henceforth 5-CHI/HA-CHI/SA films), and the second by depositing CHI/SA bilayers alone (henceforth CHI/SA films) on a quartz substrate. PE concentrations of 1 and 2mg/mL were investigated and all films were built by the original method. A maximum of ten bilayers (total) were deposited. Final rinses in water were performed for 10s in 10mL of deionized water which was changed every use. At PE concentrations of 1mg/mL only CHI/SA films showed a peak at 253nm (Figures 2-26 & 2-27). Despite this, absorbance values were quite low with large error which complicates the determination of a growth trend. The 5-CHI/HA-CHI/SA films did not show a growth trend (Figure 2-26). It is clear from Figure 2-27 that the deposition of DNA is very low and therefore, the DNA peak in the 5-CHI/HA-CHI/SA films may be masked by the baseline absorbance of the CHI/HA base. At 2mg/mL SA deposition decreased even further and was not detectable in either film scenario (Figures 2-28 & 2-29). Absorbance was low enough for the CHI/SA film that the data was not normalized. In general, the absorbance between 230-310nm is lower in the 2mg/mL the 5-CHI/HA-CHI/SA films than in the 1mg/mL film (Figures 2-26 & 2-28). This could suggest that there is a masked DNA peak contributing to the absorbance in that region and further investigation using more sensitive techniques is worthwhile in the 1mg/mL films.

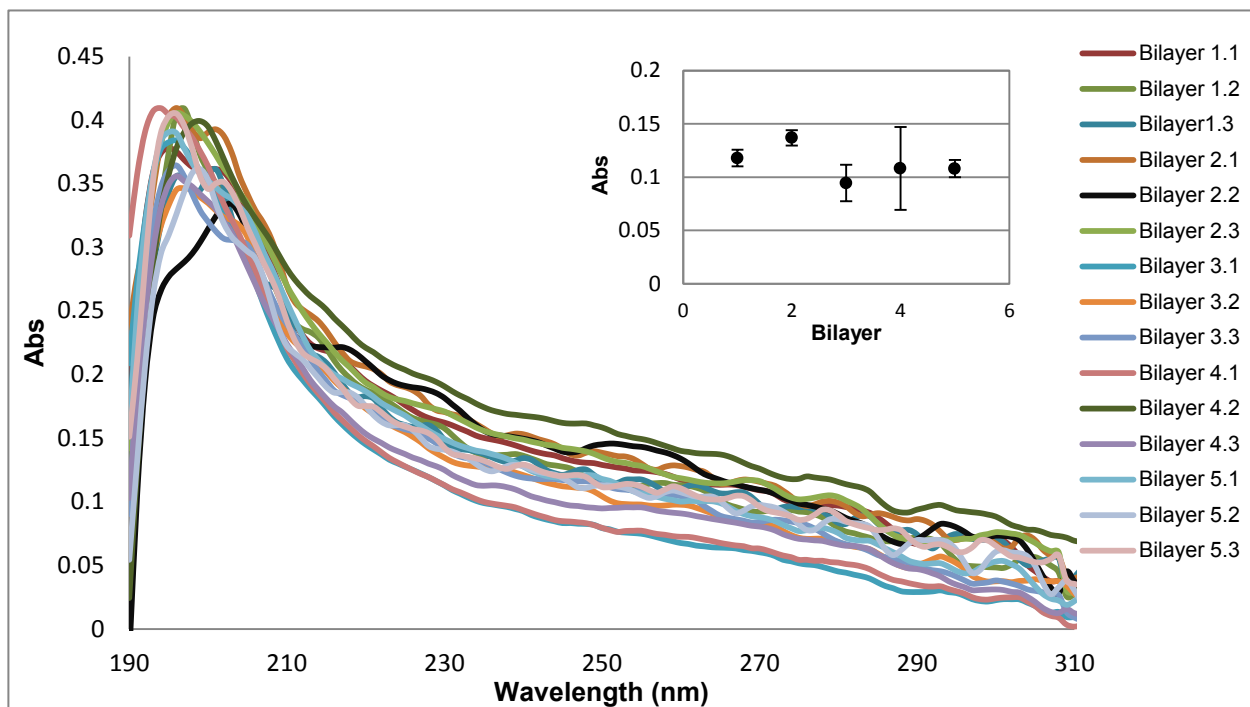


Figure 2-26: UV-Vis spectrophotometry analysis monitoring the growth of CHI/SA bilayers on a base of 5 CHI/HA bilayers by measuring the absorbance of SA DNA at 253nm. Films were grown according to the original method using PE concentrations of 1mg/mL. Three trials were done for each bilayer to account for minor compositional differences. All data is normalized to 350nm. Water rinse was for 5s. Inset: Plot of average absorbance (N=3) at 253nm depicting the growth of the CHI/SA bilayers. Error bars represent standard deviation.

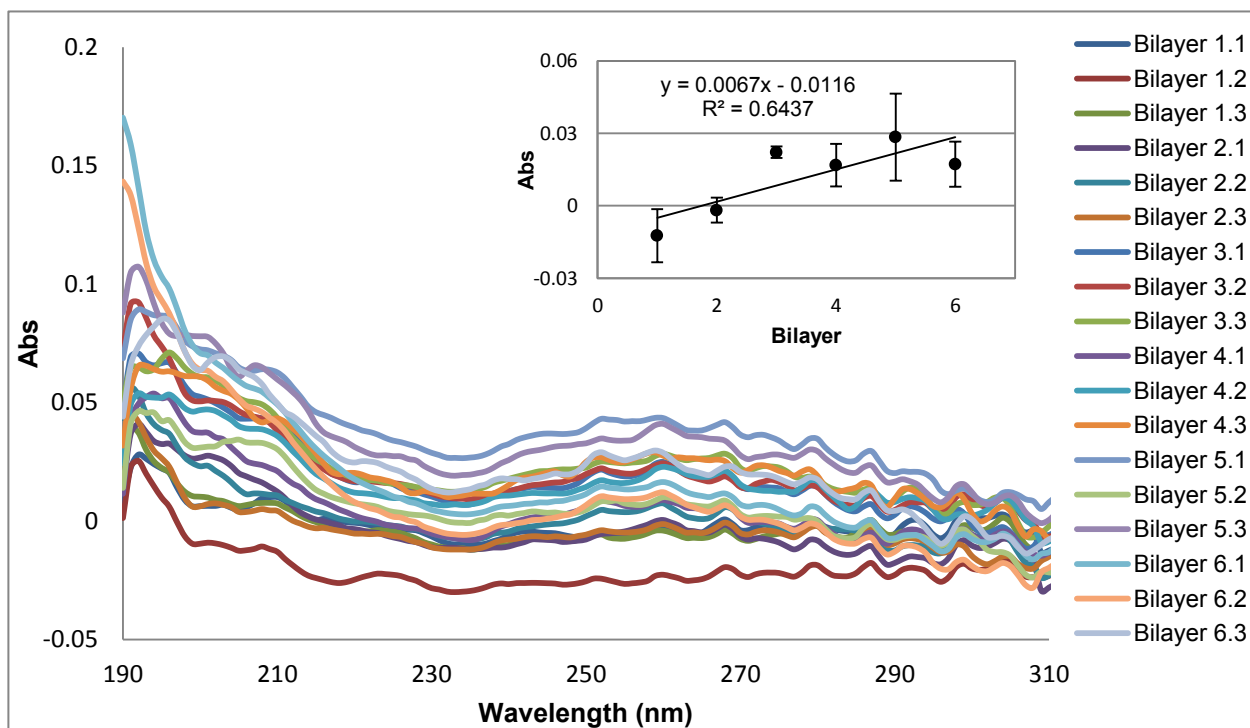


Figure 2-27: UV-Vis spectrophotometry analysis monitoring the growth of CHI/SA bilayers on a quartz substrate by measuring the absorbance of SA DNA at 253nm. Films were grown according to the original method using PE concentrations of 1mg/mL. Three trials were done for each bilayer to account for minor compositional differences. All data is normalized to 350nm. Water rinse was for 5s. Inset: Plot of average absorbance (N=3) at 253nm depicting the growth of the CHI/SA bilayers. Error bars represent standard deviation.

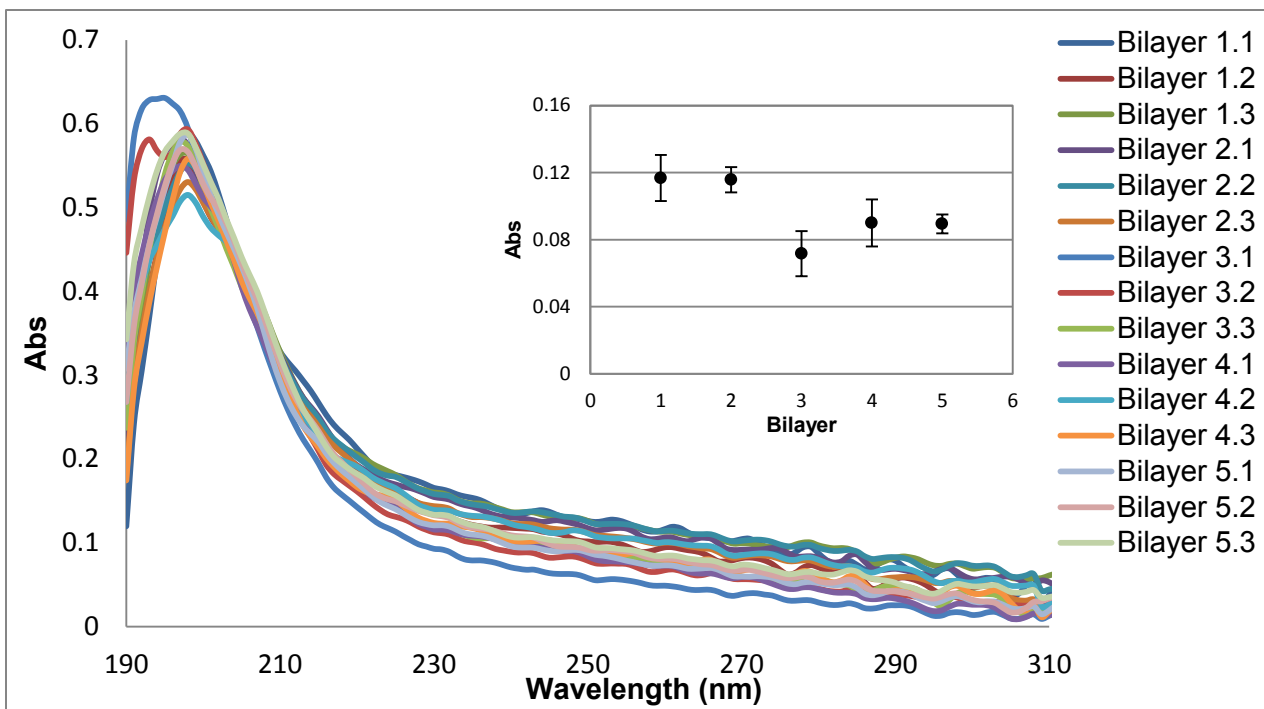


Figure 2-28: UV-Vis spectrophotometry analysis monitoring the growth of CHI/SA bilayers on a base of 5 CHI/HA bilayers by measuring the absorbance of SA DNA at 253nm. Films were grown according to the original method using PE concentrations of 2mg/mL. Three trials were done for each bilayer to account for minor compositional differences. All data is normalized to 350nm. Water rinse was for 5s. Inset: Plot of average absorbance (N=3) at 253nm depicting the growth of the CHI/SA bilayers. Error bars represent standard deviation.

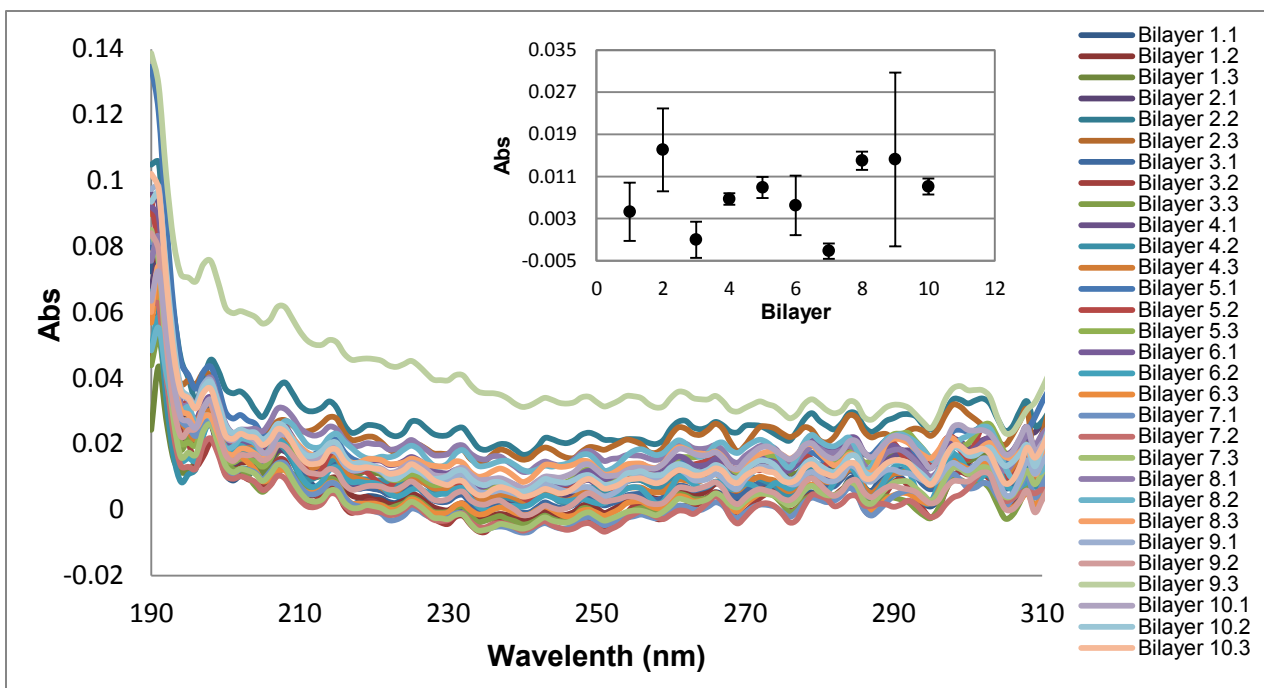


Figure 2-29: UV-Vis spectrophotometry analysis monitoring the growth of CHI/SA bilayers on a quartz substrate by measuring the absorbance of SA DNA at 253nm. Films were grown according to the original method using PE concentrations of 2mg/mL. Three trials were done for each bilayer to account for minor compositional differences. Water rinse was for 5s. Inset: Plot of average absorbance (N=3) at 253nm depicting the growth of the CHI/SA bilayers. Error bars represent standard deviation.

This experiment was repeated with RO DNA to investigate the equality of deposition between the two DNA types. The same trends that were seen in the SA films were also seen in the RO films (Figures 2-30 to 2-33). Only the CHI/RO film deposited with a PE concentration of 1 mg/mL showed a definite peak at 260nm (Figure 2-31). A linear growth trend was seen in this sample, however the absorbance values were extremely low with large errors, and therefore this observation should be confirmed with another method. As with the SA films, the 2mg/mL films had no detectable growth (Figures 2-32 & 2-33).

In both SA and RO films, the samples prepared with 2mg/mL PE solutions had worse deposition even though the preliminary study showed considerable deposition of RO DNA. Again, rinsing conditions seem to be the cause of this difference. In the later experiments, the water rinse procedure was changed from a brief rinse with water to a timed dip (10s) in a constant volume of deionized water (10mL) that was changed with every use. CHI/DNA complexes may become very unstable in the low ionic strength and pH conditions that water imposes on the system leading to the dissociation of CHI/DNA complexes from the film or even partial film disassembly. Low ionic strength has already been shown to negatively impact film growth in several film systems by reducing the material deposited per bilayer^[75,79,84]. Therefore, the water rinse may cause the films to become unstable and fall apart. However, this still does not explain the difference between the two concentrations of PE. Theoretically, a higher concentration of CHI should lead to a higher incremental change per bilayer; however the higher concentration has instead lead to the complete

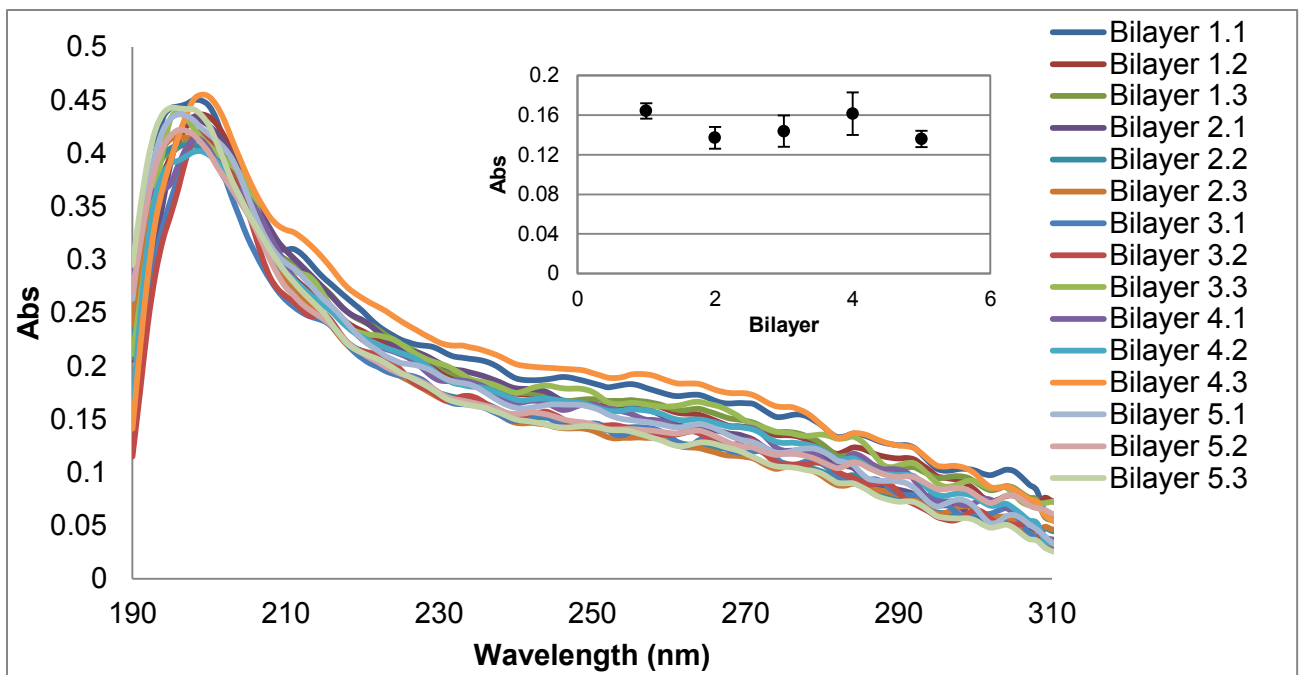


Figure 2-30: UV-Vis spectrophotometry analysis monitoring the growth of CHI/RO bilayers on a base of 5 CHI/HA bilayers by measuring the absorbance of RO DNA at 260nm. Films were grown according to the original method using PE concentrations of 1mg/mL. Three trials were done for each bilayer to account for minor compositional differences. All data is normalized to 350nm. Water rinse was for 5s. Inset: Plot of average absorbance (N=3) at 260nm depicting the growth of the CHI/RO bilayers. Error bars represent standard deviation.

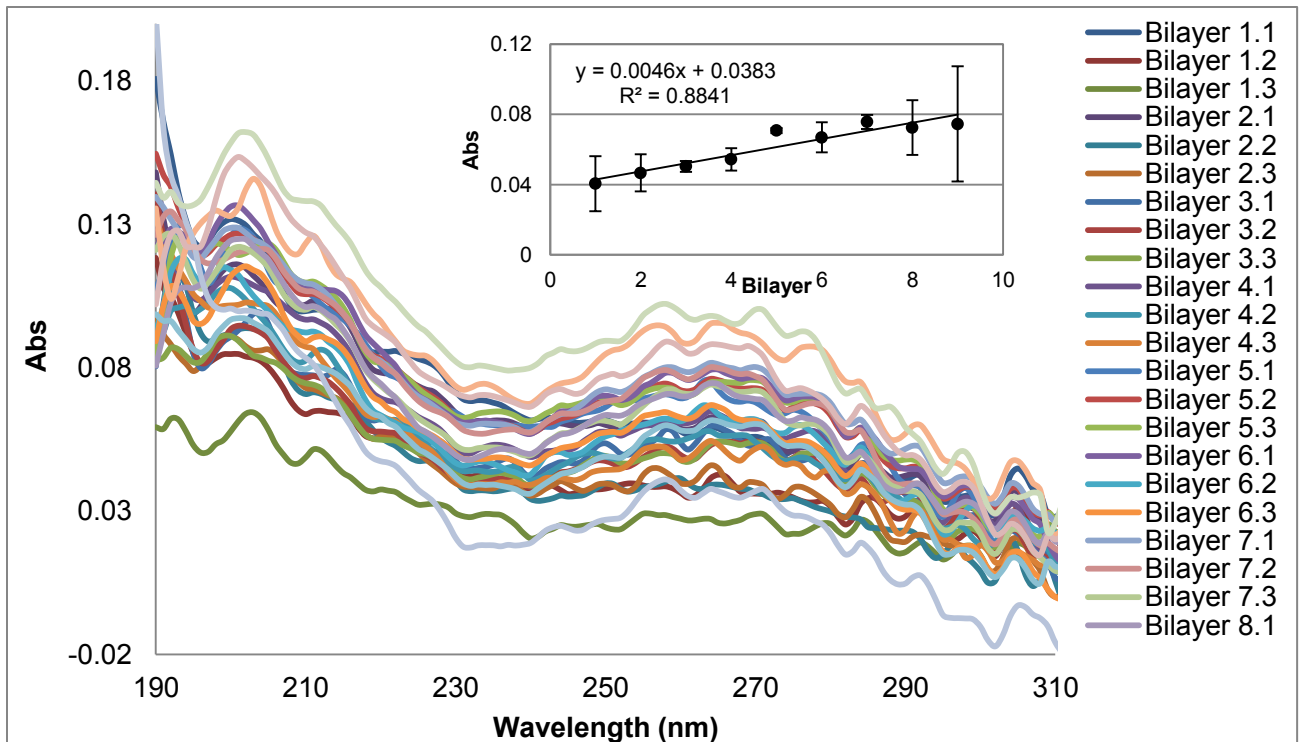


Figure 2-31: UV-Vis spectrophotometry analysis monitoring the growth of CHI/RO bilayers on a quartz substrate by measuring the absorbance of RO DNA at 260nm. Films were grown according to the original method using PE concentrations of 1mg/mL. Three trials were done for each bilayer to account for minor compositional differences. All data is normalized to 350nm. Water rinse was for 5s. Inset: Plot of average absorbance (N=3) at 260nm depicting the growth of the CHI/RO bilayers. Error bars represent standard deviation.

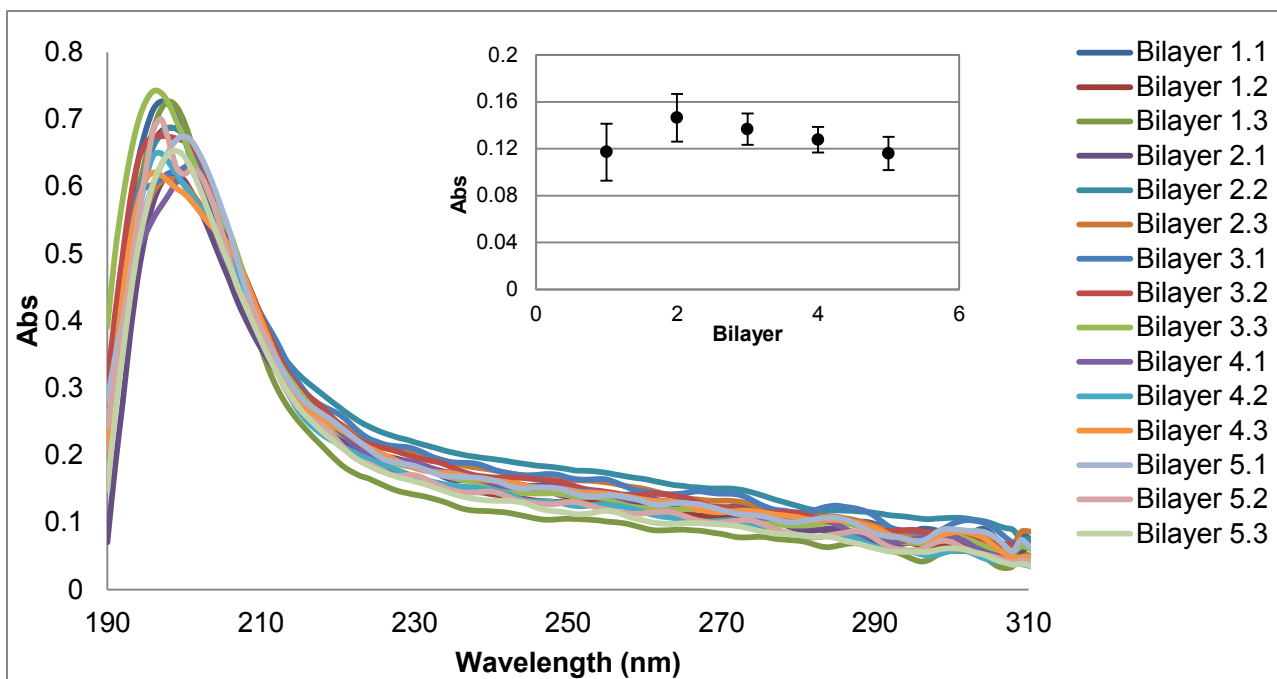


Figure 2-32: UV-Vis spectrophotometry analysis monitoring the growth of CHI/RO bilayers on a base of 5 CHI/HA bilayers by measuring the absorbance of RO DNA at 260nm. Films were grown according to the original method using PE concentrations of 2mg/mL. Three trials were done for each bilayer to account for minor compositional differences. All data is normalized to 350nm. Water rinse was for 5s. Inset: Plot of average absorbance (N=3) at 260nm depicting the growth of the CHI/RO bilayers. Error bars represent standard deviation.

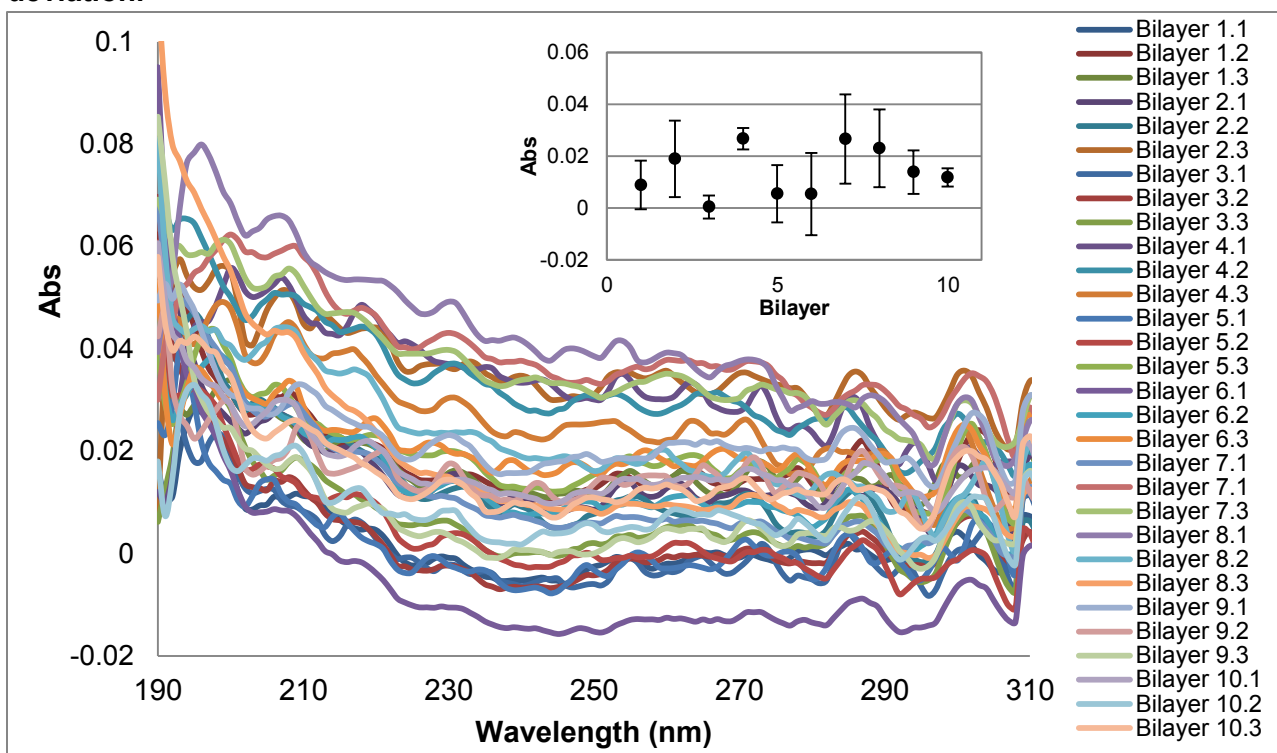


Figure 2-33: UV-Vis spectrophotometry analysis monitoring the growth of CHI/RO bilayers on a quartz substrate by measuring the absorbance of RO DNA at 260nm. Films were grown according to the original method using PE concentrations of 2mg/mL. Three trials were done for each bilayer to account for minor compositional differences. All data is normalized to 350nm. Water rinse was for 5s. Inset: Plot of average absorbance (N=3) at 260nm depicting the growth of the CHI/RO bilayers. Error bars represent standard deviation.

reduction of growth altogether. In general, DNA complexes very well with CHI, however the stability of these complexes varies with pH^[127]. DNA is highly charged due to its phosphate-backbone whereas the charge of CHI is quite variable depending on pH. CHI has a pKa of ≈ 6 whereas the pH of deionized water can range from 7 to 5.8 depending on its exposure to air^[128]. This could lead to the deprotonation of the CHI population and therefore a loss of its positive charge. DNA will remain negative through this change in pH. In a study of CHI-DNA complexes, Strand *et al* found that the complexes began to dissociate as the pH of the system was raised (pH=6.5) leading to an eventual complete and rapid dissociation (pH=7.4)^[127]. This dissociation was attributed to the decrease in the CHI charge density and it was concluded that CHI binding affinity for DNA was heavily affected by the number of charges available for interaction. Therefore, in the water rinse, the charge density of the CHI will decrease due to the increase in pH, making the CHI/DNA film unstable. The DNA cannot act like the HA as a structural component due to its small size (9,225Da and 8,940Da for SA and RO respectively) so the structural integrity of the CHI/DNA film matrix may be less robust. Concentration may result in a change of film behavior in that thinner layers (1mg/mL) may behave more like thin films and less like hydrogels (2mg/mL) as the thicker layers behave. This could mean in the case of thinner layers that the CHI/DNA complexes are more closely associated (more charge-charge matching) or have more opportunities for secondary interactions such as hydrogen bonds. Previous studies have shown that altering the ability of PE multilayers to hydrogen bond with water can alter the way it grows^[129].

Increasing hydrogen bonds resulted in linear growth while decreasing hydrogen bonds resulted in exponential growth in a PSS/PDDA film^[129]. Multilayer films based solely on hydrogen bonds have been documented and the nature of the interactions within the film can be changed rapidly from electrostatic to hydrogen bond by varying the pH of the system^[75]. These films generally require high salt concentrations and tend to show reduced growth under low ionic strength. In the thicker films, loss of CHI charge and increasing repulsion among the DNA may overwhelm secondary interactions such as H-bonds, especially if the two species are loosely associated with each other or with other complexes. A stronger H-bonding network may be found within the thinner multilayers which can compensate with the brief loss of electrostatic interactions between the CHI and the DNA. This is further supported by the fact a clear DNA peak can be found in both 1mg/mL films that does not appear to grow (Figures 2-27 & 2-30). Additional growth may result in CHI layers that are too thick causing the network to fail. CHI polymers readily form intra- and inter-molecular hydrogen bonds with other CHI molecules. With thicker CHI layers, the CHI polymers will form a network of hydrogen bonds with other CHI molecules rather than with the DNA, forming unstable complexes that do not remain attached to the film. Therefore, the surface does not have sufficient positive charge for DNA complexation in the next deposition cycle. As the rinsing procedure is more intense in the modified method films, this method was never tested. UV-Vis has been successful for other groups in studying the growth of different films systems; however often the rinse procedure is not discussed in detail other than it was

performed^[71,78,130,131,132]. Overall, additional studies are required with more sensitive equipment that removes the need for additional rinses to minimize the impact on film growth.

These studies failed to shed light on whether there is an inherent depositional bias towards the RO sequence over the SA sequence or if this is a result of target interaction (as seen in Section 2.3.3). Unfortunately, few studies had investigated the growth mechanism of LBL films containing ssDNA from the perspective of its role as a structural component. A few have looked into the growth mechanism of films containing dsDNA sources; however the mechanisms are mixed depending on the paired polycation. Linear growth has been observed in dsDNA films made with PAH^[133], poly(ethylenimine, polyarginine^[134], and poly(dimethyldiallylammonium chloride)^[131], and exponential when paired with poly(L-lysine) (PLL)^[71] and CHI^[135]. A single study performed with ssDNA (produced through denaturing complementary DNA strands) and CHI suggests a linear growth pattern, however deposition conditions were quite different from what was used in this study and it was not discussed in great detail^[135]. Additionally, the DNA source used was from salmon testes with a length of 2000bp. This size range is common with DNA films. This is much larger than the 29 nucleotide sequences employed in these studies. Even so, the build-up of CHI/ssDNA bilayers was slow, with UV-Vis absorbance values under 0.2 after the deposition of 6 bilayers^[135]. The effect of extreme differences in molecular weight on film growth has mixed results. Large differences have been reported to cause a loss of polyelectrolyte from the surface of the multilayer when

exposed to the oppositely charged species^[136]. Alternatively, extreme changes in PE molecular weight were shown to have no impact on the growth of films constructed by dipping method^[82]. However, this was a study on the linear growth regime of films experiencing exponential-to-linear film growth transitions and therefore films far more established than 10 bilayers were being used. The small size of the DNA suggests that it may be more amenable to diffusion in the film however; an accurate prediction system for growth behavior has not been developed for LBL systems. Having more than one diffusible species is possible. PLL/PGA films are one example where both species are diffusible with no impact on film growth but the thickness of each bilayer depends on contact time rather than establishing equilibrium in solution^[74]. ToF-SIMS analysis of the films used in this study suggests that ssDNA is a diffusible species; distinct layers could not be seen and the entrance of DNA and PE-characteristic secondary ions in the sputter profiles were temporally very similar (See Figure 2-5). However, as discussed previously, films composed of one or more diffusible species does not guarantee exponential-like growth. Further investigation into the behavior of small ssDNA in a film environment may shed light on some of these questions.

2.4. Conclusions

Using the SB aptamer, these studies confirmed that an aptamer can function within CHI/HA films. Rinsing conditions proved to have a large effect on film growth, DNA distribution, and aptamer-dye interaction. Increasing the rinse time and volume was found to transition film growth from linear to a more

exponential-like growth. Short rinsing times yielded linearly growing films with “hotspots” of aptamer-dye interaction that is significantly higher than films built with the RO control sequence. Longer rinsing times result in films with a more exponential-like growth, however the increase in nonspecific interaction between the dye and film matrix masks any aptamer-dye binding that may be occurring. In general, more sensitive techniques that do not possess the technical constraints of UV-Vis spectrophotometry (such as QCM-D) are required to further examine the impact of rinse time and volume of film growth. This would also allow a better investigation into the manner of growth in CHI/DNA films whose growth fell below the detection limits of the UV-Vis. The next chapter will discuss the ability of the film matrix to protect embedded aptamer from degradation.

2.5. Acknowledgements

Thank you to Amy Won for producing the AFM images of the CHI/HA films and all help with their analysis. Also, thanks to Dimitre Karpuzov at the Alberta Centre for Surface Engineering and Science at the University of Alberta for his aid in the ToF-SIMS analysis.

Chapter 3. Development of an assay assessing film protective properties against nuclease-mediated degradation

3.1. Introduction

3.1.1. Limitations of *in vivo* aptamer nanotechnology

Due to their characteristic binding abilities, aptamers have shown great promise in applications such as controlled delivery^[137], therapeutics^[138], biosensors^[139], and detection platforms^[140]. However, native aptamers (DNA and RNA) are extremely susceptible to degradation by nucleases (exo- and endo-) especially in *in vivo* applications such as therapeutics. Because of this, aptamers generally have a half-life of minutes in a biological system due to nuclease degradation and fast clearance^[141]. In order for aptamers to be effective in *in vivo* applications they must be able to retain a high level of affinity and specificity for their target, have sufficient resistance to degradation and be able to persist within in the environment employed. Therefore, sensitivity to nuclease-mediated degradation imposes high-impact complications and must be resolved before large-scale use of aptamers can be employed in real-life applications. Several strategies have been developed to help confer nuclease resistance to aptamers. Partial and complete chemical modification of aptamer monomers have been shown to improve lifetime, usually in combination with modifications preventing premature clearance from biological systems, and can increase aptamer

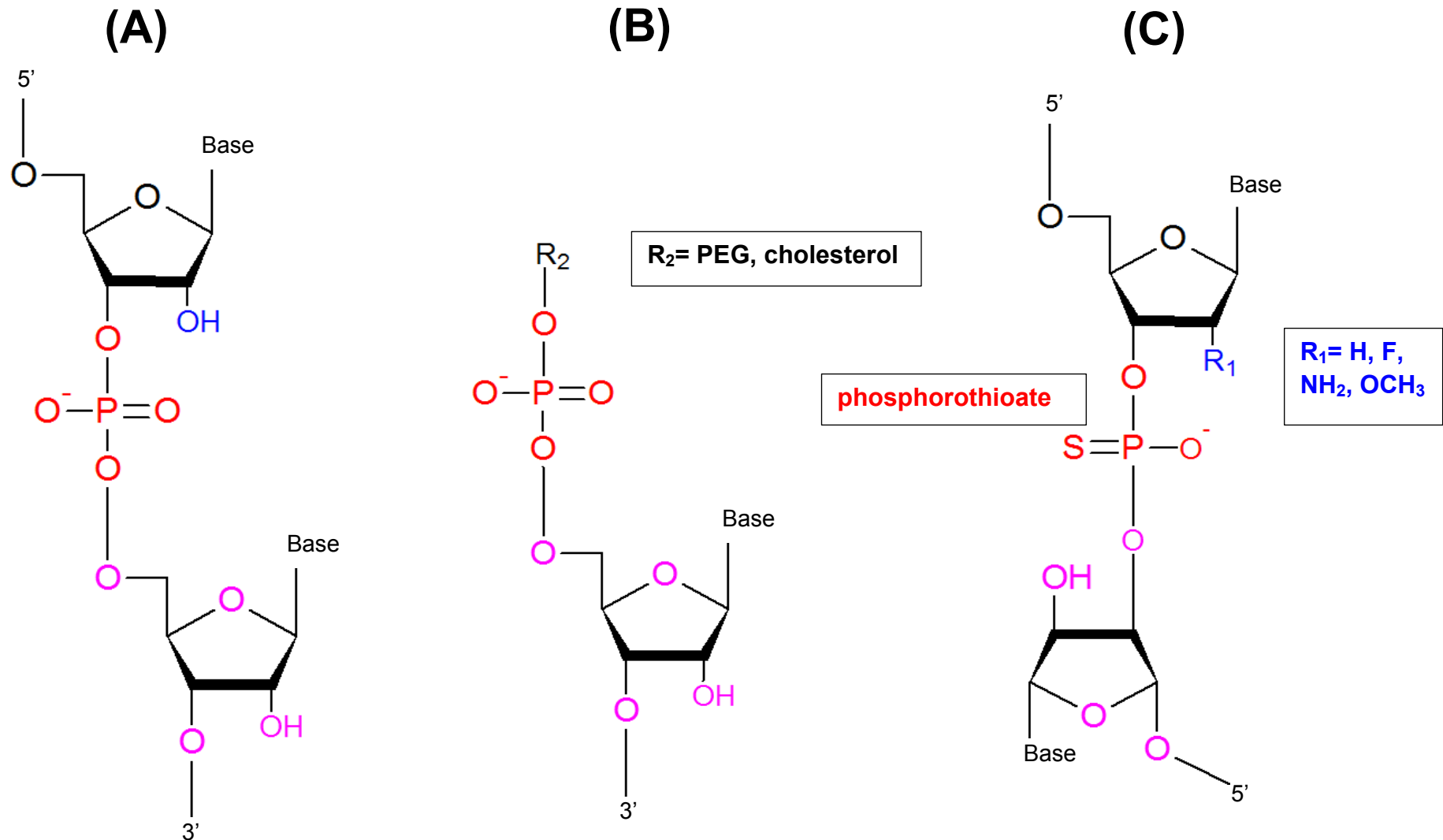


Figure 3-1: Common aptamer modifications to improve lifetime and resistance against nuclease-mediated degradation. (A) Native RNA structure (note: modifications can also be applied to DNA). (B) Modification to 5'-end of sequence with molecules like polyethylene glycol (PEG) and cholesterol prevent premature clearance from biological systems. (C) Modification of the 2'-(O)H with groups such as fluorine (F), amino (NH_2) or O-methyl (OCH_3) aids against nuclease degradation (blue). Phosphorothioate linkages (where a non-bridging O is replaced by an S) dramatically increases nuclease resistance (red). Capping of the 3'-end by inversion of the 3'-nucleoside to create 5'—5' oligonucleotides is highly effective at preventing degradation due to 3'-exonucleases (pink). (Adapted from [141])

lifetime to days^[141]. Figure 3-1 shows some commonly employed modifications which have large impacts on aptamer (DNA and RNA) lifetime. Substituting the 2'-OH group to an amino group in RNA aptamers for human neutrophil elastase resulted in a lifetime increase from five minutes to over an hour in biological fluids^[142]. Spiegelmers (which use the enantiomers of natural nucleotides) are also highly effective at conferring nuclease resistance by exploiting the stereospecificity of nucleases^[141]. Similarly, LNA (locked nucleic acids) which circularize the monomers between C(2') and C(4') have been shown to increase nuclease resistance in the Tenascin C RNA aptamer^[143,144]. This was attributed to the decrease in flexibility of the single-stranded sequence regions susceptible to nuclease attack^[144]. However, when RNA monomers within the binding regions were converted to LNA a complete loss of target interaction resulted^[144]. Similar limitations have been noted in the chemical modifications listed above. LNA-type moieties are very effective against exonucleases but not against endonucleases^[145]. Spiegelmers are difficult to generate which imposes restrictions on the target^[141]. Chemical modifications have been known to decrease the binding affinity of the original aptamer. Despite the increase in nuclease resistance, modification of RNA aptamers for Rous sarcoma virus with 2'-fluoro-2'-deoxyuridine and 2'-fluoro-2'-deoxycytidine resulted in a 7-10X decrease in virus counteraction^[146]. Chemical modifications make selection of aptamers more complicated as the polymerases used in amplification steps may not accept the modifications^[147]. Modification post-selection may have a detrimental effect on aptamer affinity^[145]. In general, chemical modification

remains the more expensive alternative. As of 2010, RNA phosphoramidites cost \$3/g (US) when unmodified, but this increases to \$20/g when modified with a 2'-fluoro, 2'-ribo, or 2'-O-methyl^[141]. Therefore, methods able to employ native DNA and RNA aptamers and protect against nuclease degradation may provide a more effective solution.

The use of aptamers in combination with nanotechnology may provide that alternative, and studies have indicated that nanomaterials are capable of shielding aptamers from nucleases. Integrating aptamers with nanomaterials such as carbon nanotubes, quantum dots, metal or silica nanoparticles, or encapsulating them in silica polymers and gels have been shown to increase aptamer lifetime^[148]. Single-wall carbon nanotubes within the cytoplasm were able to protect the DNA coating it just by association^[149]. When bound, the aptamers were able to maintain a conformation unfamiliar to the nuclease, preventing recognition. A similar effect was seen with DNA conjugated to gold nanoparticles^[150]. In this study, it was theorized that an ionic gradient was created due to the high loading density of DNA onto the nanoparticles, resulting heightened salt concentrations near the nanoparticles that inhibited nuclease activity. Encapsulation of DNA within nanostructures has also been explored. Encapsulation of RNA aptamers in virus-like particles were able to protect against nuclease-mediated degradation by acting as a selectively permeable entity^[151]. Thus, nucleases were unable to access the interior of the capsule. In another study, aptamer-based probes embedded in polyacrylamide nanoparticles showed increased resistance over the course of 90 minutes to DNase I

compared to naked DNA which was degraded within an hour^[145]. Furthermore, the nanoparticles allowed diffusion of small molecules (in this cases adenine nucleotides) enabling the aptamer probes to maintain their function while embedded. This study is a promising example of an aptamer-functionalized nanomaterial that has fulfilled both requirements necessary for success as discussed previously.

As there are few examples of aptamer-functionalized LBL films, very little work investigating the protective capabilities of the film matrix have been performed. LBL films using strong PE pairs are well known to allow the diffusion of small molecules (i.e. dyes, ions) through the film matrix but reject those of larger molecular weight (i.e. nucleases, sugars)^[152]. Diffusion through PEMs can be tuned by altering film properties such as layer thickness, porosity, PE pairs, and film structure, and different compounds show a wide variety of diffusion behavior depending on their own nature (i.e. charge and size)^[153]. In fact, diffusion behavior through PEMs becomes more complex with films that begin to employ weak PEs. Aravind *et al* demonstrated that pH and salt concentration also played a role in diffusion through CHI/PSS films due to their effects on film thickness and charge of proteins diffusing through the matrix^[154]. Diffusion of bovine serum albumin (BSA) through 9 bilayer CHI/PSS films prepared at pH 2.1 was less hindered (72.9% rejection) than films prepared at pH 1.7 (94.7% rejection) in 0.1M NaCl. However, when conducted in a salt-less environment, diffusion of BSA through the pH 1.7 films was nearly unhindered (13% rejection). Ovalbumin and lysozyme showed completely different diffusion behavior than

BSA and were more affected by charge and pH than the presence of salt or number of bilayers. Film systems prone to diffusion of at least one polyelectrolyte tend to be more amenable to diffusion of larger compounds. CHI/HA films have been shown to allow diffusion of myoglobin (>15% rejection, MW 17,000) but not BSA (97% rejection, MW 67,000) and therefore the molecular cut-off weight exists somewhere in between^[155]. However, preventing diffusion does not seem to be essential in conferring a protective effect towards enzyme-mediated degradation of a species of interest. Electrostatic interaction with an oppositely charged species alone has proved to confer additional resistance to DNA against nucleases. Albumin/perfluorocarbon microbubbles coated with PAH were demonstrated to bind plasmid DNA and prevent its degradation by rhDNase I despite the DNA existing in the outermost layer of the structure^[156]. Multilayers of plasmid DNA and lipid-DNA complexes constructed by LBL chemistry showed similar protective effects; plasmid DNA could be detected after an hour of exposure to DNase I whereas naked plasmid DNA was completely degraded after 20 minutes^[157]. Complexes of PLL and plasmid DNA were resistant against degradation in 90% serum (v/v) for up to 2 hours^[158]. CHI-calf thymus DNA complexes using different CHI molecular weights were extremely effective at protecting DNA against DNase II^[159]. CHIs of low (>5,000), medium (5,000-10,000), and high (>10,000) molecular weights showed 99.9 ± 0.1 , 99.1 ± 1.5 , and $98.5 \pm 2.0\%$ inhibition of DNase II-mediated degradation respectively^[159]. From this, it is expected that encapsulation of aptamer

sequences within a film matrix will confer a protective effect against nucleases, extending the functional lifetime of the ssDNA.

3.1.2. Chapter Objectives

For real-world applications, aptamers must be able to function within a given matrix with high affinity and selectivity and withstand the surrounding environmental challenges such as nuclease-mediated degradation. Aptamers for SB dye are able retain their binding function when sequestered within a CHI/HA matrix (as discussed in Chapter 2). This chapter will investigate the protective ability of the CHI/HA matrix against degradation of DNA within the film by Nuclease S₁. Nuclease S₁ was chosen as it is optimally active at pH 4.5. As the CHI/HA/6-FAM SA films are constructed at pH 4.5, this avoids a dramatic pH change and therefore minimizes the impact on film structure as pH has been demonstrated to effect film stability and morphology.

3.2. Experimental

3.2.1. Materials

Nuclease S₁ from *Aspergillus oryzae* (in 30mM sodium acetate, 50mM NaCl, 1mM ZnCl₂, 50% (w/v) glycerol), chitosanase from *Streptomyces griseus* (lyophilized powder), and hyaluronidase from bovine testes (lyophilized powder)

were purchased from Sigma Aldrich. All reagents were used as received. All materials used for films are outlined in Section 2.2.1.

3.2.2. Optimization of ssDNA degradation by Nuclease S₁

SA DNA was synthesized with a 5' fluorescein modifier (6-FAM) by standard phosphoramidite chemistry and purified by PAGE as described in Section 2.2.2. Protocol was adapted from the Fisher Scientific Nuclease Assay protocol^[160]. Digestion reactions contained ~1ug of 6-FAM SA, 6μL of 5X Nuclease S₁ Reaction buffer (200mM sodium acetate, pH 4.5, 1.5M NaCl, 10mM ZnSO₄), 0.1-20U of Nuclease S₁ and dH₂O to 30μl. The reactions were incubated for varying time intervals (0-60min) at 37°C or RT. Reactions were stopped by the addition of 2μL of 0.5M ethylenediaminetetraacetic acid (EDTA) (in dH₂O, pH 8.0) heated to 70 or 90°C and a 10 minute incubation at 70 or 90°C. Reactions were analyzed using a 12 or 19% PAGE gel as outlined in Section 2.2.2 and imaged at 302nm using the fluorescence of the 6-FAM SA DNA.

Nuclease digestion temperature. Two sets of reactions were prepared using 20U of Nuclease S₁ and incubated for 0 to 10 minutes (one minute increments) in a 37°C water bath or at RT. Reactions were stopped with the addition of 2μL of 70°C EDTA and incubating for 10 minutes in a 70°C water bath. Reactions were analyzed using a 12% PAGE gel.

Reaction deactivation temperature and gel resolution. Four sets of reactions were prepared using 10 or 1U of Nuclease S₁ and incubated for 0-5

minutes (one minute increments) at RT. Reactions were stopped with the addition of 2 μ L of 70 or 90°C EDTA and incubating for 10 minutes in a 70 or 90°C water bath. The 70°C and 90°C reactions were analyzed using a 12 and 19% PAGE gel respectively.

Enzyme amount. Two sets of reactions were prepared using 0.1 and 0.01U of Nuclease S₁ and incubated for 0-5 minutes (one minute increments) at RT. Reactions were stopped with the addition of 2 μ L of 90°C EDTA and incubating for 10 minutes in a 90°C water bath. Reactions were analyzed using a 19% PAGE gel.

Reaction time. Three sets of reactions were prepared using 1, 0.5, and 0.1U of Nuclease S₁ and incubated for 0-30 minutes (five minute increments) at RT. Reactions were stopped with the addition of 2 μ L of 90°C EDTA and incubating for 10 minutes in a 90°C water bath. Reactions were analyzed using a 19% PAGE gel.

Finalization of reaction conditions. Two reactions were prepared using 1 and 0.5U of Nuclease S₁ and incubated for 60 minutes at RT. Reactions were stopped with the addition of 2 μ L of 90°C EDTA and incubating for 10 minutes in a 90°C water bath. Reactions were analyzed using a 19% PAGE gel.

From the optimizations, the final protocol was decided and adapted for films. Digestion reactions contained ~1 μ g of 6-FAM SA, 6 μ L of 5X Nuclease S₁ Reaction buffer (200mM sodium acetate, pH 4.5, 1.5M NaCl, 10mM ZnSO₄), 0.1 μ L of 0.5U Nuclease S₁ and dH₂O to 30 μ L. To cover an entire film deposited

on a slide (gridded or not), ~500 μ L of liquid is required. Therefore, the above protocol was scaled up accordingly. Reactions were stopped with the following rinse sequence: 3X with 500 μ L of 90°C EDTA, 5X with 500 μ L of 90°C 0.15 NaCl pH 4.5, and 1X with 500 μ L of 90°C dH₂O.

3.2.3. PAGE gel analysis of nuclease assay

CHI/HA/6-FAM SA films were prepared by both the original protocol as outlined in Section 2.2.3, with a few changes. To investigate the protective role of the capping layer, films were prepared both with and without the capping layer. The following films were created (where the number specifies the number of bilayers): 10 CHI/HA-5 CHI/6-FAM SA (uncapped) and 10 CHI/HA-5 CHI/6-FAM SA-1 CHI/HA (capped). A control film was also prepared with the same compositional scheme as the capped film which was not exposed to the nuclease.

The nuclease assay was performed on dry films as described in Section 3.2.2. The same process was also performed on the control film however the volume of nuclease was replaced with dH₂O. All rinses were kept and dried down by SpeedVac. In order to analyze structural integrity by PAGE gel, the embedded DNA must be released from the film matrix. To do this, two additional enzyme assays were added to degrade the CHI/HA film. To degrade the CHI, 500 μ L of a 100 μ g/mL (~0.5U/mL) solution of chitosanase prepared in 0.15M NaCl pH 5 was applied to the film and incubated for an hour in a mini-incubator.

The film was rinsed as follows: 3X with 500 μ L of 90°C NaCl pH 4.5, and 1X with 500 μ L of 90°C dH₂O. All rinses were dried down by SpeedVac immediately. Subsequently, the HA was degraded by incubating 500 μ L of a 1-2mg/mL (~500U/mL) solution of hyaluronidase prepared in 0.15M NaCl pH 5 on the film for one hour at 37°C. The film was rinsed as follows: 3X with 500 μ L of 90°C NaCl pH 4.5, and 1X with 500 μ L of 90°C dH₂O. All rinses were dried down by SpeedVac immediately. This process was repeated for the other side of the slide. This protocol was adapted from the chitosanase/hyaluronidase protocol used by Picart *et al*^[108].

The washes formed a thick gel when dried down. After re-suspending in a minimum volume, the rinses were filtered Amicon-Ultra centrifuge units (50 kDa cut off) to remove CHI and HA although this did not solve the problem. The washes were analyzed using a 12% PAGE gel as described in Section 2.2.2. The wells of the gel were altered by hand to create wells spanning three lanes to accommodate the additional volume required to get the gel formed in the rinses back into solution.

3.2.4. Fluorescence-based analysis of nuclease assay

Films were prepared by the original and modified method as outlined in Section 2.2.3, with a few changes. The following films were created (where the number specifies the number of bilayers): 10 CHI/HA-5 CHI/6-FAM SA (uncapped) and 10 CHI/HA-5 CHI/6-FAM SA-1 CHI/HA (capped). Control films were prepared without a capping layer. DNA digestion was tracked by

measuring the fluorescent intensity of 6-FAM SA DNA remaining within CHI/HA/6-FAM SA films. A preliminary study was performed as outlined by the finalized assay protocol in Section 3.2.2 however subsequent studies (gridded glass slides) had a slightly altered rinse sequence. The original rinse sequence (3X with 500 μ L of 90 $^{\circ}$ C EDTA, 5X with 500 μ L of 90 $^{\circ}$ C 0.15 NaCl pH 4.5, and 1X with 500 μ L of 90 $^{\circ}$ C dH₂O) was replaced by the following: 3X with 500 μ L of 90 $^{\circ}$ C EDTA, 5X with 500 μ L of 90 $^{\circ}$ C dH₂O. This change was implemented to reduce the volume necessary to re-suspend the gel-like substance that formed when the assay rinses were dried down. The same process was also performed on the control film however the volume of nuclease was replaced with dH₂O. Films were dried under a stream of Ar immediately after each digestion. All rinses were kept and dried down by SpeedVac.

Images were taken on dry films with an EVOS®*fl* fluorescent microscope (AMG software) using the GFP channel ($\lambda_{\text{excitation}}=470\text{nm}$, $\lambda_{\text{emission}}=525\text{nm}$). Images of each film were taken before nuclease exposure, then after each digestion for a total to two. Magnification was 10X. Mean fluorescent intensities of the images were calculated using ImageJ.

In addition to this, the rinses collected from each assay were analyzed for fluorescence using a Horiba Fluorolog Fluorescence Spectrophotometer with a SpectrAcq controller. Emission spectra ($\lambda_{\text{excitation}}=490\text{nm}$, $\lambda_{\text{emission}}=500\text{-}600\text{nm}$) were taken to account for any DNA that had escaped the films using the fluorescence of the fluorescein tag. 5X Nuclease S₁ Reaction Buffer and dH₂O mixed in the same proportions as in the assay was used as a blank.

3.3. Results and Discussion

3.3.1. Optimized protocol for digestion of ssDNA by Nuclease S₁

In order to gain useful information from the nuclease assay, the digestion level had to be optimized to be slow enough to see changes in DNA integrity, yet be complete after a certain period of time. Termination of the reaction must also be instantaneous to prevent degradation of DNA after the desired incubation period. This could be achieved by varying enzyme level, reaction temperature, reaction time, and EDTA/stop-incubation temperature. Fluorescein-labeled DNA was used to achieve lower limits of detection due to low-loading of DNA in the CHI/HA films.

Performing the digestions at 37°C and at RT seemed to have little impact on the efficiency of DNA digestion (See Figure 3-2). However, Nuclease S₁ is so potent that even the 0 minute controls show complete digestion despite the immediate addition of EDTA. It is possible that digestion appears complete due to the gel percentage used and a higher gel concentration would give higher resolution of digestion fragments. Heating the EDTA to 70°C (and the subsequent incubation at 70°C) may also be insufficient to stop the reaction.

In light of the results from the first digestion, several parameters were changed including reducing the enzyme used, increasing the deactivation temperature and investigating the resolution capabilities of a 19% gel. Reduction of the enzyme used does decrease the digestion seen in the 0 minute control; however incubation at 70°C is still inefficient at stopping the reaction (Figure 3-3).

Increasing this temperature to 90°C appeared to help stop the reaction as shown by the increasing proportion of full length DNA to digest products (Figure 3-4). Switching to a 19% gel also provided enough resolution to separate different sized digestion fragments.

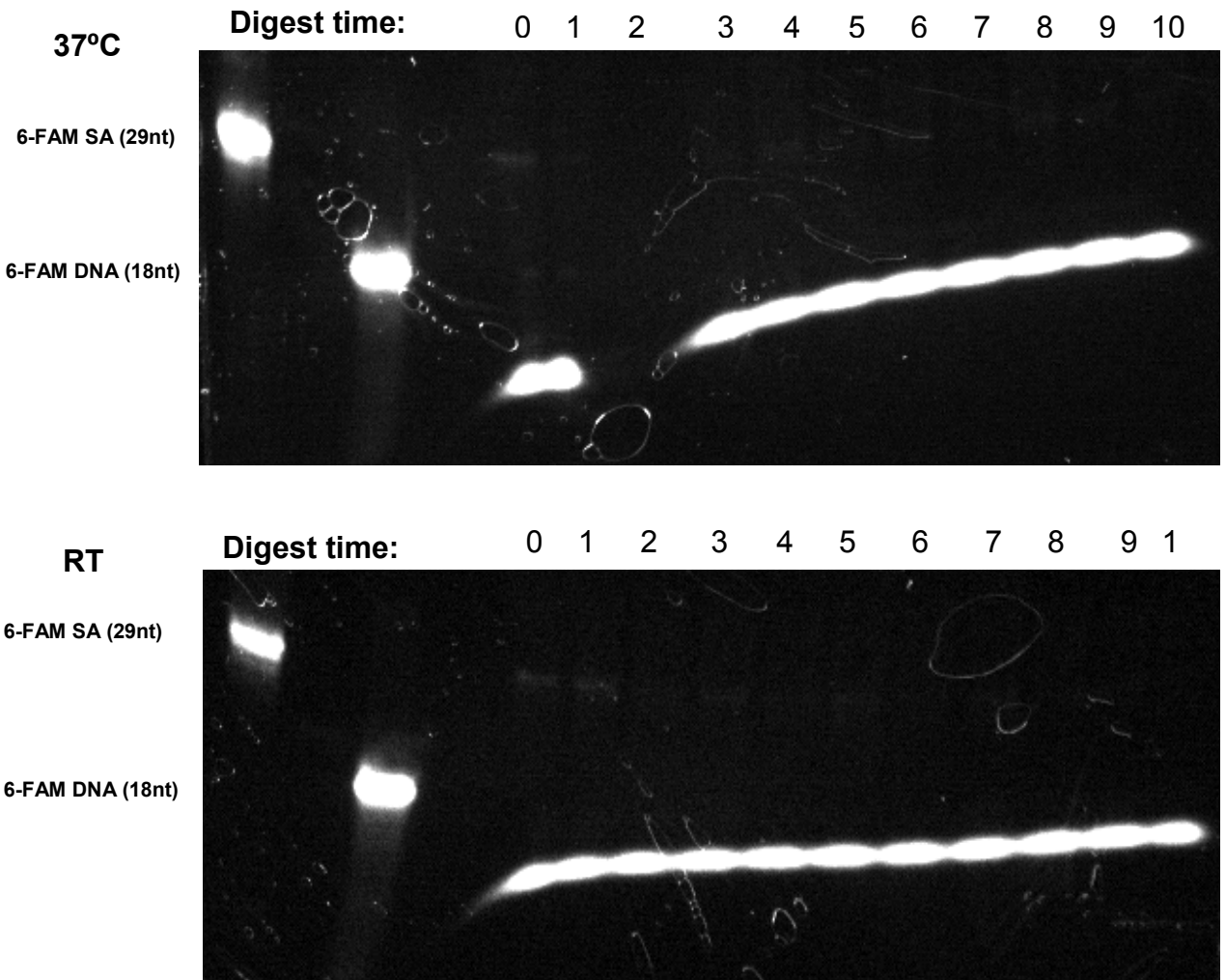


Figure 3-2: Comparison of 6-FAM SA digestion by Nuclease S₁ over varying times (0 to 10 minutes) at 37°C (top) and at RT (bottom). Samples were analyzed on a 12% PAGE gel. Reactions were stopped with the addition of 70°C EDTA and a 10 minute incubation at 70°C. Size controls consisted of undigested 6-FAM SA DNA (29nt) and an 18nt fluorescently labeled DNA sequence. Gels were imaged at 302nm by monitoring the fluorescence of fluorescein.

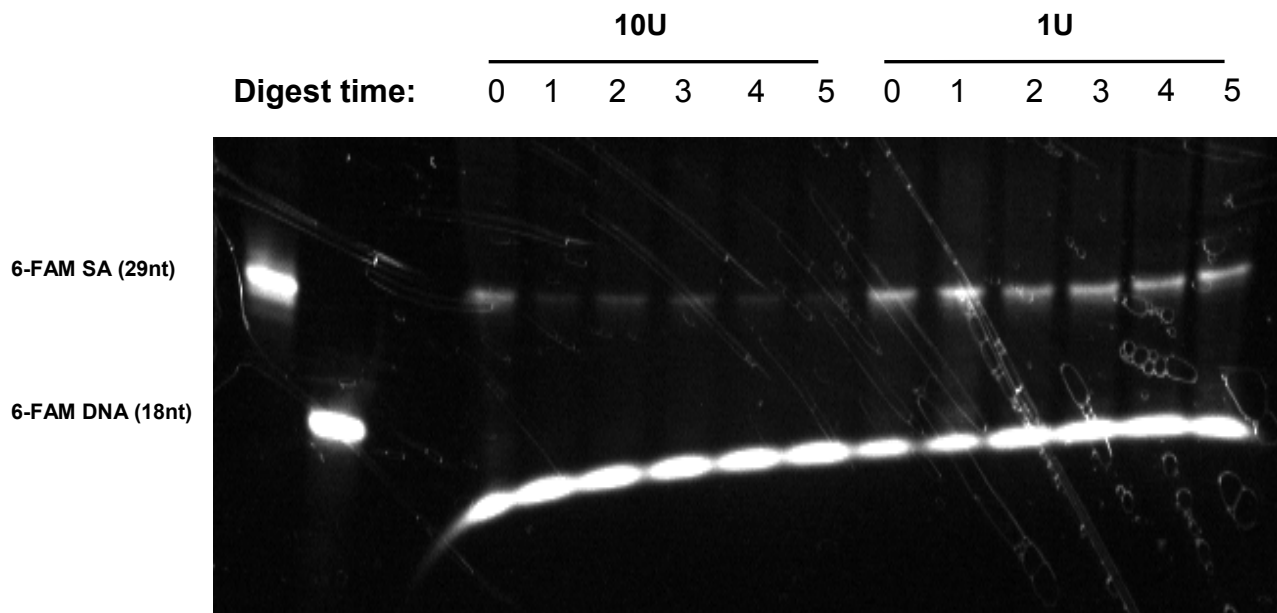


Figure 3-3: Comparison of 6-FAM SA digestion by Nuclease S_1 over varying times (0 to 5 minutes) using 10U (left) or 1U (right) of nuclease at RT. Samples were analyzed on a 12% PAGE gel using the fluorescence of fluorescein. Reactions were stopped with the addition of 70°C EDTA and a 10 minute incubation at 70°C. Size controls consisted of undigested 6-FAM SA DNA (29nt) and an 18nt fluorescently labeled DNA sequence.

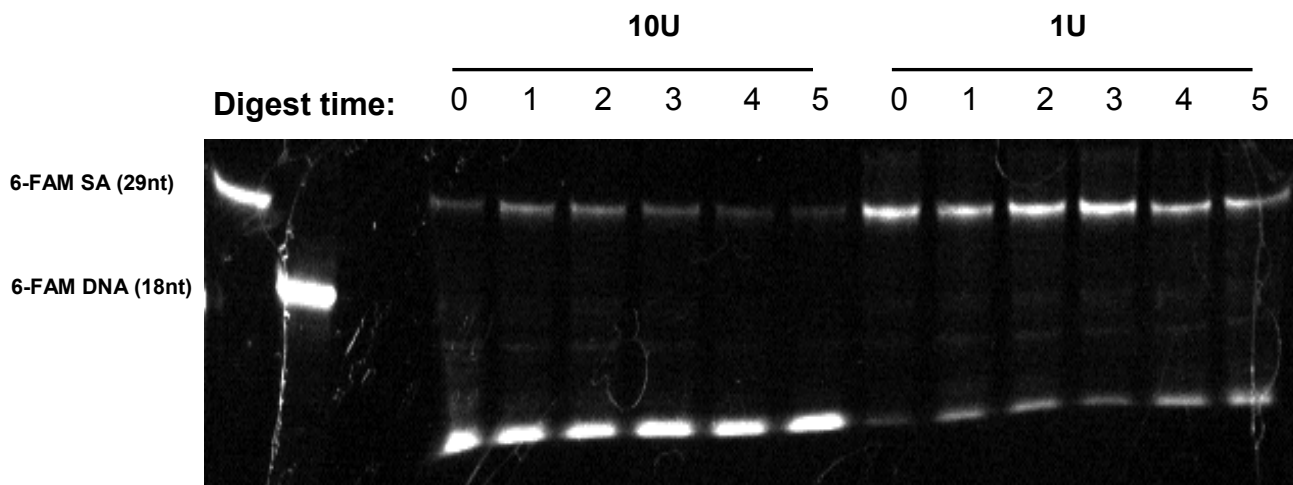


Figure 3-4: Comparison of 6-FAM SA digestion by Nuclease S_1 over varying times (0 to 5 minutes) using 10U (left) or 1U (right) of nuclease at RT. Samples were analyzed on a 19% PAGE gel using the fluorescence of fluorescein. Reactions were stopped with the addition of 90°C EDTA and a 10 minute incubation at 90°C. Size controls consisted of undigested 6-FAM SA DNA (29nt) and an 18nt fluorescently labeled DNA sequence.

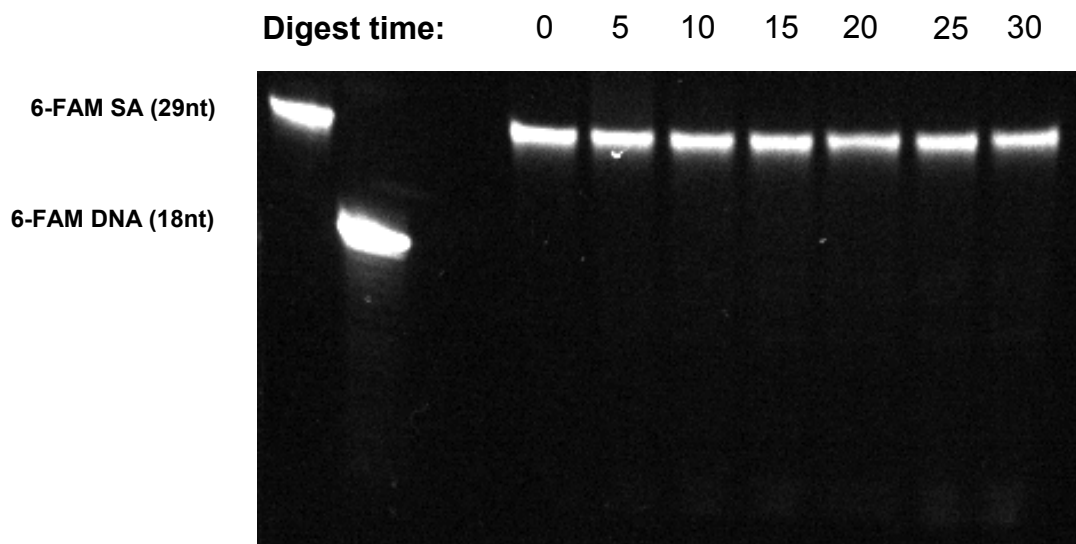


Figure 3-5: Digestion of 6-FAM SA DNA by Nuclease S_1 over varying times (0 to 30 minutes) using 0.1U of nuclease at RT. Samples were analyzed on a 19% PAGE gel using the fluorescence of fluorescein. Reactions were stopped with the addition of 90°C EDTA and a 10 minute incubation at 90°C. Size controls consisted of undigested 6-FAM SA DNA (29nt) and an 18nt fluorescently labeled DNA sequence.

The amount of enzyme was reduced further and digestion times were increased. From this, 0.1U of enzyme had the best 0 minute control, but had minimal degradation products even after 30 minutes (See Figure 3-5). This concentration was not carried onwards beyond this point. Using 1 and 0.5U of enzyme seemed to give good yields of digestion products (although 30 minutes was insufficient for complete degradation) and had minimal degradation products in the 0 minute control signifying good control over reaction termination (See Figure 3-6). Increasing the digestion time using 1 and 0.5U of enzyme resulted in near complete digestion of DNA in both samples (See Figure 3-7). From this, 0.5U of enzyme and a digestion time of an hour yielded the best results for digestion of the 6-FAM SA DNA and control over reaction termination.

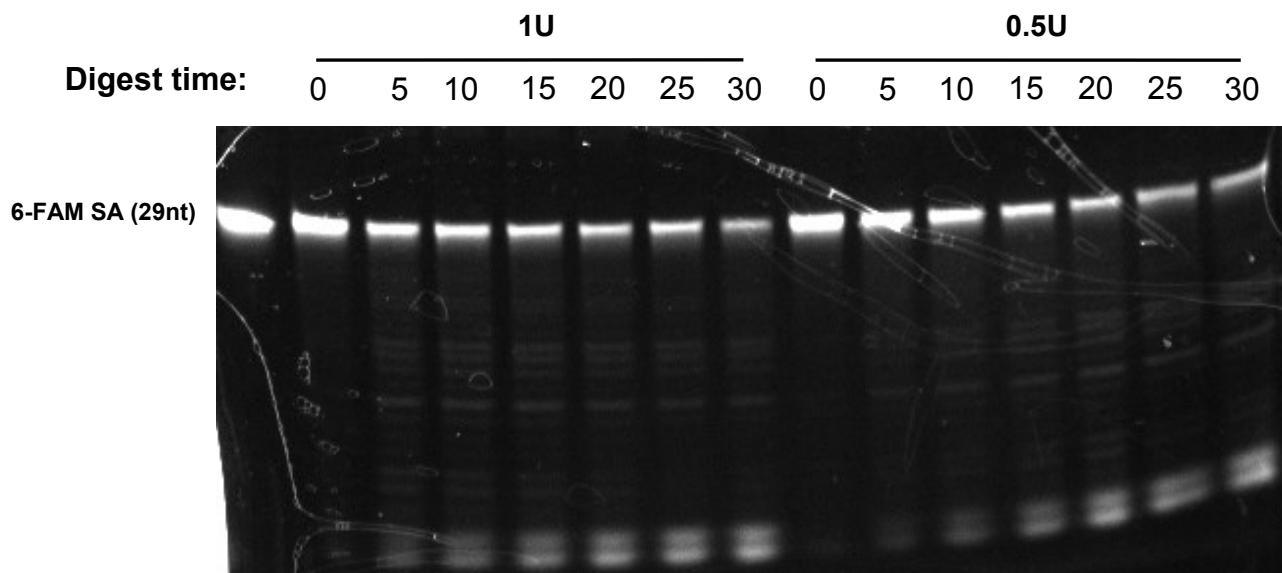


Figure 3-6: Comparison of 6-FAM SA digestion by Nuclease S_1 over varying times (0 to 30 minutes) using 1U (left) or 0.5U (right) of nuclease at RT. Samples were analyzed on a 19% PAGE gel using the fluorescence of fluorescein. Reactions were stopped with the addition of 90°C EDTA and a 10 minute incubation at 90°C. Size control consisted of undigested 6-FAM SA DNA (29nt).

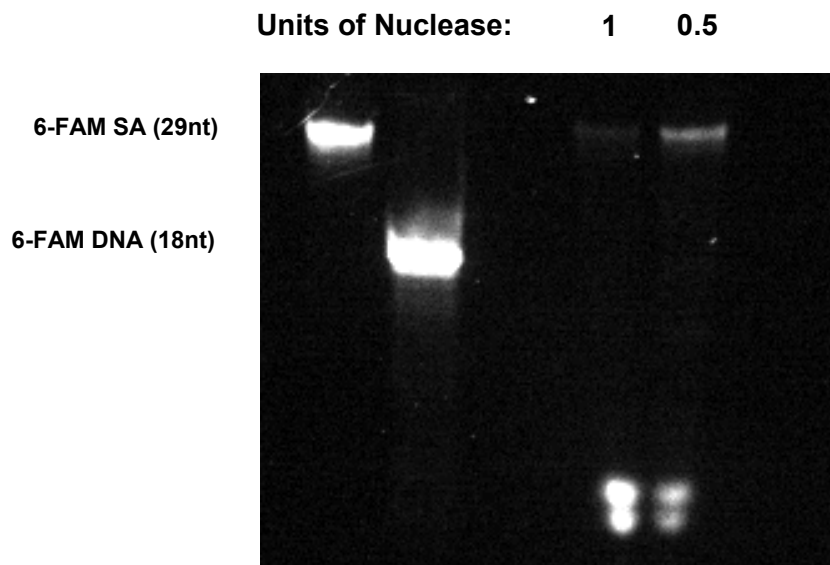


Figure 3-7: Comparison of 6-FAM SA digestion by Nuclease S_1 after 60 minutes using 1U or 0.5U of nuclease at RT. Samples were analyzed on a 19% PAGE gel using the fluorescence of fluorescein. Reactions were stopped with the addition of 90°C EDTA and a 10 minute incubation at 90°C. Size controls consisted of undigested 6-FAM SA DNA (29nt) and an 18nt fluorescently labeled DNA sequence.

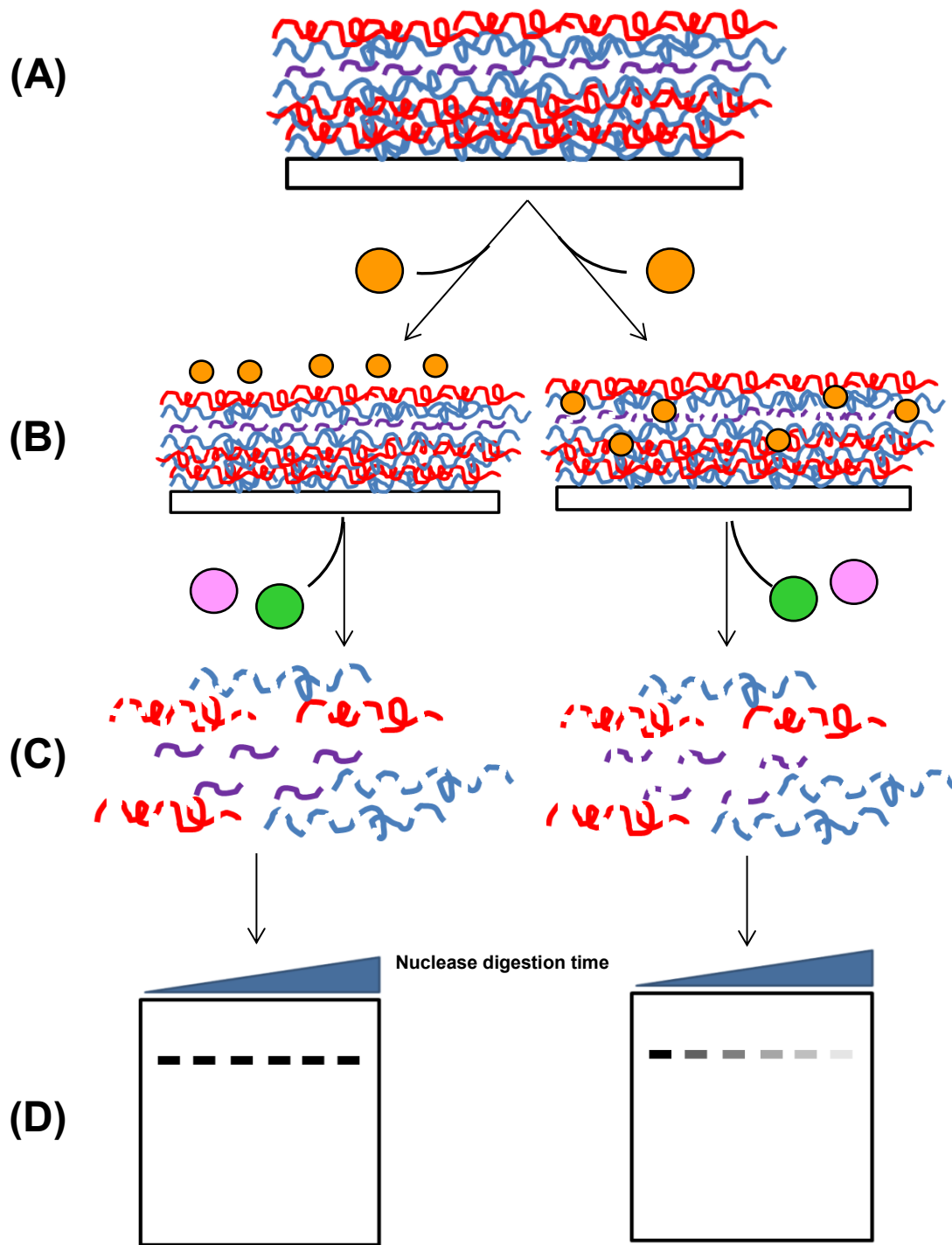


Figure 3-8: Schematic of PAGE-based nuclease assay. (A) A CHI/HA/6-FAM SA film is prepared. **(B)** Film is exposed to Nuclease S₁ (orange circles). Nuclease either permeates the film to digest the DNA (right) or does not, leaving the DNA intact (left). **(C)** Film matrix is degraded by chitosanase (green) and hyaluronidase (pink), releasing the DNA into solution. **(D)** DNA integrity is analyzed by PAGE gel for restriction fragments using the fluorescence of fluorescein.

3.3.2. Analysis of film nuclease assay by PAGE

This assay was designed to assess the protective role of LBL films against the degradation of DNA by Nuclease S₁. Looking at the extremes, subjecting the CHI/HA/6-FAM SA film to nuclease would result in one of two outcomes (Figure 3-8). In one pathway, the nuclease would not be able to enter the film to access the DNA and full length DNA would be seen upon subsequent release from the film. In the reverse scenario, the nuclease would be able to permeate the capping layer and access DNA resulting in a range of DNA degradation products. The reality is most likely a scenario in between these extreme cases; however no fluorescence was seen besides the 18nt fluorescent DNA marker upon analysis of the assay rinses (Figure 3-9).

This experiment met two major roadblocks: the low loading of DNA in the films and the tendency of the film rinses to form a gel upon drying. From the UV-Vis studies (Section 2.3.4), it is suspected that the level of DNA within the films is low. This poses a considerable challenge for analysis of this assay by gel electrophoresis which requires a substantial amount of DNA for visualization even by fluorescence (~23ng; results not shown). This is further complicated by the nature of the assay itself; by degrading the DNA, the amount of DNA in each fragment population is reduced (depending on the number of digestion fragments). By using fluorescently tagged DNA, it was hoped that the probability of detecting the DNA fragments would be improved. The second challenge was the formation of a thick gel in the rinses upon drying (See Figure 3-10). The drying process is required to reduce the volume of the sample to an appropriate

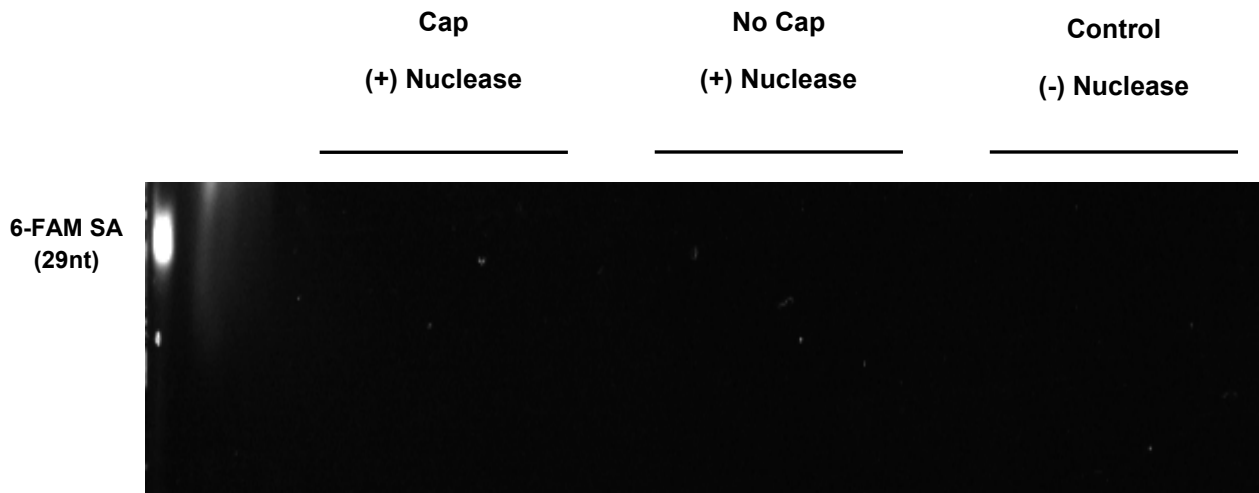


Figure 3-9: Comparison of 6-FAM SA digestion by Nuclease S₁ between films with different compositions after 60 minutes using 0.5U of nuclease at RT. Washes from the nuclease assay for each film type were analyzed on a 12% PAGE gel using the fluorescence of fluorescein. Size control consisted of undigested 6-FAM SA DNA (29nt).

amount that can be loaded into a PAGE gel. The formation of gel prevents volume reduction of the sample (and hence concentration of the DNA) to be analyzed as a larger volume is required to dissolve the sample. It also prevents the preparation of multiple samples to increase the amount of DNA analyzed in one experiment. The increased volume required to dissolve the sample poses the biggest issue as it requires a larger well (in the PAGE gel) for loading. This in turn spreads the DNA over a larger area and effectively dilutes it, contributing already present problem of low DNA levels. The need for a more sensitive technique in order to cope with the limitations of the samples is obvious.

Therefore, FM and fluorescence spectrophotometry were employed in attempt to determine the protective role of the films.



Figure 3-10: Gel formed in nuclease assay rinses upon drying down by SpeedVac before PAGE gel analysis.

3.3.3. Analysis of film nuclease assay using fluorescence

In a preliminary study, CHI/HA/6-FAM SA films with and without a capping layer were prepared by the original method on quartz slides. Images were taken in random locations where fluorescence was highest (three from the top, middle, and bottom of the slides for a total of nine). The results from this assay were promising, as the film with a capping layer retained more fluorescence (therefore more DNA) than the film without a capping layer (See Figure 3-11). However, these results are within error of each other. There are several other issues associated with this study. Images were not taken from the same locations after each digestion. A control was not performed to rule out the effects of the

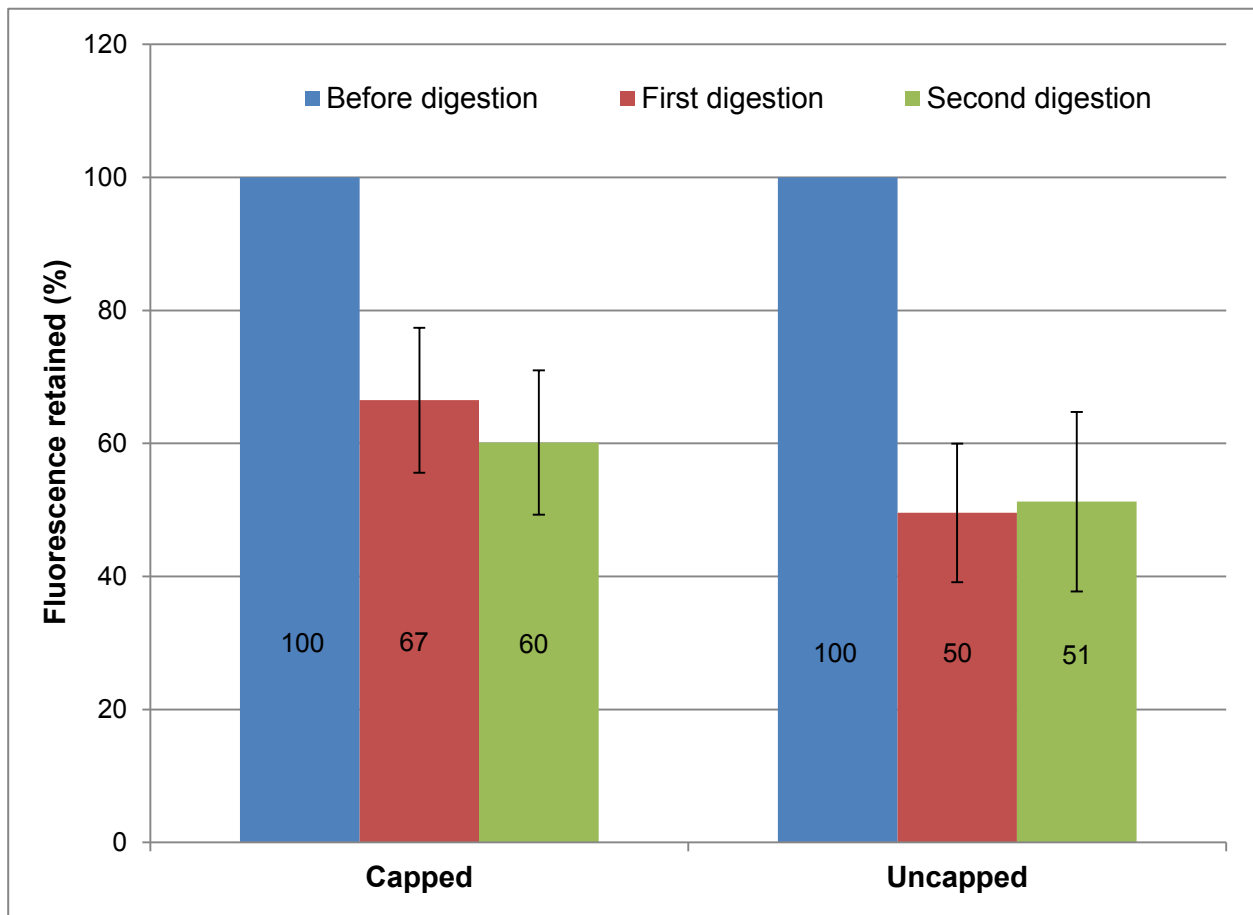


Figure 3-11: Preliminary study of the change in the average mean fluorescent intensity of CHI/HA/6-FAM SA films (N=9) with and without a capping layer after each hour-long exposure to Nuclease S₁. All films were made using the original method. Fluorescence retained was calculated as the percentage of the average mean fluorescent intensity (as calculated by ImageJ) retained from the baseline fluorescence (before nuclease exposure).

washing process. Therefore, the assay was repeated with gridded slides so the same areas on the film could be re-visited after each digestion.

CHI/HA/6-FAM SA films were prepared on gridded glass slides by the original method. Unfortunately, the logical trends seen in the preliminary study were not present, and the capped and uncapped samples gained fluorescence compared to the baseline data (Figure 3-12). Only the control showed a logical decrease in fluorescence suggesting that the washing process causes DNA to

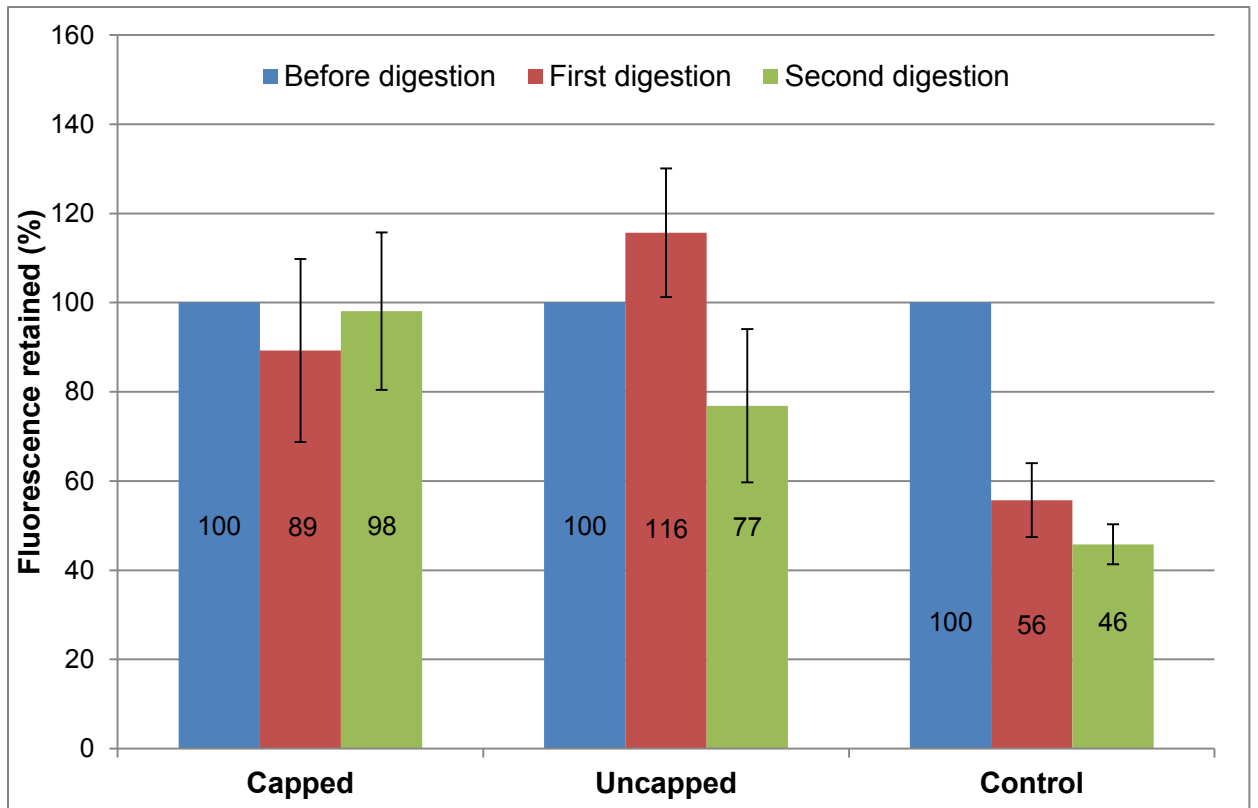


Figure 3-12: Change in the average mean fluorescent intensity of CHI/HA/6-FAM SA films (N=16) with and without a capping layer after each hour-long exposure to Nuclease S₁. Control film was uncapped and exposed to the assay process without addition of nuclease (N=8). All films were made using the original method. Fluorescence retained was calculated as the percentage of the average mean fluorescent intensity (as calculated by ImageJ) retained from the baseline fluorescence (before nuclease exposure).

be lost from the films. The increase in fluorescence in some cases suggests that the DNA (fragments or full sequences) are able to move within the films taking them between quadrants on the slide. The fluorescence spectrophotometry measurements on the assay rinses were not able to clarify the trends present (Figure 3-13). The washes from the capped and uncapped samples showed similar DNA loss, while the control had the highest DNA loss. This is most likely due to the higher loading of DNA in the control sample as compared to the other films (data not shown). The same trends were seen in samples prepared by the

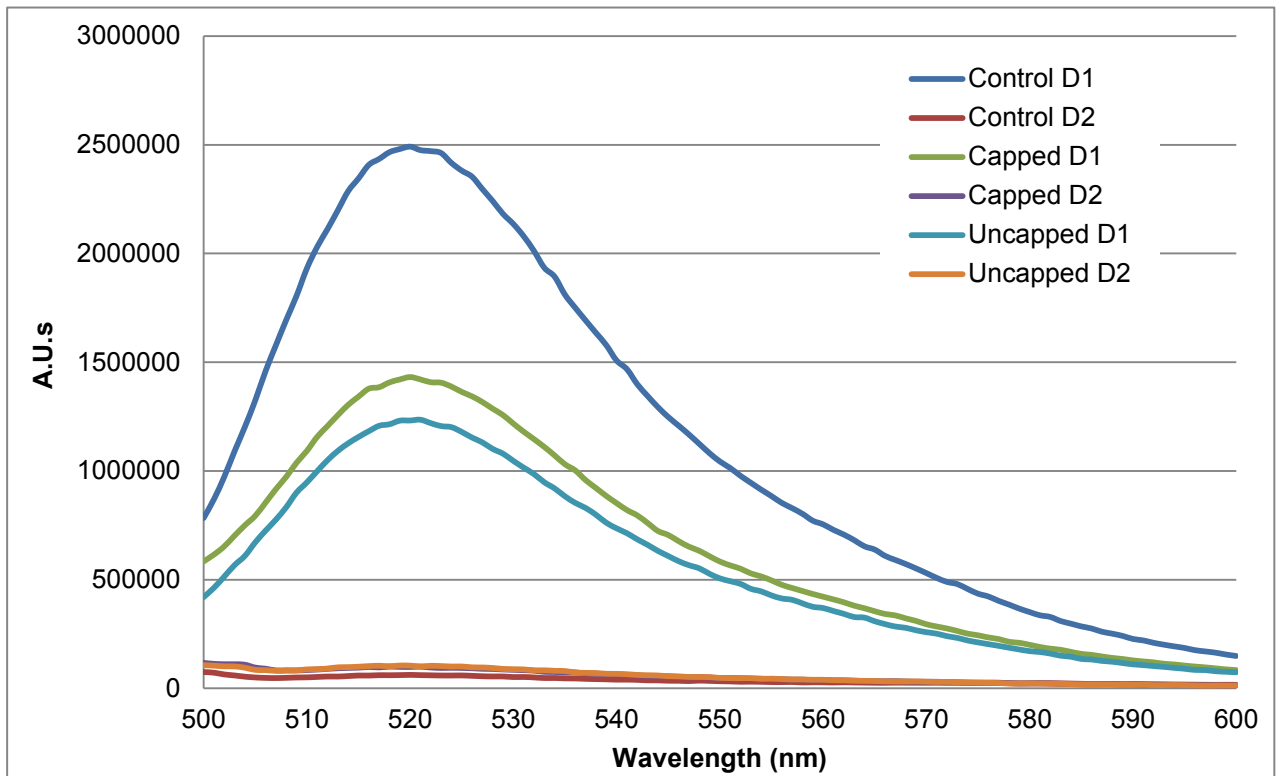


Figure 3-13: Fluorescence measurements of film washes after each nuclease digestion of CHI/HA/6-FAM SA films with and without a capping layer analyzing for DNA loss from the films. Control film was uncapped and exposed to the assay process without addition of nuclease. All films were made using the original method. The presence of DNA was monitored by the fluorescence of fluorescein (Ex=490nm).

modified method as well (Figures 3-14 & 3-15). The results show an even stronger argument supporting the movement of DNA through the films. The control film shows complete retention of all DNA after the first digestion (Figure 3-14), yet the fluorescence of the washes from the first digestion show DNA was lost (Figure 3-15).

There are several limitations to this adaptation of the nuclease assay that put it at a disadvantage to its gel-based counterpart. While the limit of detection is indeed lower, it is not as accurate as individual digest fragments cannot be

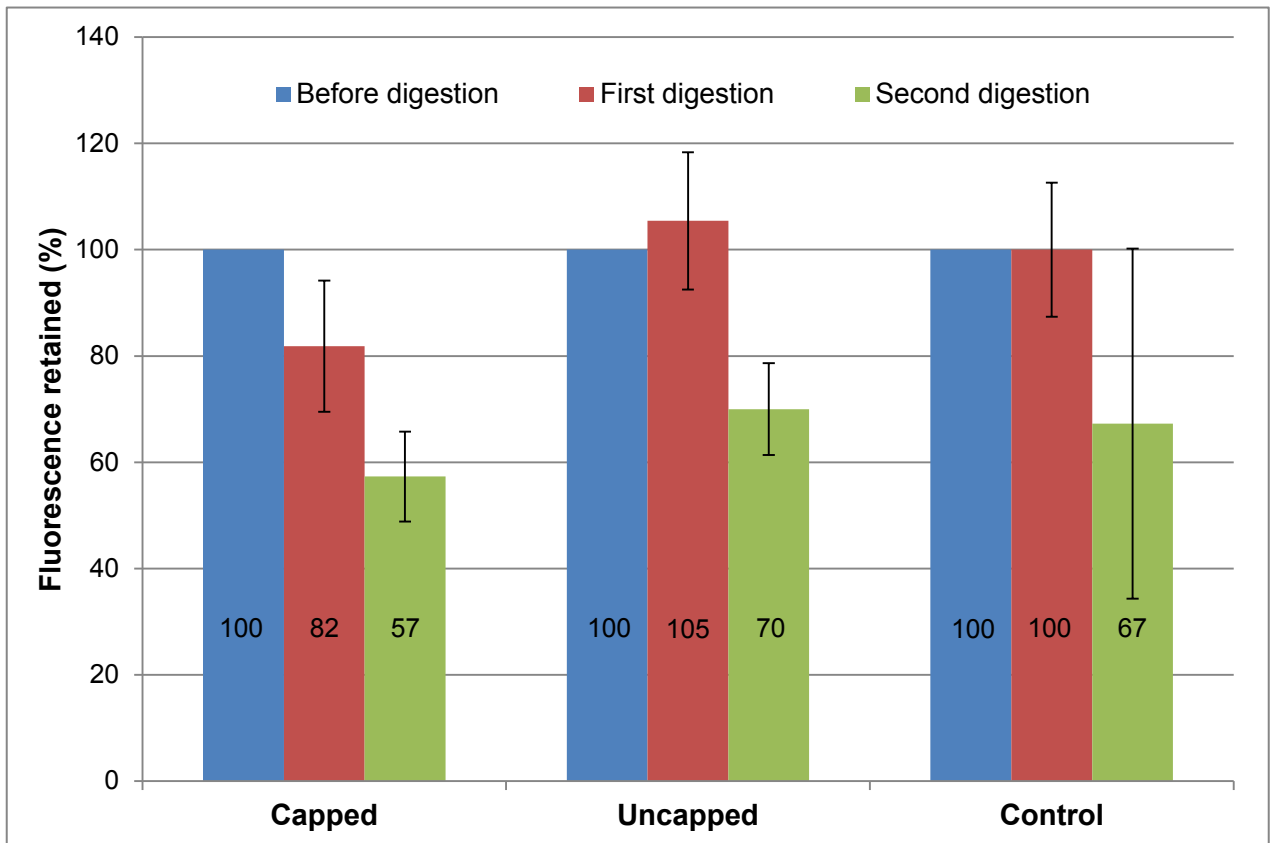


Figure 3-14: Change in the average mean fluorescent intensity of CHI/HA/6-FAM SA films (N=8) with and without a capping layer after each hour-long exposure to Nuclease S₁. Control film was uncapped and exposed to the assay process without addition of nuclease (N=8). All films were made using the modified method. Fluorescence retained was calculated as the percentage of the average mean fluorescent intensity (as calculated by ImageJ) retained from the baseline fluorescence (before nuclease exposure).

discerned. It is still possible for digest fragments to remain within the film (due to electrostatic interactions) and contribute their own fluorescence yielding an artificially higher signal. However before these aspects can be addressed, solutions resolving the compatibility issues between film stability and the conditions of the nuclease assay must be established. The results obtained from the nuclease assay (and the resulting complications) arise from increasing ionic and thermal instability of the film and subsequent restructuring and material loss. The films are constructed in 150mM NaCl, but this is doubled to 300mM NaCl

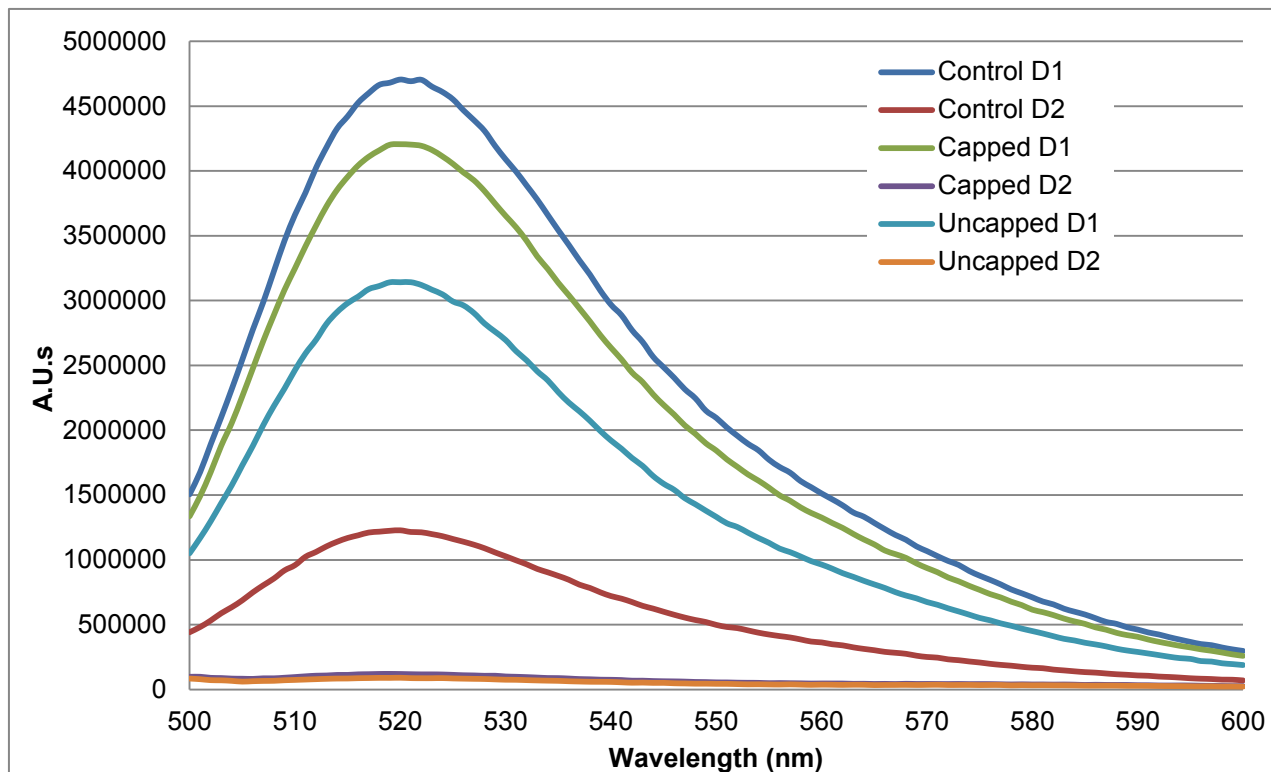


Figure 3-15: Fluorescence measurements of film washes after each nuclease digestion of CHI/HA/6-FAM SA films with and without a capping layer analyzing for DNA loss from the films. Control film was uncapped and exposed to the assay process without addition of nuclease. All films were made using the modified method. The presence of DNA was monitored by the fluorescence of fluorescein (Ex=490nm).

under the conditions of the assay (ionic strength is technically even higher due to the presence of other species). As a result, DNA migration (laterally and out of the film) is observed. Increases in ionic strength have been shown to influence film structure and integrity. This manifests as an increase in electrostatic shielding until PEs of opposite charge are unable to maintain a sufficient number of interactions^[161]. The film becomes unable to build new bilayers and eventually grows unstable and falls apart as ionic strength continues to increase. This effect can be exaggerated in films where a large size difference between PEs exists^[161]. Dubas *et al* found that increasing the surrounding ionic strength led to swelling and eventual structural instability and dissolution (0.6M NaCl) of

PAA/PDDA multilayers^[161]. In another study, prolonged incubation of freshly prepared PSS/PDDA films in solutions of higher salt concentration (than they were constructed in) had a “smoothing” effect on the films^[162]. The measured decrease in RMS roughness was attributed to a leveling effect involving lateral migration of PE from crests to valleys possibly due to ionic shielding. Weakly charged groups (such as HA) tend to be more sensitive to changes in ionic strength as fewer ionic crosslinks are responsible for holding the film together^[163].

To add to this effect, heat was shown to have an effect on film-dye interactions leading to a large increase in nonspecific binding (as discussed in Section 2.3.3). The root of this effect was suspected to be heat induced swelling allowing for material loss from the film resulting in an increased number of fixed charges. Similarly, it is possible that the 90°C washes carry enough thermal energy to overcome the limited number of interactions between the DNA and the CHI (due to the smaller size of the DNA), and in combination with film swelling, enable movement of the DNA. This effect could be similar to annealing in which DNA is shuttled to areas in the film where the surrounding interactions produce a more stable energy minimum or, the DNA may be able to escape the film due to a more “denaturing” effect. In combination, these two factors could be responsible for the shifting of DNA within the film matrix and its escape to the surrounding medium. An alternative study could include a real-time fluorescence assay using a technique such as confocal under flow conditions tracking the loss of fluorescence over time. This would eliminate the need to inactivate the nuclease after a finite period of time and hence remove the thermal effects of the rinsing

procedure all together. Alternative nucleases which function under low ionic conditions at a similar pH could also be employed instead of Nuclease S₁ to reduce the effects of ionic strength.

3.4. Conclusions

Although previous studies have shown pairing of DNA with a PE gives a protective effect against nuclease-assisted degradation, no studies have investigated how that effect translates to DNA integrated into LBL films. Protection of aptamers against degradation without compromising its binding functions is of particular interest as it gives options of extending the lifetime of real-world applications whose major hurdle is rapid digestion of the aptamer sequence. Gel and fluorescence assisted analysis of Nuclease S₁-mediated degradation of ssDNA within CHI/HA films were attempted. Detection limit restrictions prevented useful fragmentation information in PAGE gel analysis. Film instability due to increased ionic strength and temperatures resulted in non-nuclease related DNA loss in fluorescence studies. Novel methods with lower limits of detection and/or scale-up methodologies able to accommodate large sample volumes are required for further investigation of nuclease-mediated degradation of film-bound ssDNA.

Chapter 4. Contributions to knowledge and future studies

The research presented demonstrates that a highly structured aptamer can still function within a film matrix and thus the proof of concept work was not an isolated event. This promising result likely translates to many film systems and opens doors to the wide range of PE available for LBL film assembly; providing a wide range of materials and functionalities to tailor a smart fertilizer system able to resist the harsh conditions of *in situ* use. Moreover, this system confirmed the compatibility of this concept with materials possessing the desired biocompatibility properties for a large-scale agricultural technology. Despite the difficulties encountered, there is still great promise in embedding aptamers within LBL films in order to enhance nuclease resistance without affecting binding function. Further development of smart materials is not only beneficial to agricultural technologies, but could also prove useful in therapeutic and controlled delivery applications as well.

This preliminary work provides a promising start for future smart fertilizer technology, however there are still many more experiments required to validate the concepts presented. While this system was successful as a film, it is still unclear if the results presented will translate to a microcapsule system. The films used were extremely thick compared to the proof-of-concept system which may be detrimental to microcapsule formation. The binding event between the aptamer and target dye must also trigger and permeability change in the microcapsule and the films must be optimized for ideal diffusion characteristics.

Finally, specificity was not tested in this work. Tests demonstrating that the binding events are specifically reserved for the target and not similar molecules must also be performed confirming that the specificity of the aptamer is not changed by the film matrix.

It is obvious from the nuclease studies that LBL systems are very sensitive to environmental changes such as pH and ionic strength which could prove challenging in *in situ* applications. Chemical crosslinking of film layers is an option commonly employed to help improve LBL film stability and offers considerable control over the extent of linking through reaction times and reagent concentrations. Real-time studies using confocal or the use of alternative nucleases working under more compatible conditions could help establish a preliminary knowledge-base on the protective abilities of the film. Alternatively, using nucleases with a wide range of working conditions may help establish conditions where the films are susceptible to deformation (and hence increased DNA degradation). This could help target the issues that need to be addressed with film stability.

Appendices

Appendix A. Aptamer-functionalized multilayer films (Chapter 2)

A.1 ToF-SIMS sputter profiles of 5 bilayer base films

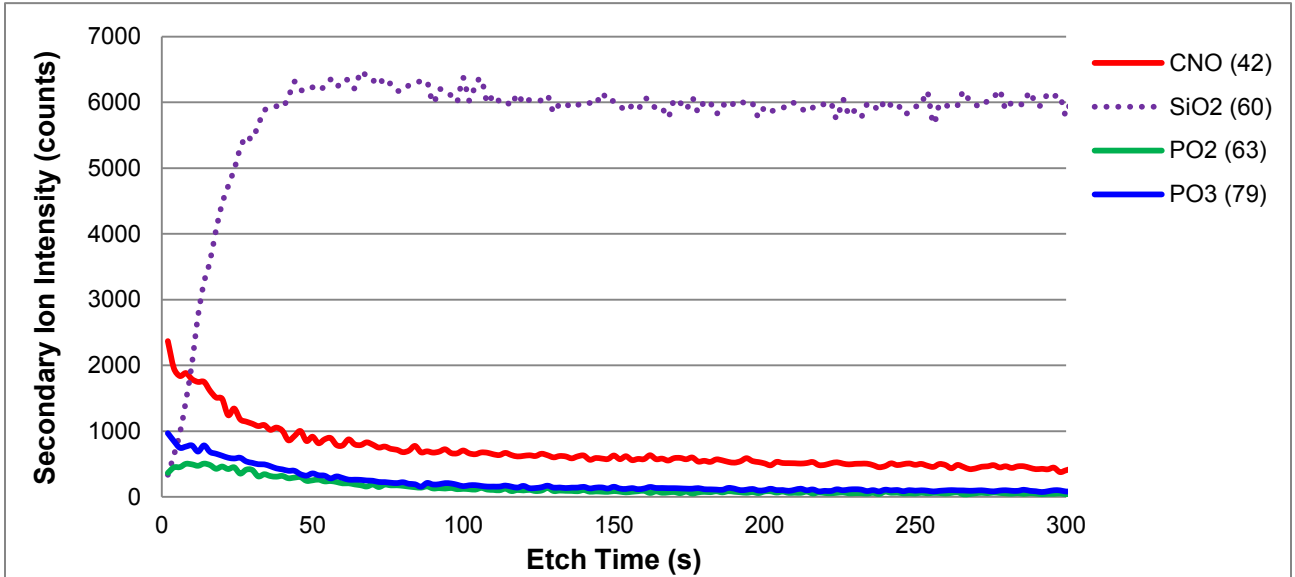


Figure A.1-1: ToF-SIMS sputter profile of a multilayer film composed of 5 CHI/HA bilayers. The depth profile shows the characteristic secondary ions for tracking relevant species within the film. Ion masses (in g/mol) are shown in brackets. As the film was not exposed to dye, SO_3^{2-} was not tracked.

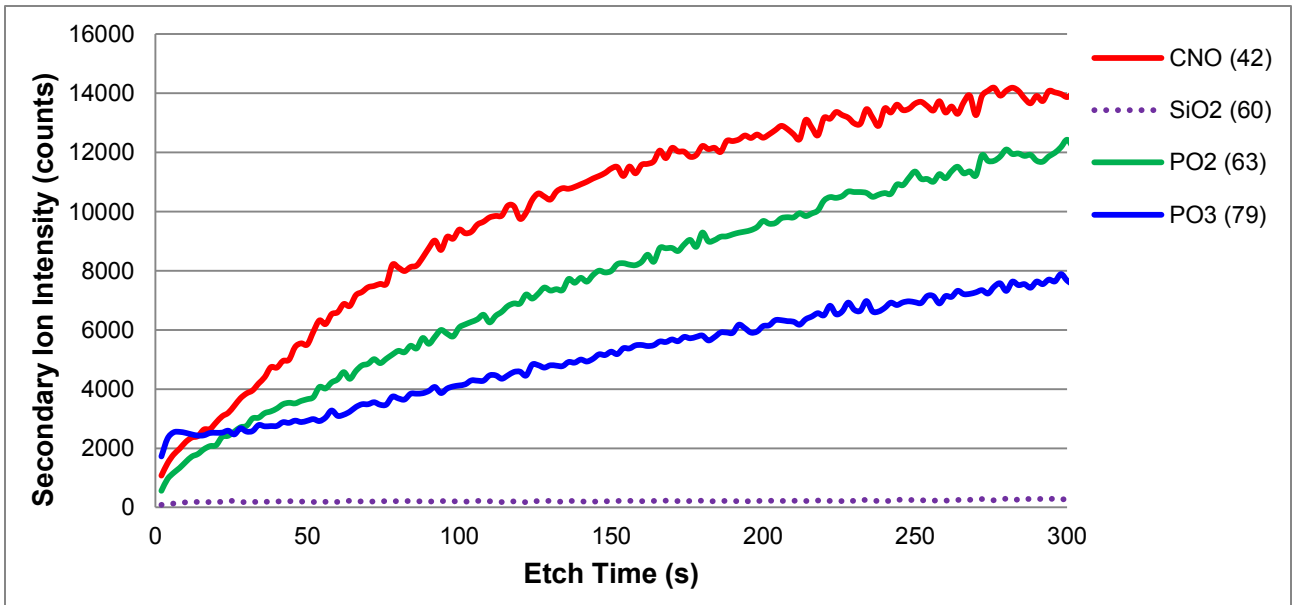


Figure A.1-2: ToF-SIMS sputter profile of a multilayer film composed of 5 CHI/HA – 5 CHI/SA bilayers (no capping layer). The depth profile shows the characteristic secondary ions for tracking relevant species within the film. Ion masses (in g/mol) are shown in brackets. As the film was not exposed to dye, SO_3^{2-} was not tracked.

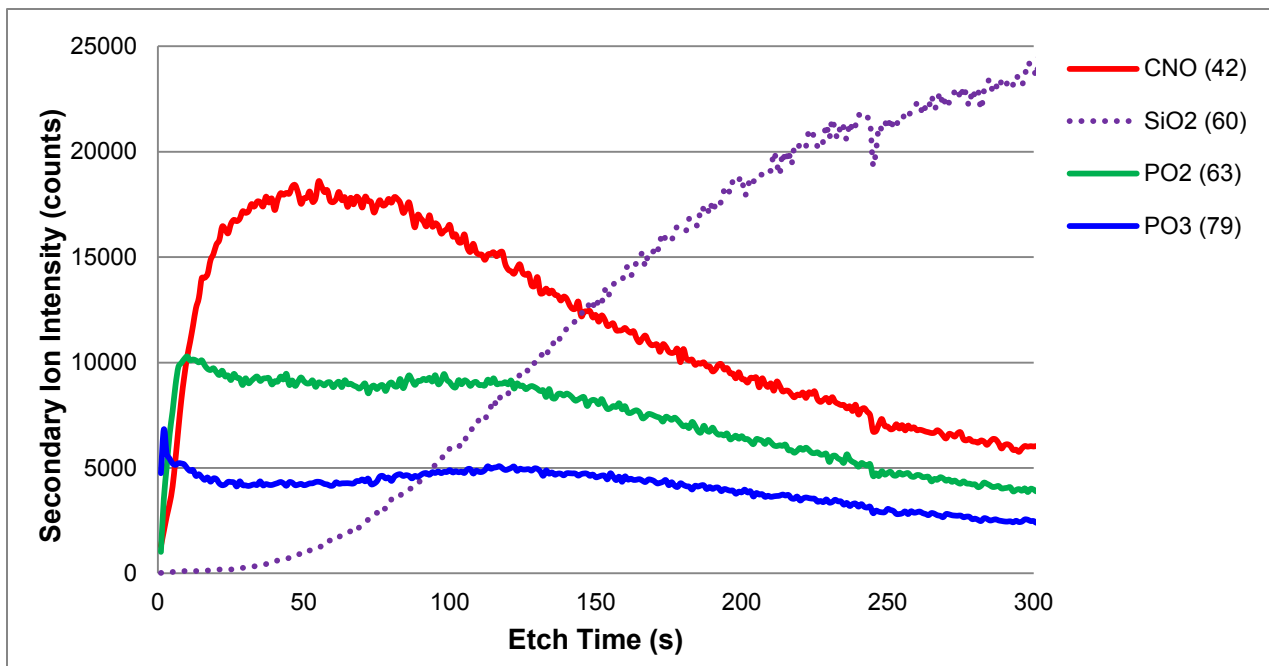


Figure A.1-3: ToF-SIMS sputter profile of a multilayer film composed of 5 CHI/HA – 5 CHI/RO bilayers (no capping layer). The depth profile shows the characteristic secondary ions for tracking relevant species within the film. Ion masses (in g/mol) are shown in brackets. As the film was not exposed to dye, SO_3^{2-} was not tracked.

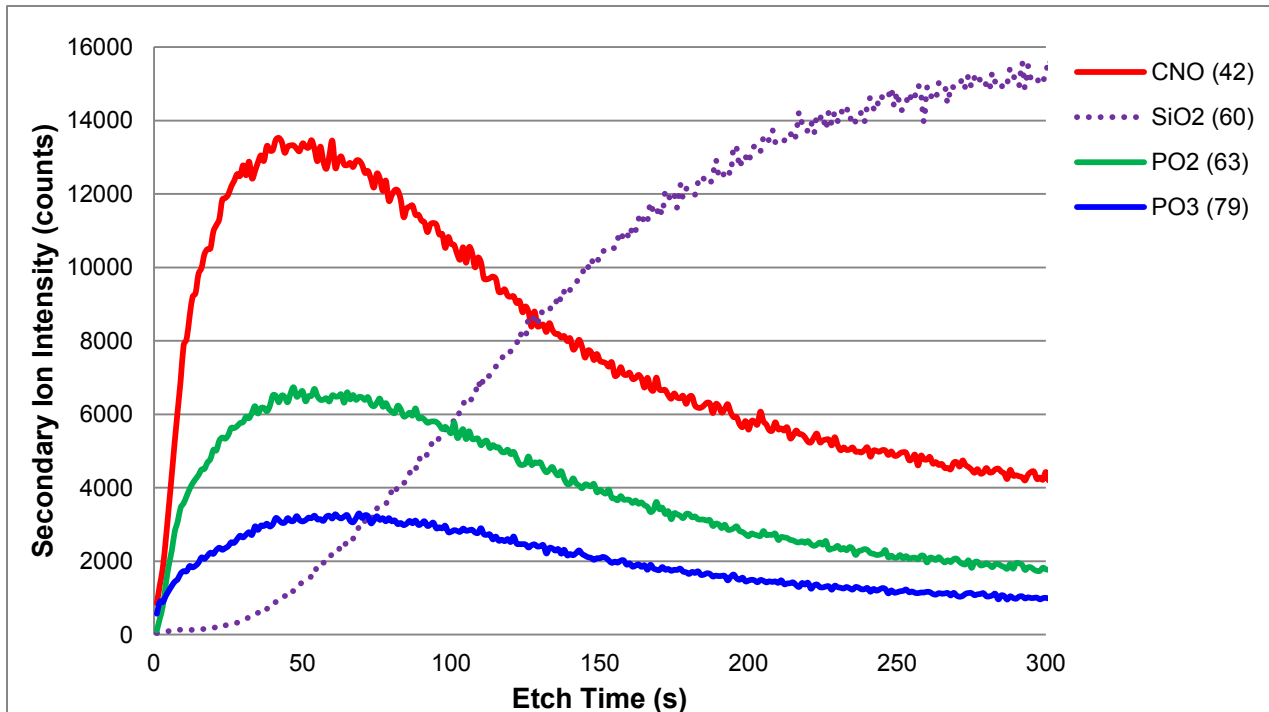


Figure A.1-4: ToF-SIMS sputter profile of a multilayer film composed of 5 CHI/HA – 5 CHI/SA – 1 CHI/HA bilayers. The depth profile shows the characteristic secondary ions for tracking relevant species within the film. Ion masses (in g/mol) are shown in brackets. As the film was not exposed to dye, SO_3^{2-} was not tracked.

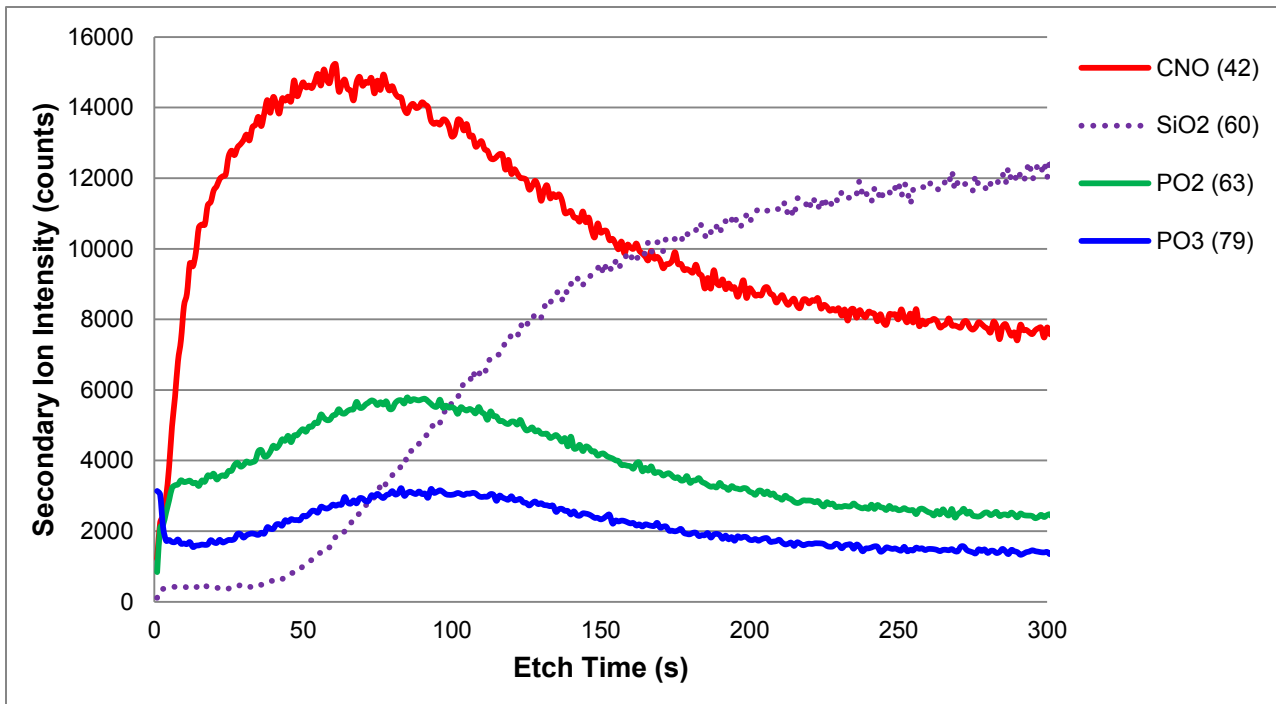


Figure A.1-5: ToF-SIMS sputter profile of a multilayer film composed of 5 CHI/HA – 5 CHI/RO – 1 CHI/HA bilayers. The depth profile shows the characteristic secondary ions for tracking relevant species within the film. Ion masses (in g/mol) are shown in brackets. As the film was not exposed to dye, SO_3^{2-} was not tracked.

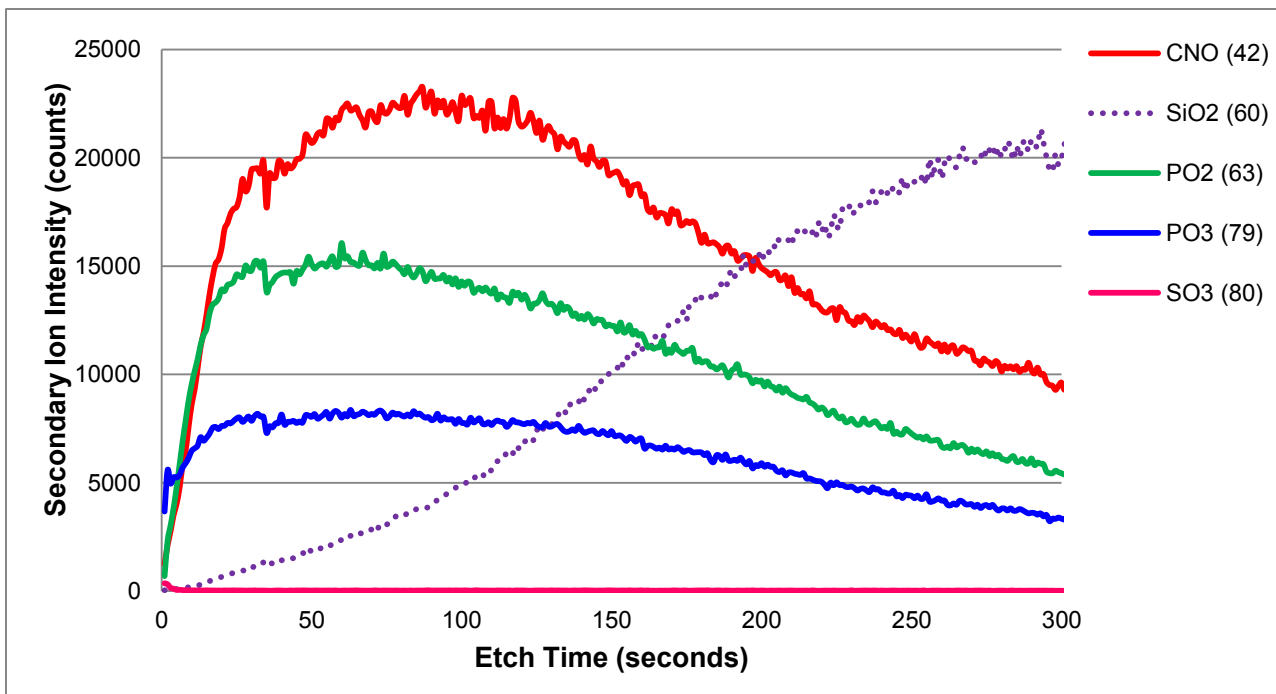


Figure A.1-6: ToF-SIMS sputter profile from a sample set of multilayer films with the general composition of 5 CHI/HA – 5 CHI/RO – 1 CHI/HA after exposure to 2mM SB dye. The depth profile shows the characteristic secondary ions for tracking relevant species within the film. Ion masses (in g/mol) are shown in brackets.

A.2 Hydrated AFM of a CHI/HA/DNA film

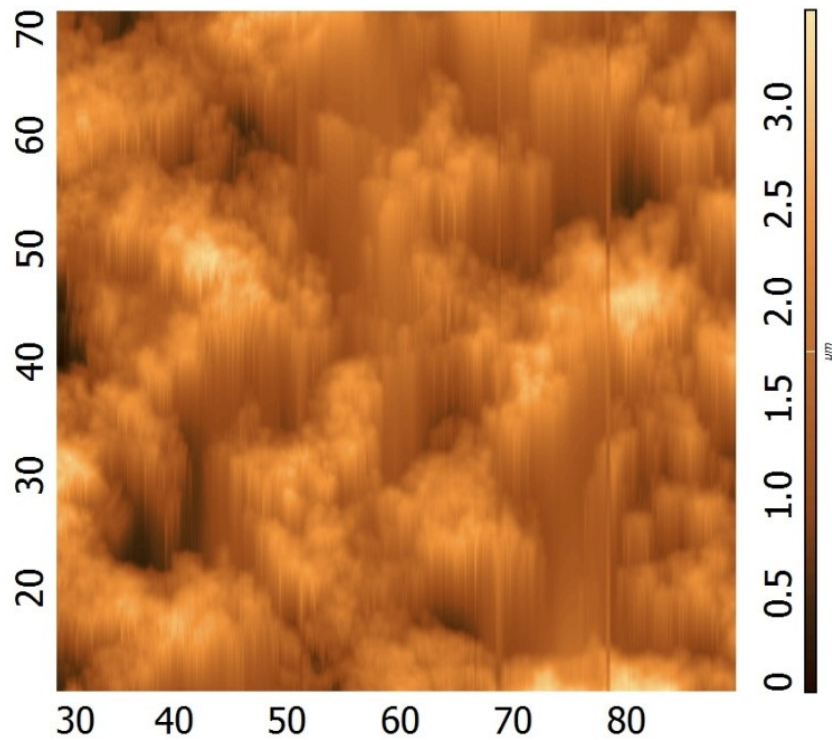


Figure A.2-1: Attempted AFM image of a multilayer film composed of 10 CHI/HA – 5 CHI/SA – 1 CHI/HA layers in 0.15M NaCl. Streaking in the images indicates sticking of the AFM tip due to the soft nature of the films.

Appendix B. Growth studies of CHI/HA multilayer films (Chapter 2)

B.1 Effects of drying on UV-Vis measurements of CHI/HA films

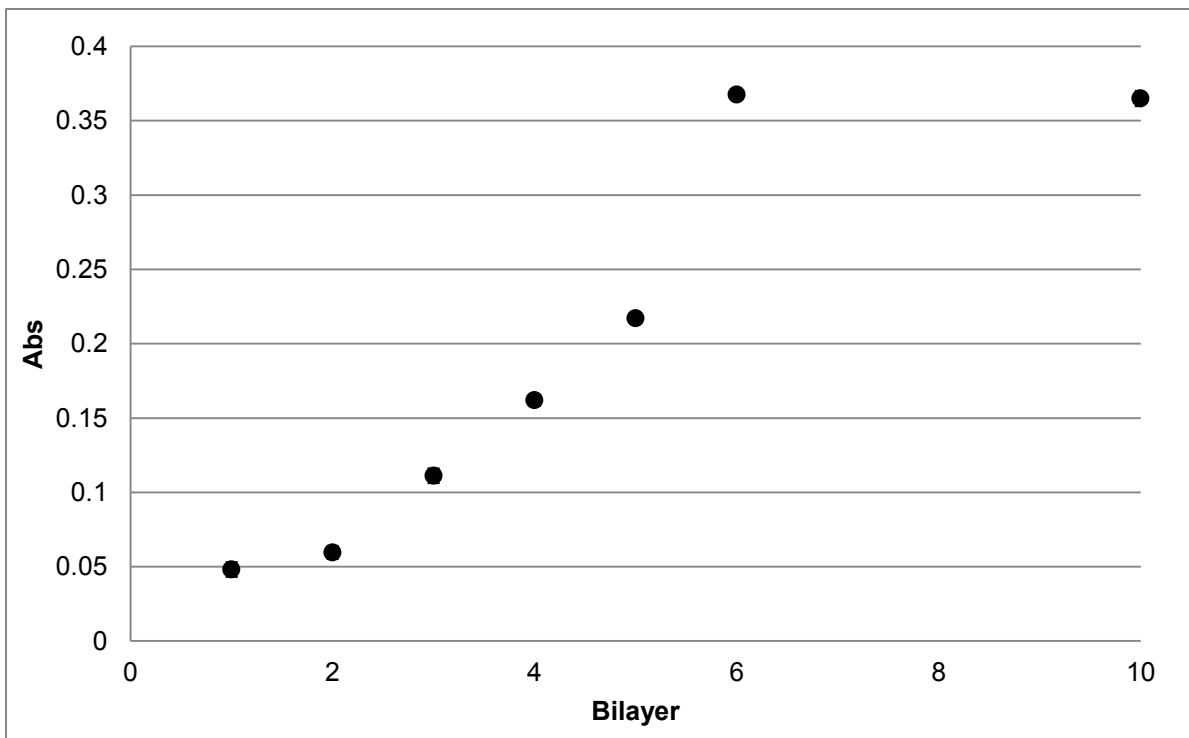


Figure B.1-1: Plot of the average absorbance between 190-220nm monitoring the growth of CHI/HA bilayers deposited on a quartz substrate to investigate the effects of drying the films. Two films were monitored; one measuring the absorbance after the deposition of each bilayer, and the other constructed to 10 bilayers before analysis. Absorbance issues seen in other growth studies are not the result of drying as the both the 6 bilayer and 10 bilayer measurements produced the same absorbance. Three trials were done for each measurement to account for minor compositional variances. Water rinse (10mL) was for 1 minute. Error bars represent standard deviation.

B.2 CHI/HA growth mechanism plots without normalized data

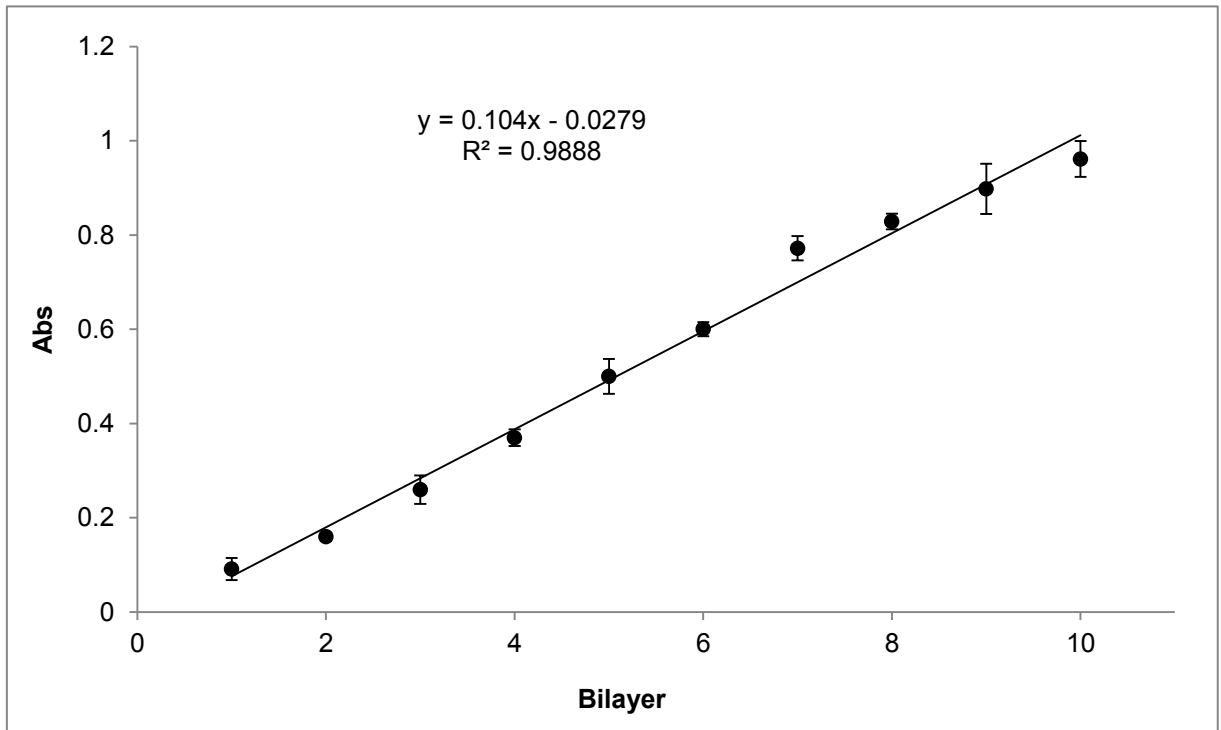


Figure B.2-1: Plot of the average absorbance between 190-220nm monitoring the growth of CHI/HA bilayers deposited by the original protocol. Data was not normalized to subtract scattering effects. Scattering was found to become a significant portion of the observed change after and absorbance of 0.5-0.6 is reached. Three trials were done for each bilayer to account for minor compositional variances. Water rinse was for 10 seconds. Error bars represent standard deviation.

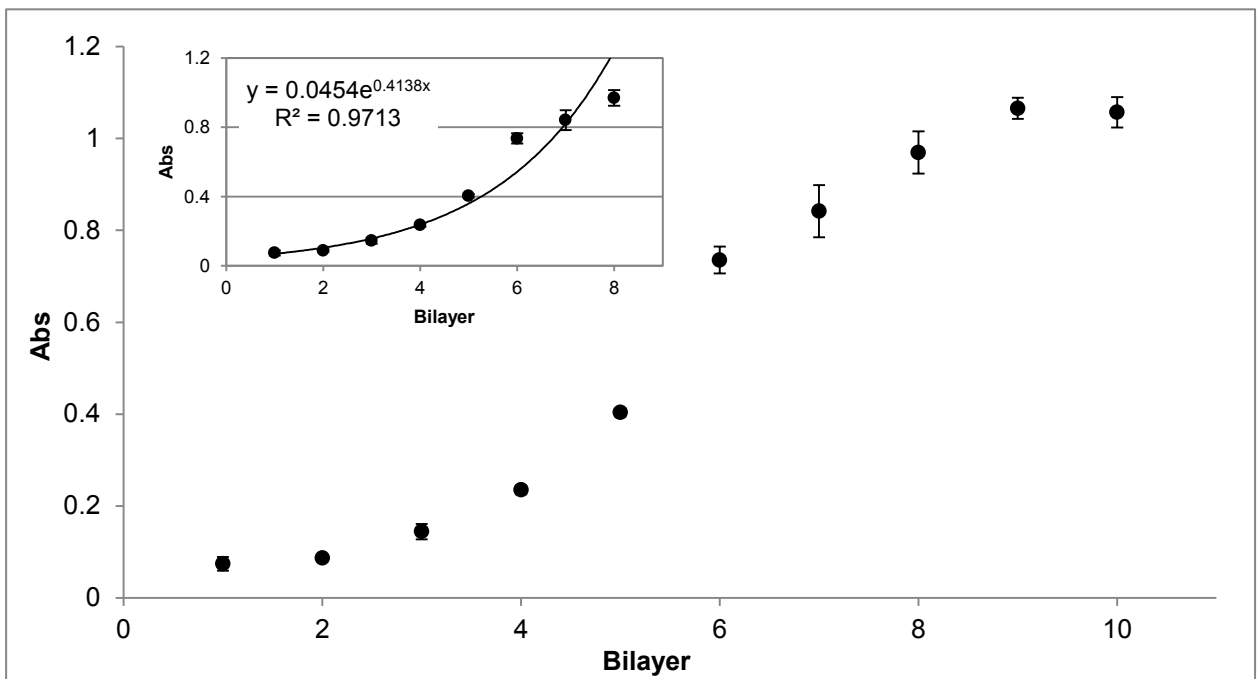


Figure B.2-2: Plot of the average absorbance between 190-220nm monitoring the growth of CHI/HA bilayers deposited by the modified protocol with increased rinse times, volume, and frequency of solution changes. Three trials were done for each bilayer to account for minor compositional variances. Data was not normalized to subtract scattering effects. Scattering was found to become a significant portion of the observed change after and absorbance of 0.5-0.6 is reached. Water rinse was for 1 minute. Error bars represent standard deviation. Inset: Exponential region of the growth curve over bilayers 1 to 8.

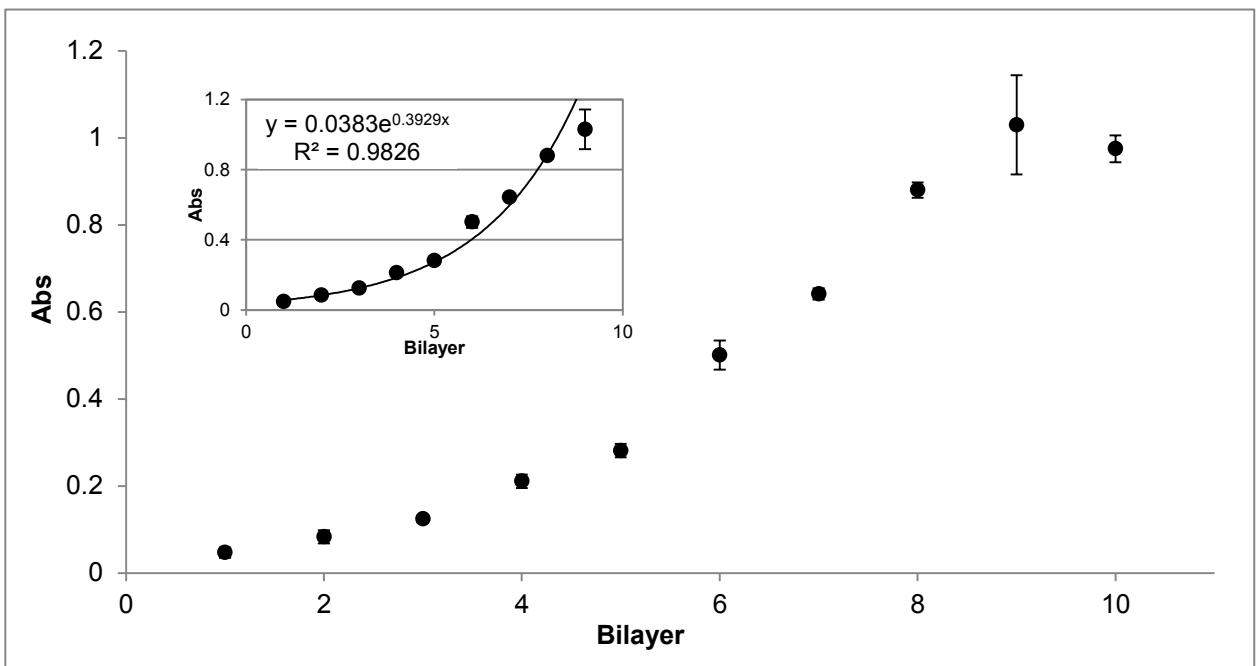


Figure B.2-3: Plot of the average absorbance between 190-220nm monitoring the growth of CHI/HA bilayers deposited by an adaptation of the modified protocol where the rinses were changed with every use (FS protocol). Three trials were done for each bilayer to account for minor compositional variances. Data was not normalized to subtract scattering effects. Scattering was found to become a significant portion of the observed change after and absorbance of 0.5-0.6 is reached. Water rinse was for 10s. Error bars represent standard deviation. Inset: Exponential region of the growth curve over bilayers 1 to 9.

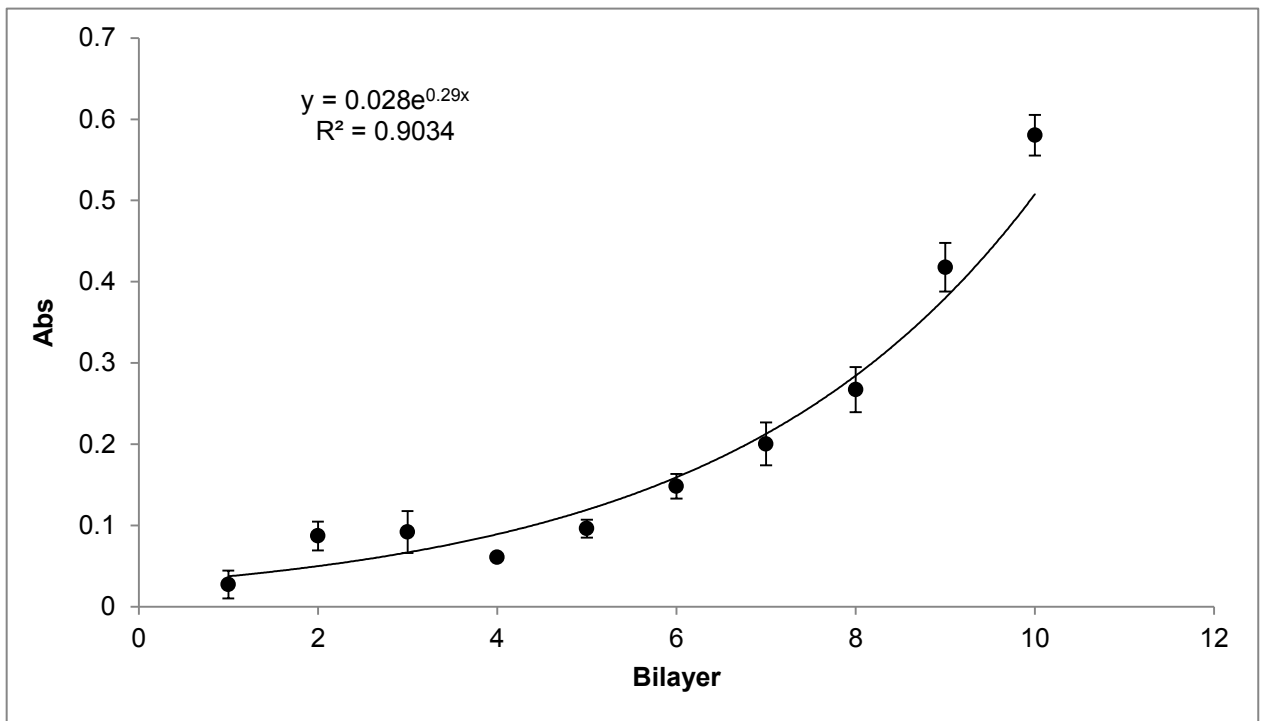


Figure B.2-4: Plot of the average absorbance between 190-220nm monitoring the growth of CHI/HA bilayers deposited by an adaptation on the modified protocol with increased rinse volumes (Mulligan protocol). Three trials were done for each bilayer to account for minor compositional variances. Data was not normalized to subtract scattering effects. Scattering was found to become a significant portion of the observed change after and absorbance of 0.5-0.6 is reached. Water rinse was for 1 minute. Error bars represent standard deviation.

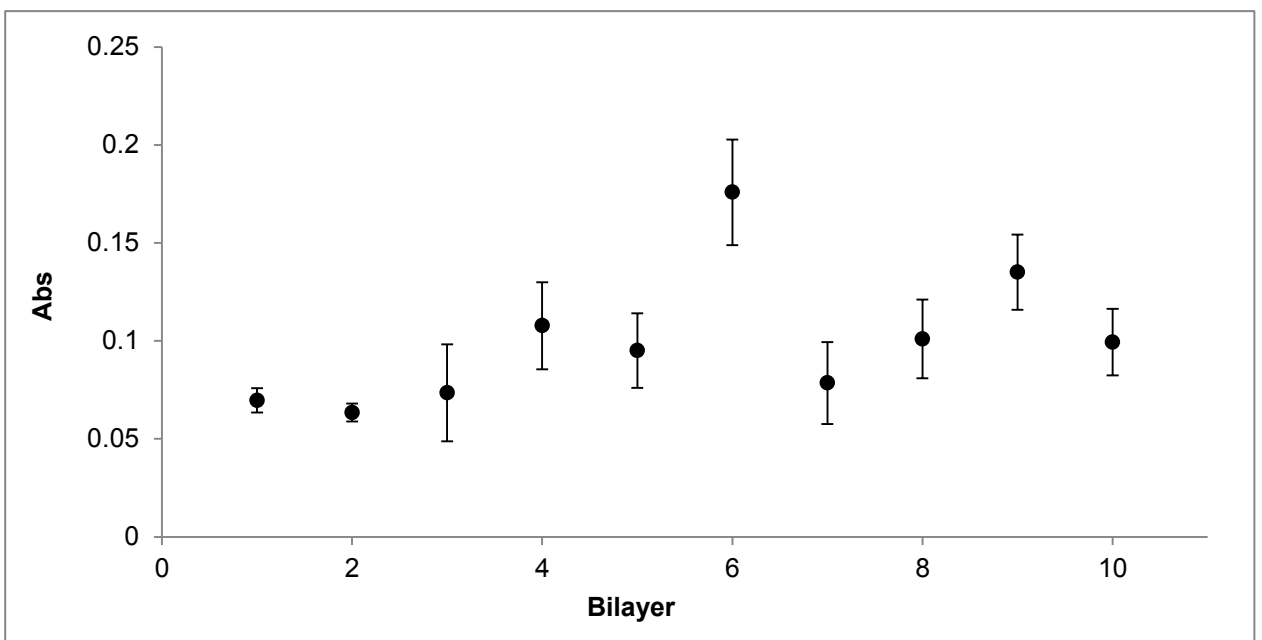


Figure B.2-5: Plot of the average absorbance between 190-220nm monitoring the growth of CHI/HA bilayers deposited by an adaptation of the modified protocol with increased rinse volumes, times, and number (Richert protocol). Data was not normalized to subtract scattering effects. Scattering was found to become a significant portion of the observed change after and absorbance of 0.5-0.6 is reached. Three trials were done for each bilayer to account for minor compositional variances. Water rinse was for 10 seconds. Error bars represent standard deviation.

Appendix C. Growth studies of CHI/HA/DNA multilayer films (Chapter 2)

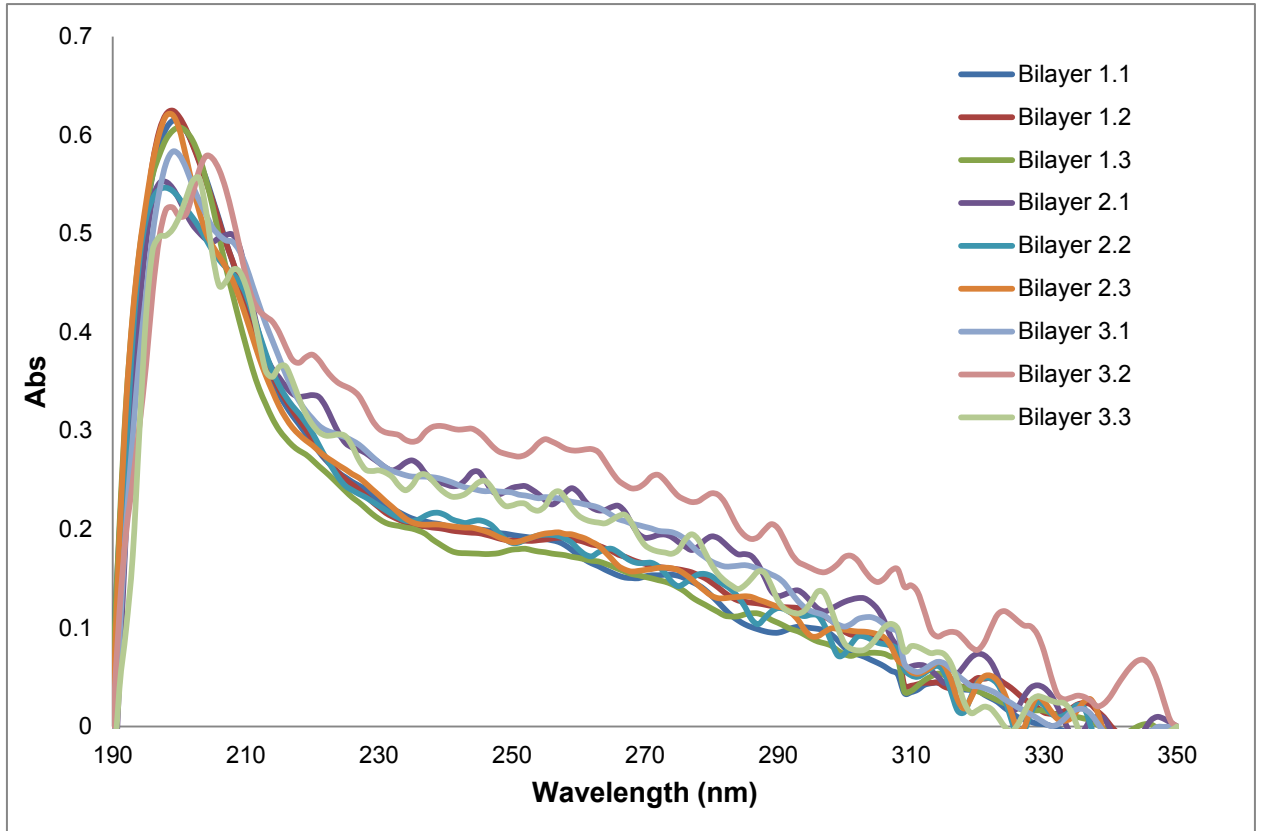


Figure C-1: UV-Vis analysis monitoring the growth of CHI/SA bilayers on a base of 10 CHI/HA bilayers by monitoring the absorbance of SA DNA at 253nm. Films were grown by the original method using PE concentrations of 1mg/mL. Three trials were done for each bilayer to account for minor compositional differences. All data is normalized to 350nm. Water rinse was for 5s. Increased scattering was seen across the wavelengths scanned with each additional CHI/DNA bilayer deposited indicating the film base was too thick. Analysis was therefore discontinued after the deposition of 3 CHI/DNA bilayers.

References

- [1] Borm, P. J., Robbins, D., Haubold, S., Kuhlbusch, T., Fissan, H., Donaldson, K., Schins, R., Stone, V., Kreyling, W., Lademann, J., Krutmann, J., Warheit, D., Oberdorster, E. *Part Fiber Toxicol.* **2006**, *3*, 1-35.
- [2] Shapira, P., Wang, J. *Nature* **2010**, *468*, 627-628.
- [3] Coccia, M., Finardi, U., Margon, D. *J. Technol. Transf.* **2012**, *37*, 777-787.
- [4] Grassian, V. H. *J. Phys. Chem.* **2008**, *112*, 18303-18313.
- [5] Roduner, E. *Chem. Soc. Rev.* **2006**, *35*, 583-592.
- [6] Boverhof, D. R., David, R. M. *Anal. Bioanal. Chem.* **2010**, *396*, 953-961.
- [7] Barreto, J. A., O'Malley, W., Kubeil, M., Graham, B., Stephan, H., Spiccia, L. *Adv. Mater.* **2011**, *23*, H18-H40.
- [8] Peralta-Videa, J. R., Zhao, L., Lopez-Moreno, M. L., Rosa, G., Hong, J., Gardea-Torresdey, J. L. *J. Hazard. Mater.* **2011**, *186*, 1-15.
- [9] Lines, M. G. *J. Alloys Compd.* **2008**, *449*, 242-245.
- [10] Webster, D. M., Sundaram, P., Byrne, M. E. *Eur. J. Pharm. Biopharm.* **2013**, *84*, 1-20.
- [11] Srikanth, M., Kessler, J. A. *Nature Rev.* **2012**, *8*, 307-318.
- [12] Ghormade, V., Deshpande, M. V., Paknikar, K. M. *Biotech. Adv.* **2011**, *29*, 792-803.
- [13] Dvir, T., Timko, B. P., Kohane, D. S., Langer, R. *Nat. Nanotech.* **2011**, *6*, 13-22.
- [14] Song, S., Wang, L., Li, J., Zhao, J., Fan, C. *TrAC*, **2008**, *27*, 108-117.
- [15] Wilson, C., Szostak, J. W. *Chem. & Bio.* **1998**, *5*, 609-617.
- [16] Huizenga, D. E., Szostak, J. W. *Biochem.* **1995**, *34*, 656-665.
- [17] Cruz-Aguado, J. A., Penner, G. *J. Agric. Food Chem.* **2008**, *56*, 10456-10461.
- [18] Paborsky, L. R., McCurdy, S. N., Griffin, L. C., Toole, J. J., Leung, L. L. K. *J. Biol. Chem.* **1993**, *268*, 20808-20811.
- [19] Schurer, H., Stembera, K., Knoll, D., Mayer, G., Blind, M., Forster, H., Famulok, M., Welzel, P., Hahn, U. *Bioorg. Med. Chem.* **2001**, *9*, 2557-2563.
- [20] Gopinath, S. C. B., Sakamaki, Y., Kawasaki, K., Kumar, P. K. R. *J. Biochem.* **2006**, *139*, 837-846.
- [21] Jenison, R. D., Gill, S. C., Pardi, A., Polisky, B. *Science*, **1994**, *263*, 1425-1429.
- [22] Tombelli, S., Minunni, M., Mascini, M. *Biosens. Bioelectron.* **2005**, *20*, 2424-2434.
- [23] D'Amico, D. J., Masonson, H. N., Patel, M. *J Ophthalmol.* **2006**, *113*, 992-1001.
- [24] Zhou, J., Battig, M. R., Wang, Y. *Anal. Bioanal. Chem.* **2010**, *398*, 2471-2480.

-
- [25] Robertson, D. L., Joyce, G. F. *Nature* **1990**, *344*, 467-468.
- [26] Bunka, D. H. J., Platonova, O., Stockley, P. G. *Curr. Opin. Pharmacol.* **2010**, *10*, 557-562.
- [27] Ellington, A. D., Szostak, J. W. *Nature* **1990**, *346*, 818-822.
- [28] Silverman, S. K. *Functional Nucleic Acids for Analytical Applications* **2009**, *1*, 50.
- [29] Stoltenburg, R., Reinemann, C., Strehlitz, B. *Biomol. Eng.* **2007**, *24*, 381-403.
- [30] White, R. J., Rowe, A. A., Plaxco, K. W. *Analyst* **2010**, *135*, 589-594.
- [31] Povsic, T. J., Vavalle, J. P., Aberle, L. H., Kasprzak, J. D., Cohen, M. G., Mehran, R., Bode, C., Buller, C. E., Montalescot, G., Cornel, J. H., Rynkiewicz, A., Ring, M. E., Zeymer, U., Natarajan, M., Delarche, N., Zelenkofske, S. L., Becker, R. C., Alexander, J. H. *Eur. Heart. J.* **2012**, DOI: 10.1093/eurheartj/ehs232.
- [32] Sheng, Q., Liu, R., Zhang, S., Zheng, J. *Biosens. Bioelectron.* **2013**, *51*, 191-194.
- [33] Lee, J., Kim, J. H., Lee, S. H., Kim, J. Y., Mah, S. J., Gu, M. B. *Biochip J.* **2013**, *7*, 180-187.
- [34] Dong, Z. M., Zhao, G. C. *Analyst* **2013**, *138*, 2456-2462.
- [35] Zuo, P., Li, X., Dominguez, D. C., Ye, B. C. *Lab Chip* **2013**, *13*, 3921-3928.
- [36] Sultan, Y., Walsh, R., Monreal, C., DeRosa, M. *Biomacromolecules* **2009**, *10*, 1149-1154.
- [37] Sultan, Y., DeRosa, M. *Small* **2011**, *7*, 1219-1226.
- [38] Townsend, A. R., Howarth, R. W. *Sci. Amer.* **2010**, *302*, 64-71.
- [39] Novoa, R., Loomis, R. S. *Plant Soil* **1981**, *58*, 177-204.
- [40] Fisher, K., Newton, W. E. **2002**. *Nitrogen Fixation at the Millennium*. Elsevier Science B. V., Netherlands: pp 1-3.
- [41] Robertson, G. P., Groffman, P. M. **2006**. *Soil Microbiology, Ecology, and Biochemistry*. Elsevier, USA: pp. 347-355.
- [42] Erisman, J. W., Sutton, M. A., Galloway, J., Klimont, Z., Winiwarter, W. *Nat. Geo.* **2008**, *1*, 636-639.
- [43] Chen, H., Yada, R. *Trends Food Sci. Tech.* **2011**, *22*, 585-594.
- [44] FAO. *Current world fertilizer trends and outlook to 2016*. Rome, **2012**.
- [45] Schubert, C. *Nat. Biotech.* **2006**, *24*, 777-784.
- [46] DeRosa, M. C., Monreal, C., Schnitzer, M., Walsh, R., Sultan, Y. *Nat. Nanotech.* **2010**, *5*, 91.
- [47] Camargo, J. A., Alonso, A. *Environ. Int.* **2006**, *32*, 831-849.
- [48] Ward, M. H., deKok, T. M., Lavallois, P., Brender, J., Gulis, G., Nolan, B. T., VanDerslice, J. *Environ. Health Perspect.* **2005**, *11*, 1607-1614.

-
- [49] Abrol, Y. P., Raghuram, N., Sachdev, M. S. **2007**. *Agricultural Nitrogen Use and Its Environmental Implications*. I.K. International Publishing House Pvt. Ltd., India: pp. 510-513.
- [50] Oertli, J. J. *Fert. Res.* **1980**, *1*, 103-123.
- [51] Melaj, M. A., Daraio, M. E. *J. Appl. Polym. Sci.* **2013**, DOI: 10.1002/APP.39452.
- [52] Berber, M. R., Hafez, I. H., Minagawa, K., Mori, T. *J. Soils Sediments* **2013**, DOI: 10.1007/s11368-013-0766-3.
- [53] Corradini, E., Moura, M. R., Mattoso, L. H. C. *Polym. Lett.* **2010**, *4*, 509-515.
- [54] Ohkama-Ohtsu, N., Wasaki, J. *Plant Cell Physiol.* **2010**, *51*, 1255-1264.
- [55] Wu, F. Y., Chung, A. K. C., Tam, N. F. Y., Wong, M. H. *Int. J. Phytorem.* **2012**, *14*, 545-553.
- [56] Yoneyama, K., Xie, X., Kusumoto, D., Sekimoto, H., Sugimoto, Y., Takeuchi, Y., Yoneyama, K. *Planta* **2007**, *227*, 125-132.
- [57] Khorassani, R., Hettwer, U., Ratzinger, A., Steingrobe, B., Karlovsky, P., Claassen, N. *BMC Plant Bio.* **2011**, *11*, 1-8.
- [58] Dakora, F. D., Phillips, D. A. *Plant Soil* **2002**, *245*, 35-47.
- [59] Bais, H. P., Weir, T. L., Perry, L. G., Gilroy, S., Vivanco, J. M. *Annu. Rev. Plant Biol.* **2006**, *57*, 233-266.
- [60] Deng, Y., Hao, J. **2011**. *Self-assembled Structures: Properties and Applications in Solution and on Surfaces*. Taylor and Francis Group, USA: pp. 210.
- [61] Schwartz, D. K. *Sur. Sci. Rep.* **1997**, *27*, 241-334.
- [62] Zasadzinski, J. A., Viswanathan, R., Madsen, L., Garnaes, J., Schwartz, D. K. *Science* **1994**, *263*, 1726-1733.
- [63] Decher, G. *Science* **1997**, *277*, 1232-1237.
- [64] Josph, N., Ahmadiannamini, P., Hoogenboom, R., Vankelecom, I. F. J. *Polym. Chem.* **2013**, DOI: 10.1039/C3PY01262J.
- [65] Schoeler, B., Kumaraswamy, G., Caruso, F. *Macromolecules* **2002**, *35*, 889-897.
- [66] Lvov, Y., Decher, G., Mohwald, H. *Langmuir* **1993**, *9*, 481-486.
- [67] Shiratori, S. S., Rubner, M. F. *Macromolecules* **2000**, *33*, 4213-4219.
- [68] Tian, S., Liu, J., Zhu, T., Knoll, W. *Chem. Mater.* **2004**, *16*, 4103-4108.
- [69] Mamedov, A. A., Kotov, N. A., Prato, M., Guldi, D. M., Wicksted, J. P., Hirsch, A. *Nat. Mater.* **2002**, *1*, 190-194.
- [70] Schneider, A., Richert, L., Francius, G., Voegel, J. C., Picart, C. *Biomed. Mater.* **2007**, *2*, 45-51.
- [71] Ren, K., Ji, J., Shen, J. *Biomaterials* **2006**, *27*, 1152-1159.

-
- [72] Caruso, F., Niikuram K., Furlong, D. N., Okahata, Y. *Langmuir* **1997**, *13*, 3427-3433.
- [73] Lvov, Y., Haas, H., Decher, G., Mohwald, H. *Langmuir* **1994**, 4232-4236.
- [74] Lavalle, P., Picart, C., Mutterer, J., Gergely, C., Reiss, H., Voegel, J. C., Senger, B., Scaaf, P. *J. Phys. Chem.* **2004**, *108*, 635-648.
- [75] Kharlampieva, E., Sukhishvili, S. A. *J Macromol Sci Polymer Rev.* **2006**, *46*, 377-395.
- [76] Sievers, T. K., Vergin, A., Mohwald, H., Kurth, D. G. *Langmuir* **2007**, *23*, 12179-12184.
- [77] Kotov, N. A. *Nanostruct. Mater.* **1999**, *12*, 789-796.
- [78] Mesquita, J. P., Donnici, C. L., Pereira, F. V. *Biomacromolecules* **2010**, *11*, 473-480.
- [79] Richert, L., Lavalle, P., Payan, E., Shu, X. Z., Prestwich, G. D., Stoltz, J. F., Schaaf, P., Voegel, J. C., Picart, C. *Langmuir* **2004**, *20*, 448-458.
- [80] Picart, C., Lavalle, P., Hubert, P., Cusinier, F. J. G., Decher, G., Schaaf, P., Voegel, J. C. *Langmuir* **2001**, *17*, 7414-7424.
- [81] Elbert, D. L., Herbert, C. B., Hubbell, J. A. *Langmuir* **1999**, *15*, 5355-5362.
- [82] Porcel, C., Lavalle, P., Decher, G., Senger, B., Voegel, J. C., Schaaf, P. *Langmuir* **2007**, *23*, 1898-1904.
- [83] Picart, C., Gergely, C., Arntz, Y., Voegel, J. C., Schaaf, P., Cuisinier, F. J. G., Senger, B. *Biosens. Bioelectron.* **2004**, *20*, 553-561.
- [84] Xie, Y. L., Wang, M. J., Yao, S. J. *Langmuir* **2009**, *25*, 8999-9005.
- [85] Bieker, P., Schonhoff, M. *Macromolecules* **2010**, *43*, 5052-5059.
- [86] Sato, K., Yoshida, K., Takahashi, S., Anzai, J. *Adv. Drug Deliver. Rev.* **2011**, *63*, 809-821.
- [87] Salomaki, M., Vinokurov, I. A., Kankare, J. *Langmuir* **2005**, *21*, 11232-11240.
- [88] Ghostine, R. A., Markarian, M. Z., Schlenoff, J. B. *JACS* **2013**, *135*, 7636-7646.
- [89] Zhu, Z., Wu, C., Liu, H., Zou, Y., Zhang, X., Kang, H., Yang, C. J., Tan, W. *Angew. Chem.* **2010**, *122*, 1070-1074.
- [90] Farokhzad, O. C., Cheng, J., Teply, B. A., Sherifi, I., Jon, S., Kantoff, P. W., Richie, J. P., Langer, R. *PNAS* **2006**, *103*, 6315-6320.
- [91] Cao, Z., Tong, R., Mishra, A., Xu, W., Wong, G. C. L., Cheng, J., Lu, Y. *Angew. Chem.* **2009**, *48*, 6494-6498.
- [92] Wu, Y., Sefah, K., Liu, H., Wang, R., Tan, W. *PNAS* **2010**, *107*, 5-10.
- [93] So, H., Won, K., Kim, Y. H., Kim, B., Ryu, B. H., Na, P. S., Kim, H., Lee, J. O. *JACS* **2005**, *127*, 11906-11907.
- [94] Gu, B. X., Xu, C. X., Zhu, G. P., Liu, S. Q., Chen, L. Y., Wang, M. L., Zhu, J. J. *J. Phys. Chem. B.* **2009**, *113*, 6553-6557.

-
- [95] He, P., Hu, N., Zhou, G. *Biomacromolecules* **2002**, 3, 139-146.
- [96] Rinaudo, M. *Prog. Polym. Sci.* **2006**, 31, 603-632.
- [97] Gerente, C., Lee, V. K. C., Cloirec, P. L., McKay, G. *Crit. Rev. Env. Sci. Technol.* **2007**, 37, 41-127.
- [98] Hadwiger, L. A. *Plant Sci.* **2013**, 208, 42-49.
- [99] Bhatnagar, A., Sillanpaa, M. *Adv. Colloid Interface Sci.* **2009**, 152, 26-38.
- [100] No, H. K., Meyers, S. P., Prinyawiwatkul, W., Xu, Z. *J. Food Sci.* **2007**, 72, 87-100.
- [101] Kujawa, P., Moraille, P., Sanchez, J., Badia, A., Winnik, F. M. *JACS* **2005**, 127, 9224-9234.
- [102] Necas, J., Bartosikova, L., Brauner, P., Kolar, J. *Ve.t Med.* **2008**, 53, 397-411.
- [103] Kogan, G., Soltes, L., Stern, R., Gemeiner, P. *Biotechnol. Lett.* **2007**, 29, 17-25.
- [104] Toole, B. P. *Nat. Rev.* **2004**, 4, 528-539.
- [105] Thierry, B., Winnik, F. M., Merhi, Y., Silver, J., Tabrizian, M. *Biomacromolecules* **2003**, 4, 1564-1571.
- [106] Tan, H., Chu, C. R., Payne, K. A., Marra, K. G. *Biomaterials*, **2009**, 30, 2499-2506.
- [107] Lim, S. T., Martin, G. P., Berry, D. J., Brown, M. B. *J Control. Release* **2000**, 66, 281-292.
- [108] Picart, C., Schneider, A., Etienne, O., Mutterer, J., Schaaf, P., Egles, C., Jessel, N., Voegel, J. C. *Adv. Funct. Mater.* **2005**, 15, 1771-1780.
- [109] Sambrook, J. R. D. **2001**. *Molecular Cloning: A Laboratory Manual*.
- [110] Raposo, M., Ferreira, Q., Riberio, P. A. *Mod.Res.Educ.Top.Microscopy* **2007**, 758-768.
- [111] Lavallo, P., Gergely, C., Cuisinier, F. J. G., Decher, G., Schaaf, P., Voegel, J. C., Picart, C. *Macromolecules* **2002**, 35, 4458-4465.
- [112] Ram, M. K., Salerno, M., Adami, M., Faraci, P., Nicolini, C. *Langmuir* **1999**, 15, 1252-1259.
- [113] Fujii, N., Fujimoto, K., Michinobu, T., Akada, M., Hill, J. P., Shiratori, S., Argia, K., Shigehara, K. *Macromolecules* **2010**, 43, 3947-3955.
- [114] Crouzier, T., Boudou, T., Picart, C. *Curr. Opin. Colloid In.* **2010**, 15, 417-426.
- [115] Kulcsar, A., Voegel, J. C., Schaaf, P., Kekicheff, P. *Langmuir* **2005**, 21, 1166-1170.
- [116] Porcel, C., Lavallo, P., Ball, V., Decher, G., Senger, B., Voegel, J. C., Schaaf, P. *Langmuir* **2006**, 22, 4376-4383.
- [117] Collin, D., Lavallo, P., Garza, J. M., Voegel, J. C., Schaaf, P., Martinoty, P. *Macromolecules* **2004**, 37, 10195-10198.
- [118] Hammond, P. T. *AIChE* **2011**, 57, 2928-2940.
- [119] Gao, C., Leporatti, S., Moya, S., Donath, E., Mohwald, H. *Chem. Eur. J.* **2003**, 9, 915-920.

-
- [120] Mulligan, K., Jakubek, Z. J., Johnston, L. J. *Langmuir* **2011**, *27*, 14352-14359.
- [121] Wu, T, Zivanovic, S. *Carbohydr. Polym.* **2008**, *73*, 248-253.
- [122] Liu, D., Wei, Y., Yao, P., Jiang, L. *Carbohydr. Res.* **2006**, *341*, 782-785.
- [123] Upstone, S. L. **2000**. *Ultraviolet/Visible Light Absorption Spectrophotometry in Clinical Chemistry*. John Wiley & Sons, Chichester: pp. 1966-1714.
- [124] Stenzel, O. **2005**. *The Physics of Thin Film Optical Spectra: An Introduction*. Springer, Germany: pp. 101-118.
- [125] Hubsch, E., Ball, V., Senger, B., Decher, G., Voegel, J. C., Schaaf. *Langmuir* **2004**, *20*, 1980-1985.
- [126] Michel, M., Izquierdo, A., Decher, G., Voegel, J. C., Schaaf, P., Ball, V. *Langmuir* **2005**, *21*, 7854-7859.
- [127] Strand, S. P., Danielsen, S., Christensen, B. E., Varum, K. M. *Biomacromolecules* **2005**, *6*, 3357-3366.
- [128] Riche, E., Carrie, A., Andin, N., Mabic, S. **2006**. *High Purity Water and pH*. American Laboratory News.
- [129] Laugel, N., Betscha, C., Winterhalter, M., Voegel, J. C., Schaaf, P., Ball, V. *J. Phys. Chem.* **2006**, *110*, 19443-19449.
- [130] Lang, J., Liu, M. *J. Phys. Chem.* **1999**, *103*, 11393-11397.
- [131] Pei, R., Cui, X., Yang, X., Wang, E. *Biomacromolecules* **2001**, *2*, 463-468.
- [132] Luo, L., Liu, J., Wang, Z., Yang, X., Dong, S., Wang, E. *Biophys. Chem.* **2001**, *94*, 11-22.
- [133] Lvov, Y., Decher, G., Sukhorukov, G. *Macromolecules* **1993**, *26*, 5396-5399.
- [134] Sukhorukov, G. B., Mohwald, H., Decher, G., Lvov, Y. M. *Thin Solid Films* **1996**, *284-285*, 220-223.
- [135] Liu, Y., Hu, N. *Biosensors Bioelectronics* **2007**, *23*, 661-667.
- [136] Sui, Z., Salloum, D., Schlenoff, J. B. *Langmuir* **2003**, *19*, 2491-2495.
- [137] Zhu, C. L., Song, X. Y., Zhou, W. H., Wang, H. H., Wen, Y. H., Wang, X. R. *J. Mater. Chem.* **2009**, *19*, 7765-7770.
- [138] Ng, E. W. M., Shima, D. T., Calias, P., Cunningham, E. T., Guyer, D. R., Adamis, A. P. *Nat. Rev.* **2006**, *5*, 123-132.
- [139] Hong, P., Li, W., Li, J. *Sensors*, **2012**, *12*, 1181-1193.
- [140] Galarreta, B. C., Tabatabaci, M. *Anal. Bioanal. Chem.* **2013**, *405*, 1613-1621.
- [141] Keefe, A. D., Pai, S., Ellington, A. *Nat. Rev.* **2010**, *9*, 537-550.
- [142] Lin, Y., Qui, Q., Gill, S. C., Jayasena, S. D. *Nucleic Acids Res.* **1994**, *22*, 5229-5234.
- [143] Veedu, R. N., Wengel, J. *Chem. Biodiv.* **2010**, *7*, 536-542.

-
- [144] Schmidt, K. S., Borkowski, S., Kurreck, J., Stephens, A. W., Bald, R., Heckt, M., Friebe, M., Dinkelborg, L., Erdmann, V. A. *Nucleic Acids Res.* **2004**, *32*, 5757-5765.
- [145] Nielson, L., Olsen, L. F., Ozalp, V. C. *ACS Nano* **2010**, *4*, 4361-4370.
- [146] Pan, W., Craven, R. C., Qiu, Q., Wilson, C. B., Wills, J. W., Golovine, S., Wang, J. F. *PNAS* **1995**, *92*, 11509-11513.
- [147] Mascini, M. **2009**. *Aptamers in Bioanalysis*. John Wiley & Sons Inc., Canada: pp. 8.
- [148] Wu, Z., Tang, L. J., Zhang, X. B., Jiang, J. H., Tan, W. *ACS Nano* **2011**, *5*, 7696-7699.
- [149] Wu, Y., Phillips, J. A., Liu, H., Yang, R., Tan, W. *ACS Nano*, **2008**, *2*, 2023-2028.
- [150] Seferos, D. S., Prigodich, A. E., Gijohann, D. A., Patel, P. C., Mirkin, C. A. *Nano. Lett.* **2009**, *9*, 308-311.
- [151] Lau, J. L., Baksh, M. M., Fiedler, J. D., Brown, S. D., Kussrow, A., Bornhop, D. J., Ordoukhanian, P., Finn, M. G. *ACS Nano* **2011**, *5*, 7722-7729.
- [152] Antipov, A. A., Sukhorukov, G. B., Donath, E., Mohwald, H. *J. Phys. Chem.* **2001**, *105*, 2281-2284.
- [153] Antipov, A. A., Sukhorukov, G. B. *Adv. Colloid Interface Sci.* **2004**, *111*, 49-61.
- [154] Aravind, U. K., Mathew, J., Aravindakumar, C. T. *J. Membrane Sci.* **2007**, *299*, 146-155.
- [155] Miller, M. D., Bruening, M. L. *Langmuir* **2004**, *20*, 11545-11551.
- [156] Lentacker, I., Greest, B. G., Vanderbroucke, R. E., Peeters, L., Demeester, J., Smedt, S. C., Sanders, N. N. *Langmuir* **2006**, *22*, 7273-7278.
- [157] Yamauchi, F., Koyamatsu, Y., Kato, K., Iwata, H. *Biomaterials* **2006**, *27*, 3497-3504.
- [158] Hill, I. R. C., Garnett, M. C., Bignotti, F., Davis, S. S. *Anal. Biochem.* **2001**, *291*, 62-68.
- [159] Richardson, S. C. W., Kolbe, H. V. J., Duncan, R. *Int. J. Pharm.* **1999**, *178*, 231-243.
- [160] Thermo Fisher Scientific. **2012**. *Product Information: Nuclease S₁, Rev. 5*.
<http://www.thermoscientificbio.com/uploadedFiles/Resources/EN032_TS_5.pdf>
- [161] Dubas, S., Schlenoff, J. B. *Macromolecules* **2001**, *34*, 3736-3740.
- [162] Dubas, S. T., Schlenoff, J. B. *Langmuir* **2001**, *17*, 7725-7727.
- [163] Burke, S. E., Barrett, C. J. *Biomacromolecules* **2005**, *6*, 1419-1428.
- [164] Sultan, Y. **2011**. *Development of Smart Materials Using Aptamer Based Bionanotechnologies*. Ph. D Chem. Carleton University, Canada.